

# Nanoscale

Accepted Manuscript



This is an *Accepted Manuscript*, which has been through the Royal Society of Chemistry peer review process and has been accepted for publication.

*Accepted Manuscripts* are published online shortly after acceptance, before technical editing, formatting and proof reading. Using this free service, authors can make their results available to the community, in citable form, before we publish the edited article. We will replace this *Accepted Manuscript* with the edited and formatted *Advance Article* as soon as it is available.

You can find more information about *Accepted Manuscripts* in the [Information for Authors](#).

Please note that technical editing may introduce minor changes to the text and/or graphics, which may alter content. The journal's standard [Terms & Conditions](#) and the [Ethical guidelines](#) still apply. In no event shall the Royal Society of Chemistry be held responsible for any errors or omissions in this *Accepted Manuscript* or any consequences arising from the use of any information it contains.

## ARTICLE

## Recent advances in graphene and its metal-oxide hybrid nanostructured for lithium-ion batteries

Cite this: DOI: 10.1039/x0xx00000x

Manish Srivastava<sup>1, 2</sup>, Jay Singh<sup>3</sup>, Tapas Kuila<sup>4</sup>, Rama K. Layek<sup>1</sup>,  
Nam Hoon Kim<sup>5</sup>, Joong Hee Lee<sup>1, 5\*</sup>

Received 00th January 2014,  
Accepted 00th January 2014

DOI: 10.1039/x0xx00000x

www.rsc.org/

Today, one of the major challenges is to provide green and powerful energy sources for a cleaner environment. Rechargeable lithium-ion batteries (LIBs) are promising candidates for energy storage devices, and have attracted considerable attention due to their high energy density, rapid response, and relatively low self-discharge rate. The performance of LIBs greatly depends on the electrode materials; therefore, attention has been focused on designing a variety of electrode materials. Graphene is a two-dimensional carbon nanostructure, which has a high specific surface area and high electrical conductivity. Thus, various studies have been performed to design graphene-based electrode materials by exploiting these properties. Metal-oxide nanoparticles anchored on graphene surfaces in hybrid form have been used to increase the efficiency of electrode materials. This review highlights the recent progress in graphene and graphene-based metal-oxide hybrids for use as electrode materials in LIBs. Particularly, emphasis has been placed on the synthesis methods, structural properties, and synergetic effects of metal-oxide/graphene hybrids towards producing enhanced electrochemical response. These hybrid materials have shown significant improvement in the performance of electrode materials.

### 1. Introduction

In response to the needs of modern society and rapid industrial development, it is necessary to design high-efficiency, environmentally friendly, and low-cost energy sources.<sup>1,4</sup> Conventional energy sources based on combustion technologies are playing a major role in meeting energy needs. Nevertheless, major issues are associated with these sources, such as rapidly increasing prices, environmental consequences, and global climate change. These serious problems have necessitated the development of alternative energy sources. In this regard, biomass,<sup>5</sup> wind,<sup>6</sup> solar cells,<sup>7</sup> fuel cells,<sup>8</sup> high energy density batteries,<sup>9</sup> and supercapacitors<sup>10</sup> are becoming appealing. High energy density batteries, supercapacitors, and fuel cells are based on electrochemical energy conversion and storage principles, and they can fulfill the requirements in applications ranging from portable electronics to heavy electric vehicles. Moreover, these devices are environmentally friendly, as they directly convert chemical energy into electrical energy with little or negligible pollution. Batteries and supercapacitors are electrochemical energy storage devices, whereas fuel cells are electrochemical energy conversion devices.<sup>11-13</sup> Among these various types of energy storage devices, rechargeable LIBs are particularly important. They have revolutionized portable electronic devices, and are presently the dominating power sources used for laptops, digital cameras, camcorders, and cell phones. They can store energy with 2-3 times higher density than that of conventional rechargeable batteries. Since the release of the first commercial LIB product by the Sony Corporation in 1991, they have attracted great attention from both industrial and academic communities. The global market of LIBs is now valued at over 12 billion USD per annum, and is expected to reach ~25 billion USD by 2017.<sup>14</sup> Although LIBs

are attractive energy storage devices with high energy density, their power density is generally low. This low power density is mainly due to the high level of polarization at high charge/discharge rates.<sup>15</sup> In addition, major problems are associated with high cost, charge/discharge cyclic stability, and operability, which are related to the electrode materials. The performance of LIBs significantly depends on the charging/discharging rates, which characterize the migration of electrons and Li<sup>+</sup> through the electrode and electrolyte. Therefore, strategies have focused on the design of new electrode materials to facilitate high transport rates for Li<sup>+</sup>/electrons and to reduce the diffusion length.<sup>16</sup> In order to improve the performance of LIBs, considerable efforts have been made to design different types of electrode materials.<sup>1-3,11-17</sup> Carbon has been widely studied as an electrode material in electrochemical energy storage devices due to its excellent chemical stability, environmental friendliness, and abundance.

Recently, various types of carbon nanostructures and their hybrids have been studied as electrode materials for LIBs, including carbon nanotubes,<sup>18-23</sup> mesoporous carbon/CNTs,<sup>24</sup> carbon fiber/CNTs,<sup>25</sup> carbon nanocages/nanographene shells,<sup>26</sup> CNTs/graphene nanosheets,<sup>27</sup> CNTs/polymer hybrid,<sup>28-29</sup> organic radical polymer/mesocellular carbon foam,<sup>30</sup> activated carbon nanostructures, natural graphite, expanded graphite,<sup>31-40</sup> carbon/silicon hybrids,<sup>31-38</sup> CNTs/silicon hybrid,<sup>39-40</sup> nitrogen-doped porous carbon nanofiber and multi-walled carbon nanotubes (MWCNTs),<sup>41-42</sup> carbon-Li<sub>4</sub>Ti<sub>5</sub>O<sub>12</sub>,<sup>43-46</sup> carbon/manganese oxide,<sup>47-48</sup> carbon/lithium-based spinel-type metal oxide,<sup>49-53</sup> carbon/vanadium oxide,<sup>54-55</sup> carbon/titanium oxide,<sup>56-58</sup> hybrid TiO<sub>2</sub>/α-Fe<sub>2</sub>O<sub>3</sub> with core/shell arrays on carbon,<sup>59</sup> and carbon/SnO<sub>2</sub> hybrids.<sup>60-64</sup>

The discovery of mechanically exfoliated graphene (Novoselov et al.<sup>65</sup> in 2004), a new form of carbonaceous material, has generated immense interests in graphene-based materials for diverse applications in various fields.<sup>66-71</sup> Graphene-based hybrids have been successfully synthesized,<sup>72-78</sup> and their potential has been explored for applications such as biomaterials,<sup>79-80</sup> biosensors,<sup>81-82</sup> environmental applications,<sup>83-84</sup> catalysts,<sup>85-86</sup> photocatalysts,<sup>87-89</sup> solar cells,<sup>90</sup> gas sensors,<sup>91</sup> LIBs,<sup>92-97</sup> supercapacitors,<sup>98-100</sup> fuel cells,<sup>101-102</sup> and electronic devices.<sup>103</sup>

Graphene-based hybrid materials are becoming important for electrochemical energy storage and conversion devices. It is important to understand the advantages and disadvantages of graphene-based hybrid electrode materials for LIBs to control their properties using different synthesis approaches. Although several review articles have been devoted to estimate graphene-based hybrid materials for their application in energy storage and conversion, little attention has been paid to graphene-based metal-oxide hybrid nanostructured as electrode materials for LIBs.<sup>11,96,104-107</sup> Therefore, it was thought worthwhile to review studies on various types of graphene and metal oxide/graphene hybrid nanostructured for electrode materials in LIBs. Recent advances in various types of graphene and metal-oxide/graphene hybrids as electrode materials for LIBs are reviewed in detail. Outlines of the synthesis approaches, structural design, compositional relations, and mechanisms for enhanced electrochemical performance are discussed. This comprehensive review on graphene-based metal-oxide hybrids will provide a general understanding of the present research and a guide for developing electrode materials of LIBs in the near future.

## 2. Principle and mechanism of LIBs

Fig. 1 shows a schematic of an LIB. It operates on the principle of Faradaic reactions in the bulk of the active material, and provides high energy density (120-150 Wh/kg<sub>cell</sub>), much higher than that of a supercapacitor.<sup>108</sup> Typically, an LIB consists of a negative anode (such as graphite), positive cathode (such as LiCoO<sub>2</sub>), and a Li<sup>+</sup>-conducting electrolyte (such as LiPF<sub>6</sub>).<sup>109</sup> The charge/discharge process of LIB involves the reversible insertion and extraction of Li<sup>+</sup> in a host matrix (the cathode or anode). In general, the charging process occurs via the extraction of Li<sup>+</sup> from the cathode and insertion into the anode, whereas the discharging process is associated with the liberation of Li<sup>+</sup> from the anode and is taken up again by the cathode. Basically, three types of electrode systems have been reported, on the basis of the insertion/extraction mechanisms of Li<sup>+</sup>: conversion, insertion, and Li-alloy reactions.<sup>110-112</sup> These reaction mechanisms are given as follows:<sup>111</sup>

Mechanism for the conversion reaction:



Mechanism for the insertion reaction:



Mechanism for the Li-alloy reaction:



The fundamental science and technology of LIBs have been studied extensively and reported in several review articles<sup>9,12,17</sup> and dedicated books.<sup>113-116</sup> LIBs are attractive candidates for power-storage devices and feature high energy density; however, at high charge/discharge rates, they suffer from a high level of polarization and very low solid-state diffusion. LIBs therefore exhibit low power density (100-1000 W/kg) and require several hours of charging time.

The overall device performance, regarding capacity, charging efficiency, and life cycle depends on the properties of the electrode materials. Therefore, significant interest has been given to the research and development of new electrode materials to improve the energy density, rate capability, and cycling stability.<sup>12,15</sup>

## 3. Factors affecting the performance of LIBs

The performance of LIBs basically depends on the development of the materials used for various components. The degradation of these components during the battery operation effectively determines the performance of LIBs. These components undergo different aging mechanisms, such as rusting of the separator or current collector, or decomposition of the binder and electrolyte. Degradation of the electrolyte causes an increase in the internal resistance and a reduction in the reversibility of the electroactive material. The temperature of the cell is another important factor that influences the life cycle of LIBs.

It is known that during the cycling process, a heterogeneous layer is usually formed on the surface of the electrode, which is known as the solid electrolyte interphase (SEI). The SEI forms due to the reduction of the electrolyte species. It acts as an electronically insulating protective layer between the electrolyte and the surface of the electrode; it also has its own advantages, since it prevents further decomposition of the electrolyte. Nevertheless, the SEI layer causes several disadvantages, including (i) low rate of charging and/or the power density, since the diffusion rate of Li<sup>+</sup> through the SEI layer is lower than that within the electrode and electrolyte and (ii) significant loss in capacity due to the consumption of Li<sup>+</sup>. Thus, the performances of LIBs such as irreversible capacity loss, cycle life, Coulombic efficiency, and shelf life greatly depend on the SEI layer. The SEI layer should be well adhered to the electrode material, be insoluble in the electrolyte at elevated temperatures, and also be a good ionic conductor for Li<sup>+</sup> and good electronic insulator. In addition, the solvation shell around the Li<sup>+</sup> needs to be removed to avoid the solvent co-intercalation associated with the exfoliation of active material. Also, the composition of the SEI influences the electronic insulating properties as well as its chemical stability. The thickness, porosity, and morphology of SEI layer, govern the conductivity of Li<sup>+</sup>. Therefore, the quality of the SEI layer can play a crucial role in the overall performance of LIBs. The structural morphology, including the thickness, size, and component of the SEI layer, could be further controlled and its demerits could be minimized through proper surface modification of the electrode material. In this context, graphene and its derivative can play a vital role due to the ease of surface modifications. Furthermore, electrodes face several aging mechanisms that essentially depend on the characteristics of the materials, such as the size of the particles, surface area, crystallinity, morphology, and structural phase. Nevertheless, the main concern is the design and synthesis of the electrode materials for exhibiting high lithium storage capacity.<sup>117</sup>

## 4. An overview of graphene and LIBs

Graphene consists of a monolayer of sp<sup>2</sup>-bonded carbon atoms, which is tightly packed into a hexagonal lattice structure. It is a group of all graphitic carbons that can be rolled into a carbon nanotube or fullerene and forms three-dimensional graphite by the stacking of 2D graphene layers as shown in Fig. 2.<sup>29</sup> Graphene has attracted significant attention from researchers due to its unique electrical, mechanical, and thermal properties that are useful for various potential and technological applications.<sup>118</sup> It has been found that graphene exhibits a large specific surface area (2,630 m<sup>2</sup>g<sup>-1</sup>), excellent intrinsic mobility of carriers at room temperature (200,000 cm<sup>2</sup>V<sup>-1</sup>s<sup>-1</sup>), thermal conductivity (~5,000 Wm<sup>-1</sup>K<sup>-1</sup>), high Young's modulus (~ 1.0 TPa), and excellent optical transmittance (~

97.7%).<sup>119</sup> Particularly, the excellent electrical conductivity and high surface area of graphene has motivated considerable interest for use as an electrode material in LIBs. The theoretical specific surface area of graphene ( $2,620 \text{ m}^2 \text{ g}^{-1}$ ) is significantly higher than those of CNT ( $\sim 1,300 \text{ m}^2 \text{ g}^{-1}$ ) and graphite ( $10 - 20 \text{ m}^2 \text{ g}^{-1}$ ), which can be further helpful for providing an ideal platform for the transportation of  $\text{Li}^+$  and electrons, and more electro-active sites for energy storage. Moreover, the high surface-to-volume ratio and open porous system of graphene is advantageous for fast ion transport, enabling higher rate capability compared to graphite. In addition, the flexibility of graphene compared to brittle graphite is beneficial for constructing flexible energy storage devices.<sup>120</sup> It is believed that the highly conductive nature and interaction of  $\text{Li}^+$  on both sides of graphene can significantly enhance the lithium storage capacity, and that graphene can effectively overtake graphite, its 3D counterpart.<sup>121</sup> Derivatives of graphene such as surface modified graphene or graphene oxide (GO) containing various types of oxygen functional groups can be used as a substrate for the anisotropic growth of metal-oxides/metal nanostructures.<sup>107</sup> Additionally, the aggregation of nanoparticles during the cycling process can be effectively suppressed by using graphene, reduced-GO (RGO), or GO as a substrate or matrix. Thus, the incorporation of graphene into electrode materials can improve the performance of the LIBs significantly.<sup>108</sup>

## 5. Graphene-based electrode materials for LIBs

### 5.1 Graphene nanosheets

Wang et al.<sup>121</sup> synthesized graphene nanosheets (GNS) by oxidizing graphite into GO and subsequent reduction using hydrazine monohydrate. The field emission scanning electron microscopy (FE-SEM) images revealed that the GNS were naturally crumpled into the shape of flower-petals. These GNS based anodes exhibited better lithium storage capacity compared to the original graphite anode. The prepared GNS electrode delivered a specific capacity of  $\sim 945 \text{ mAhg}^{-1}$  in the initial discharging and a reversible capacity of  $\sim 650 \text{ mAhg}^{-1}$  in the first charging. Moreover, it was able to maintain a specific capacity of  $\sim 460 \text{ mAhg}^{-1}$  after 100 cycles.<sup>121</sup> Graphene with a larger specific surface area (and fewer layers) with a curled morphology could provide additional active sites for  $\text{Li}^+$  insertion; it therefore improved the electrochemical performance.<sup>122,123</sup> GNS was synthesized using a wet chemical route and the thermal exfoliation of graphite at different temperatures.<sup>124</sup> It was observed that the GNS synthesized using  $\text{N}_2\text{H}_4$  as the reducing reagent exhibited better electrochemical performances. After 100 cycles, at a current density of  $149 \text{ mA g}^{-1}$ , the specific capacity was maintained at  $\sim 600 \text{ mAhg}^{-1}$  (Coulombic efficiency  $\sim 85\%$  of the first 10 cycles). On the other hand, the electrochemical performance of GNS, prepared using  $\text{KBH}_4$  (GNS- $\text{KBH}_4$ ) and thermal exfoliation at 300, 500, and 800 °C (denoted as GNS-300, GNS-500, GNS-800), was found to be poor.<sup>124</sup> The GNS- $\text{KBH}_4$  and GNS-800 exhibited specific capacity  $\sim 300 \text{ mAhg}^{-1}$  only, at  $149 \text{ mA g}^{-1}$  after 100 cycles. Further, while these authors also tried to establish a correlation between the structural features of these GNSs (e.g., disorder, inter-layer spacing, and specific surface area), unfortunately, no correlation between the structural features and reversible capacity was observed.<sup>124</sup> Xiang et al.<sup>125</sup> also synthesized various types of GNS by oxidizing graphite to different degrees, and subsequently reducing it using thermal or hydrazine assisted treatments. The graphene prepared using a low degree of oxidized GO was observed to be thick with low specific surface area, as investigated through high resolution transmission electron microscopy (HR-TEM), Brunauer-Emmett-Teller (BET) specific surface area, and Raman spectroscopy techniques. In contrast, the GNS synthesized using a

high degree of oxidized GO showed a high specific surface area, disorder features, and sufficient pores. Furthermore, GNS prepared by the thermal treatment of high-grade GO at 1050 °C exhibited a specific surface area of  $492.5 \text{ m}^2 \text{ g}^{-1}$ , which delivered a reversible capacity of  $835 \text{ mAhg}^{-1}$  at  $50 \text{ mA g}^{-1}$  after 45 cycles with a Coulombic efficiency  $\sim 95\%$ . This reversible capacity and cyclic stability was found to be superior to that of the GNS prepared using medium-grade GO under the same conditions, which strongly depends on the specific surface area of GNS.<sup>125</sup> It was assumed that by controlling the morphology, electrochemical performance can also be regulated, whereas GNS containing few layers and relatively low functional groups exhibited better electrochemical performance.<sup>126</sup>

Few-layer GNS ( $\sim 4$  layers) with a specific surface area of  $492.5 \text{ m}^2 \text{ g}^{-1}$  were prepared by the rapid thermal exfoliation of GO at 1050 °C in nitrogen atmosphere.<sup>127</sup> The synthesized GNS exhibited curled morphology with a wrinkled paper-like structure. The XRD results further suggest that the periodic structure of bulk graphite and GO was destroyed in the GNS, suggesting the homogeneous exfoliation of graphitic layers. On the other hand, Fourier transform infrared (FT-IR) spectroscopy investigation revealed the removal of oxygen functional groups from the surface of GO at high temperature. Further, when used as an anode, at a current density of  $100 \text{ mA g}^{-1}$ , the first reversible specific capacity was found to be  $1264 \text{ mAhg}^{-1}$ , whereas after 40 cycles, it was maintained at  $\sim 848 \text{ mAhg}^{-1}$ . Furthermore, when cycled at a high current density of  $500 \text{ mA g}^{-1}$ , the reversible specific capacity  $\sim 718 \text{ mAhg}^{-1}$  was delivered. However, the initial irreversible capacity and large hysteresis observed in the discharge-cycles restrict their use in commercial LIBs.<sup>127</sup> Fang et al.<sup>128</sup> reported a unique approach to synthesis mesoporous GNS. In this method, a solution deposition process was first adopted to synthesize 2D mesoporous carbon nanosheets. These 2D mesoporous carbon nanosheets were prepared using a controlled low-concentration monomicelle close-packing assembly as shown in Fig. 3. These carbon nanosheets consisted of a single layer of ordered-mesopore carbon structure which was investigated through atomic force microscopy (AFM). The formations of mesopores in the GNS were clearly visible in the SEM images as shown in Fig. 4. At a current density  $100 \text{ mA g}^{-1}$ , this mesoporous GNS could deliver a reversible capacity of  $\sim 770 \text{ mAhg}^{-1}$  after 10 cycles. Notably, after the initial 15 cycles, coulombic efficiency reached above 92%, whereas after 60 cycles at a high current density of  $5 \text{ Ag}^{-1}$ , it delivered a reversible capacity of  $\sim 255 \text{ mAhg}^{-1}$  as shown in Fig. 5. In addition, after 60 cycles at different current densities, the capacity was retained at  $\sim 833 \text{ mAhg}^{-1}$ , when the current density was reset at  $100 \text{ mA g}^{-1}$ . Vertically aligned GNS was synthesized using a microwave-assisted plasma-enhanced chemical vapor deposition (CVD) technique, and could be directly used as an electrode without a binder and conductive additives.<sup>129</sup> When it was used as the anode, a reversible capacity of  $\sim 280 \text{ mAhg}^{-1}$  at a current rate of C/0.375 was achieved after 120 cycles. Nevertheless, after cycling at different rates (C/6 to C/0.375) when the current rate was reset at C/1.5, the capacity of  $\sim 320 \text{ mAhg}^{-1}$  (after 175 cycles) could be achieved, which was  $\sim 85\%$  of the capacity (after 50 cycles) at the same current rate. The vertical alignment of graphene with an effective electrical connection to the substrate minimized the electrical resistance and reduced the diffusion distance, which improved the lithium storage kinetics.<sup>130</sup>

The intercalation/deintercalation mechanisms of  $\text{Li}^+$  in GNS, synthesized using chemical methods, has been investigated by Lei et al.<sup>131</sup> It was observed that GNS consisting of 10 layers exhibited an improved reversible capacity along with good cyclic stability. The high irreversible capacity in the first cycle was attributed to the spontaneous stacking of the GNS during the lithiation and the

formation of a solid electrolyte film on the interphases of the GNS electrode and electrolyte. However, the first cycle coulombic efficiencies were found to be only 40.6%. Wei et al.<sup>132</sup> synthesized graphene microspheres composed of multilayer graphene (MMG) using chemical reduction-assisted by thermal treatment. It was observed that the MMG exhibited a capacity superior to the multilayer graphene. After 40 cycles at a current density of  $25 \text{ mA g}^{-1}$ , the capacities were observed to be  $453 \text{ mA h g}^{-1}$  and  $229 \text{ mA h g}^{-1}$  in the cases of MMG and multilayer graphene electrode, respectively. MMG also exhibited high-rate charge/discharge and better cyclic properties compared to MG. The better performance of MMG was attributed to its unique structural features, including (i) spherical structure that allows easy diffusion of  $\text{Li}^+$ , (ii)  $\text{Li}^+$  can be adsorbed on graphene microparticles similar to a “house of cards” in hard carbons and mesocarbon microbeads, and (iii) several cavities composed of graphene microparticles can be largely contributed to the  $\text{Li}^+$  storage. In addition, Pollak et al.<sup>133</sup> studied the interaction of  $\text{Li}^+$  with single-layer and few-layer graphene. The *in-situ* Raman investigations during the electrochemical lithiation process revealed that few-layer GNS resembled a graphite structure. Single-layer graphene behaved differently and exhibited a low degree of  $\text{Li}^+$  absorption on both sides of the graphene layer. Additionally, a study on the lithium intercalation into bilayer graphene by first-principles DFT calculation suggested the existence of AB and AA stacking. The AA staking was found to be more favorable for lithium storage. It has also been suggested that the structural defects can provide better conditions for lithium storage than those of pristine bilayer graphene.<sup>134</sup> On the other hand, the theoretical calculations revealed that the same number of  $\text{Li}^+$  exposed to both sides of GNS could improve the lithium storage capacity.<sup>135-136</sup> Consequently, the single-layer configuration was found to be promising to achieve the safest and most stable LIBs.<sup>137</sup> Kim et al.<sup>138</sup> reported functionalized graphene nanoplatelets as a new type of electrode material with a tunable energy and power density for LIBs. The high power and gravimetric energy density were attributed to the fast faradic reactions between the  $\text{Li}^+$  and functional groups of graphene. Moreover, the presence of a 3D network consisting of a porous morphology facilitates the accessibility of the electrolyte to the electrode. Therefore, functionalized graphene nanosheets could deliver a high energy density of  $260 \text{ Wh kg}^{-1}$ , even at a high power density of  $20 \text{ kW kg}^{-1}$  after 2000 cycles without fading capacity.<sup>138</sup>

### 5.2 Paper-like graphene nanostructures

Mukherjee et al.<sup>139</sup> synthesized free-standing graphene papers (GP) following the photoflash and laser-assisted reduction of GO. In a typical procedure, instantaneous and extensive heating from a photoflash or laser causes the deoxygenation reaction of GO. A rapid outgassing also creates voids, microscale pores, and cracks in the GP, which facilitate efficient intercalation kinetics during the ultrafast charge/discharge rates. These properties significantly enhance the performance of the graphene paper-like electrode. Furthermore, the GP prepared using the photo-reduction method could deliver a storage capacity of  $156 \text{ mA h g}^{-1}$  over 1000 cycles at a charge/discharge rate of 40 C, along with a power density  $10 \text{ kW kg}^{-1}$ . In addition, the photoflash reduced GP retained a Coulombic efficiency of  $\sim 98.5\%$  of the initial capacity for over 50 cycles. Meanwhile, the thermally reduced graphene showed inferior stability and retained a coulombic efficiency of only  $\sim 81.8\%$ .<sup>139</sup> The freeze-drying process of the aqueous dispersion of GO was used to produce a foam-like material, which was further thermally treated under an Ar atmosphere to produce foam-like graphene.<sup>140</sup> This material was directly used as an anode, without using any type of conductive additive or binder during the assembly. At a current density of  $50 \text{ mA g}^{-1}$ , this foam-like graphene material exhibited initial charge and

discharge capacities of  $732$  and  $1059 \text{ mA h g}^{-1}$ , respectively. However, at a higher current density of  $4 \text{ Ag}^{-1}$ , the reversible capacity was found to be  $\sim 140 \text{ mA h g}^{-1}$ . The cycle stability of graphene foam, measured during 100 cycles at a current density  $1 \text{ Ag}^{-1}$ , exhibited a reversible capacity of  $\sim 82\%$  of the initial capacity.<sup>140</sup> It was proposed that the freeze-drying technique may help to increase the inter-layer distance between the graphene layers, thus improving the cycling stability and rate performance.<sup>141</sup> Hu et al.<sup>142</sup> synthesized free-standing GP with different thicknesses ( $\sim 1.5$ ,  $3$ , and  $10 \mu\text{m}$ ) using water-suspended reduced GNS, following a vacuum-assisted filtration method. Cyclic voltammetry studies suggest that the thickness of the GP significantly influences the electrochemical performance and the thinner GP exhibited better performance than the thicker GP. At a current density of  $100 \text{ mA g}^{-1}$ ,  $1.5 \mu\text{m}$  thick GP could deliver an initial reversible specific capacity of  $\sim 200 \text{ mA h g}^{-1}$  (first 10 cycles). In contrast,  $10 \mu\text{m}$  thick GP exhibited a specific capacity of only  $\sim 80 \text{ mA h g}^{-1}$  at a current density of  $50 \text{ mA g}^{-1}$ . In addition, after 100 cycles, a specific capacity of  $\sim 180 \text{ mA h g}^{-1}$  was retained in the case of  $1.5\text{-}\mu\text{m}$ -thick GP, whereas the  $10\text{-}\mu\text{m}$ -thick GP exhibited only  $\sim 65 \text{ mA h g}^{-1}$ . Furthermore, compared to the  $3 \mu\text{m}$  thick GP, the  $1.5 \mu\text{m}$  thick GP retained higher coulombic efficiency and better cyclic stability during the 100 cycles. The inferior performance of the thicker GP was attributed to the lower surface area due to the dense restacking of graphene layers. This stacking of graphene increased the diffusion length through the cross-plane rather than in the plane of the GP.<sup>142</sup> Recently, Dao et al.<sup>143</sup> fabricated super-tough GP via the vacuum filtration of functionalized graphene. In this process, graphene was functionalized with polycaprolactone (PCL) brushes by the polymerization of caprolactone from the functional groups of graphene. The polymer brushes served as physical cross-linkers and gave the graphene paper a very high toughness ( $3.49 \times 10^6 \text{ J m}^{-3}$ ) of 5 times higher than that of un-functionalized graphene. This super-tough GP exhibited a stable discharge capacity of  $\sim 450 \text{ mA h g}^{-1}$  at a current density of  $300 \text{ mA g}^{-1}$ . The cyclic stability was also measured at a current density of  $60 \text{ mA g}^{-1}$  during 50 cycles, which exhibited a Coulombic efficiency of over 95%.

### 5.3 Reduced graphene oxide nanostructures

It has been reported that the large d-spacing and high specific surface area of graphene are not the only factors for enhanced capacity; the existence of surface defects along with functional groups of graphene also improved the electrochemical performances.<sup>144</sup> Depending on the reduction process, the capacity of RGO was found to vary from  $230$  to  $717 \text{ mA h g}^{-1}$ . The reduction procedures significantly influence the degree of reduction of GO and thus the lithium storage capacity. Wang et al.<sup>145</sup> synthesized epoxide-enriched GO; without reduction, it can be used as a promising electrode material for LIB. This electrode material delivered a lithium storage capacity of  $360.4 \text{ mA h g}^{-1}$  at a current density of  $50 \text{ mA g}^{-1}$ . The cycling stability, measured at  $100 \text{ mA g}^{-1}$  over the 60 cycles suggested good stability with Coulombic efficiency of over 100% of the initial capacity. It has been reported that the highly disordered feature of RGO can be beneficial for relatively higher lithium storage. The effect of different structural parameters on the lithium storage properties was systemically studied by Pan et al.<sup>146</sup> They synthesized RGO by the reduction of GO using various methods, such as chemical reduction, electron beam irradiation, and pyrolysis. The experimental results suggest that these methods can produce different degrees of structural disorder or defects in RGO, which remarkably influenced the lithium storage properties. The disordered features were extensively studied using Raman spectroscopy. The electrochemical studies revealed that the additional reversible storage sites such as those at edges and

other defects play a crucial role in enhancing the capacity. Additionally, highly disordered graphene prepared by electron beam irradiation and low-temperature pyrolysis at 300 °C exhibited high reversible capacities of 1054 mAhg<sup>-1</sup> and 1013 mAhg<sup>-1</sup> at 50 mA g<sup>-1</sup>, respectively, much higher than those of the previously reported pure graphene nanosheets (540 mAhg<sup>-1</sup>) and doped graphene nanosheets (730–784 mAhg<sup>-1</sup>).<sup>146,147</sup> In particular, highly disordered graphene nanosheets prepared by low-temperature pyrolysis and electron beam irradiation exhibited an exceptionally high reversible capacity and good cyclic stability. The enhanced capacity in disordered graphene nanosheets was mainly ascribed to additional reversible storage sites such as edges and other defects. Kumar et al.<sup>148</sup> synthesized Li<sup>+</sup> intercalated RGO. The synthesis method involves reduction of GO in the presence of lithium metal and liquid ammonia. Intercalation and binding of Li<sup>+</sup> with RGO was confirmed by X-ray photoelectron spectroscopic analysis. It was suggested that partial intercalations of Li<sup>+</sup> between the layers of RGO can enhance the storage capacity. Therefore, at a current density of 25 mA g<sup>-1</sup>, storage capacities of 300, 340, and 410 mAhg<sup>-1</sup> could be achieved in the cases of graphite, RGO, and Li-RGO electrode, respectively. In addition, compared to graphite and RGO, the Li-RGO electrode showed better cyclic performance (40 cycles) with a Coulombic efficiency of ~85% of initial capacity. Kuo et al.<sup>149</sup> prepared RGO using a controlled chemical and thermal reduction process. The chemical reduction of GO into RGO was performed through the refluxing of GO solution in the presence of hydrazine at 100 °C for 24h, whereas calcinations of GO at different temperatures in the presence of H<sub>2</sub>/N<sub>2</sub> for a period of 2 h yielded the formation of thermally reduced GO. The specific functionalities of RGO were found to dominate the surface defects and large specific surface area for enhancing the reversible capacity. Furthermore, phenol and cyclic edge ether groups were responsible for contributing the capacities over the potential of 1.5 V and in the range of 0.8–1.5 V, respectively. However, other functional groups such as carbonyl, carboxyl, and lactone did not contribute to the reversible lithiation/de-lithiation processes.<sup>149</sup>

#### 5.4 Nitrogen/Boron/Sulfur doped graphene nanostructures

The structural evolution of RGO under different refluxing times was studied by Shen et al.<sup>150</sup> The reduction and functionalization of graphene was achieved in the presence of dimethylformamide at 140 °C using the solvothermal method. The evolution of structural changes was related to the simultaneous N-doping/dangling bonds, and was found to be dependent on refluxing time. Furthermore, it was observed that the increase of refluxing time led to the growth of more topological defects and the presence of less oxygen-containing functional groups as examined through XPS. Therefore, a better reversible Li<sup>+</sup> insertion was observed in electrodes prepared with RGO, subjected to a higher refluxing time. The solvothermally reduced and functionalized RGO exhibited a reversible capacity of 180.1 mAhg<sup>-1</sup> at a current rate of 50 mA g<sup>-1</sup>. However, it showed a poor cyclic stability and thus was not suitable for the electrode material in the LIB.<sup>150</sup> Nitrogen- (N) and Boron (B)-doped graphene materials are expected to enhance the Li-storage capacity. Reddy et al.<sup>151</sup> synthesized N-doped graphene using a liquid precursor based on the CVD technique. Growth was achieved directly on the Cu used as the current collector. This technique allows growth of the N-doped graphene films with a high percentage of pyridinic N atoms, which were found to be responsible for the enhanced Li<sup>+</sup> intercalation. The induced topological defects in N-doped graphene were responsible for increasing the reversible discharge capacity compared to the pristine graphene.<sup>151-152</sup> The thermal treatment of GO at 800 °C (for 2 h) under an ammonia atmosphere was used to produce N-doped graphene. The XPS results revealed 2% N doping,

with the N binding configurations of the graphene including 7.6% graphitic, 35.0% pyrrolic, and 57.4% pyridinic N atoms.<sup>153</sup> At a current density of 42 mA g<sup>-1</sup> (1/20 C), the N-doped graphene electrode exhibited a reversible capacity of 900 mAhg<sup>-1</sup>. Moreover, a rate performance of 250 mAhg<sup>-1</sup> at a current density of 2.1 Ag<sup>-1</sup> (2.5 C) and a significantly enhanced cycling stability, compared to un-doped graphene were also observed. More importantly, when the N-doped graphene electrode was re-cycled at C/10 (after 60 cycles at different current densities), it surpassed the capacity, delivered in the initial 20 cycles.<sup>153</sup> Recently, Cai et al.<sup>154</sup> synthesized highly N-doped graphene (7.04 at.%) via a thermal annealing process. In this process, graphene sheets prepared by rapid thermal expansion were first mixed with melamine through grinding, and the mixture was then subjected to a combustion process at 700 °C under an Ar atmosphere. When used as an electrode, at a current density of 50 mA g<sup>-1</sup>, this N-doped graphene exhibited a high reversible specific capacity of 1123 mAhg<sup>-1</sup>, whereas at a high current density of (20 Ag<sup>-1</sup>), it delivered a capacity ~241 mAhg<sup>-1</sup>.<sup>154</sup>

In N-doped graphene, the effect of the electron deficiency on the electrochemical properties has also been investigated through first-principle calculations using different models such as graphitic, pyrrolic, and pyridinic graphene.<sup>155</sup> Among these, the graphitic structure was found to be the weakest, whereas pyridinic graphene was the most suitable candidate for high Li<sup>+</sup> storage. In the case of a pyridinic structure, a reversible capacity of 1262 mAhg<sup>-1</sup> was observed, which was higher than the experimental value of 1043 mAhg<sup>-1</sup>. The adsorption properties of Li<sup>+</sup> on B-doped graphene were also investigated by DFT.<sup>156</sup> The DFT calculation showed that the doping of boron into graphene makes the system more electron-deficient. Therefore, more Li<sup>+</sup> could be captured around the B-doped centers compared to with pristine graphene, and the lithium storage capacity was dramatically improved. Similarly, the doping of sulfur in graphene based anodes enhanced the capacity and rate performance, making it a promising anode material for lithium-ion batteries.<sup>157</sup> Recently, Yun et al.<sup>158</sup> studied the electrochemical performance of sulfur doped GNS (S-GNS). The S-GNS were prepared by thermal treatment of elemental sulfur and lyophilized GO mixtures. The electrochemical performance of S-GNS was observed to be superior to that of un-doped GNS. The S-GNS exhibited capacities of 285 mAhg<sup>-1</sup> at a rate of 30 C (1 C = 372 mA g<sup>-1</sup>), which was nearly three times higher than that of un-doped GNS. The cycling stability of the S-GNS electrode was measured during the 500 charge/discharge cycles at a rate of 4 C, which showed a capacity of ~300 mAhg<sup>-1</sup> with a Coulombic efficiency of ~75%. This improved rate performance of S-GNS was attributed to superior electrical properties compared to un-doped GNS.

#### 5.5 Graphene/CNT hybrid nanostructures

The layered spacing between graphene influences the accommodation of Li<sup>+</sup>, which can further be controlled by the interaction with fullerenes (C<sub>60</sub>) and carbon nanotubes (CNT).<sup>147</sup> The incorporation of CNT and C<sub>60</sub> in the GNS enhanced the storage capacities to 730 mAhg<sup>-1</sup> and 784 mAhg<sup>-1</sup>, respectively. The storage capacity was found to be higher than that of bare GNS (540 mAhg<sup>-1</sup>). The large d-spacing (0.40 nm) in the cases of the GNS+CNT and GNS+C<sub>60</sub> hybrid electrode were observed to be responsible for the enhanced storage capacity. The electrochemical measurements showed that after 20 cycles, the GNS, GNS+CNT, and GNS+C<sub>60</sub> electrodes retained the reversible capacities of 54%, 66%, and 77%, respectively.<sup>147</sup> A hybrid paper of graphene/CNTs exhibited high mechanical strength and flexibility. This hybrid paper-like electrode (CNT/graphene and optimized ratio of 2:1) delivered the highest Li<sup>+</sup> storage capacities.<sup>159</sup> At a current density of 100 mA g<sup>-1</sup>, a reversible specific capacity of ~375 mAhg<sup>-1</sup> was delivered and over 330

mAhg<sup>-1</sup> was retained even after 100 cycles. The presence of CNTs restricts the restacking of GNS, which simultaneously increases the cross-plane electrical conductivity of the paper and the Li<sup>+</sup> storage capacity. Furthermore, the electrode containing CNTs as a buffer exhibited better performance than the electrodes either containing a graphene buffer or not.<sup>160</sup> Recently, Wang et al.<sup>161</sup> synthesized a CNT/graphene hybrid using the CVD method with a mixture of H<sub>2</sub> and C<sub>2</sub>H<sub>4</sub>, grown on copper foil, which was directly used as the electrode for LIBs [Fig. 6]. The morphological investigations revealed that in this hybrid, CNT behaves similar to pillars between the graphene sheets. The seamless connection between the CNT pillars and graphene significantly enhances the charge transfer in the hybrid system. Therefore, this hybrid could deliver a reversible capacity that varies from 900 mAhg<sup>-1</sup> to 526.26 mAhg<sup>-1</sup> at a current density ranging from 100 mA g<sup>-1</sup> to 900 mA g<sup>-1</sup>. The cycling performance and Coulombic efficiency of this hybrid electrode were tested at a current density of 600 mA g<sup>-1</sup>, and suggested good stability with a Coulombic efficiency of nearly 100% [Fig. 7].

Wang et al.<sup>162</sup> also synthesized a self-assembled layer by layer CNT/GO hybrid, directly grown on copper foil and used as an anode for LIB. These hybrids could store energy up to a different extent, depending on the thickness. It was observed that at a current density of 0.01 mAcm<sup>-2</sup>, an electrode having a thickness of 917.0 nm delivered a reversible capacity of 0.265 mAhcm<sup>-2</sup>. Furthermore, a reversible capacity of 0.030 mAhcm<sup>-2</sup> was observed even at a higher current density of 0.4 mAcm<sup>-2</sup>. It was concluded that such hybrid electrodes having thicknesses of less than one micron might be promising candidates for energy storage in micro devices. Vinayan et al.<sup>163</sup> synthesized a hybrid of graphene and MWCNTs. In this method, graphene synthesized by solar exfoliation and MWCNTs synthesized by CVD were chemically mixed after the surface functionalization. It was observed that the electrostatic interaction between graphene and the MWCNTs effectively suppressed the restacking of graphene, and provided a highly accessible electroactive surface area and a short diffusion path for Li<sup>+</sup>. These properties significantly improved the electrochemical performance of these hybrid electrodes.<sup>163-164</sup> An array structure of 3D-MWCNTs/graphene was fabricated on a flexible and transparent polyethylene terephthalate (PET) film through a lamination process.<sup>165</sup> The 3D column structure of MWCNTs onto graphene-PET film provides good structural integrity and low contact resistance even at high angle bending. When used as an anode, this hybrid exhibited a reversible specific capacity of ~ 250 mAhg<sup>-1</sup> at a current density 63 mA g<sup>-1</sup> along with a good Coulombic efficiency of over 99%.<sup>165</sup> Table 1 summarizes the different types of carbon based electrode materials and their performances in LIBs. It was concluded that in most cases, graphene based electrode materials show their superiority over other materials.

### 5.6 Graphene oxide as the corrosion inhibitor for current collectors in LIB

It has been reported that graphene can also be helpful as a corrosion inhibitor for metals. However, using graphene as a corrosion inhibitor for the current collector in LIBs (with non-aqueous electrolytes) may not be effective. In the case of nonionic graphene, unbiased ionic diffusion of the charges can take place, where an electrolyte would easily be swamped due to the high surface area of graphene. These phenomena may cause a higher rate of corrosion.<sup>166</sup> Prabakar et al.<sup>166</sup> reported that GO can be a better candidate as a corrosion inhibitor for aluminum (Al) current collectors in LIBs. The spin coating of GO onto Al was applied and used as a current collector. The strongly adhered GO on the Al can effectively inhibit the corrosion in the electrolyte. Moreover, the electrochemical results suggested that, compared to uncoated Al, the

GO-coated Al current collector improved the performance of the system in terms of a relatively higher capacity and improved cyclability.

## 6. Metal oxide/graphene hybrid as anode materials

As electrode materials, nanostructured metal oxides have some advantages over bulk materials due to their high specific surface area. The high surface area can significantly improve the electrode/electrolyte interaction, and therefore creating a shorter diffusion length for Li<sup>+</sup> and electrons. However, some disadvantages are associated with the high specific surface area and low thermodynamic stability of the nanoparticles. Moreover, the large variation of volume during the cycling process causes pulverization of the electrode, which results in poor reversibility. It has been observed that the nanomaterials tend to agglomerate due to the high surface energy, and it is therefore very difficult to disperse or mix them with carbon black and binders to produce electrodes. These difficulties cause a higher contact resistance of the electrode compared to the bulk materials. During the cycling process, a pronounced agglomeration is observed and a risk of secondary reactions. These phenomena are associated with electrolyte decomposition between the electrode and electrolyte medium, which results in a high level of irreversibility and poor life cycle.<sup>112</sup> On the other hand, graphene generally suffers from serious agglomeration and restacking due to van der Waals interactions, and consequently causes poor electrochemical performance. The difficulties associated with metal-oxide nanoparticles and graphene could be overcome by fabricating metal-oxide/graphene hybrid materials. Therefore, various types of metal-oxide/graphene hybrid nanostructures have been synthesized and studied as electrode materials for LIBs. In the hybrid state, the nanoparticles increase the space between graphene layers, avoiding the restacking of graphene sheets, and react as active materials to interact with Li<sup>+</sup> ions; meanwhile, graphene avoids the problems of poor conductivity and volume changes of the nanoparticles during the cycling process. Therefore, metal-oxide/graphene hybrids can significantly improve the electrochemical properties of the system compared to their constituents.

### 6.1 Titanium dioxide/graphene hybrid

Titanium dioxide (TiO<sub>2</sub>) is an environmentally friendly transition metal oxide with a stable structure, which makes it an apt anode material for LIBs, despite a low theoretical capacity of 336 mAhg<sup>-1</sup>.<sup>167</sup> However, the poor rate capability, resulting from the inherent poor electrical conductivity (~1×10<sup>-12</sup> Sm<sup>-1</sup>) and high electrical resistance between the electrode and current collector, as well as low ionic conductivity, (~1.2×10<sup>20</sup> S<sup>-1</sup>m<sup>-2</sup>) limits its practical application. In order to improve the electrochemical properties, graphene has been used in hybrid form, which reduces the irreversible heat and internal resistance during the charge/discharge process, thus improving the performance of these hybrid electrode materials.<sup>168-173</sup> Xin et al.<sup>174</sup> synthesized TiO<sub>2</sub>/graphene hybrid nanostructures through chemical method assisted by thermal treatment. In this method, sodium dodecyl benzene sulfonate was used as a surfactant and hydroxyl titanium oxalate as the intermediate for TiO<sub>2</sub>. This hybrid exhibited flower-like TiO<sub>2</sub> nanostructures grown on graphene sheets.<sup>174</sup> The TiO<sub>2</sub>/graphene hybrid could deliver a capacity of 230 mAhg<sup>-1</sup> at 0.1 C (with a current density of 17 mA g<sup>-1</sup>). However, after 45 cycles, at a high rate of 50 C, it delivered a capacity of 80 mAhg<sup>-1</sup> (~ 35% of the initial capacity), which was ~ 30% higher than that of bare TiO<sub>2</sub> (60 mAhg<sup>-1</sup>) electrode. In addition, after this high rate test, the capacity was re-measured at a low rate of 1 C, yet exceeded that measured during the initial cycles at the same rate.<sup>174</sup> Size-tunable surface-

nitridated TiO<sub>2</sub> nanospindles densely immobilized on GNS exhibited characteristics of a highly conductive matrix and boosted the cycling performance of LIBs.<sup>175</sup> In this method, anatase TiO<sub>2</sub> nanospindles of a controlled size were first synthesized via hydrothermal methods, where tubular titanates were used as the self-sacrificing precursors. Subsequently, the synthesized TiO<sub>2</sub> nanospindles were densely dispersed onto functionalized GO through a spontaneous self-assembly process and further annealed in an NH<sub>3</sub> gas flow. The above process led to the formation of a surface nitrated TiO<sub>2</sub>/graphene hybrid (TiO<sub>2</sub>@TiO<sub>x</sub>N<sub>y</sub>/TiN-GS). The TiO<sub>2</sub>@TiO<sub>x</sub>N<sub>y</sub>/TiN-GS hybrid exhibited an initial discharge capacity of ~314 mAhg<sup>-1</sup> at a rate of C/5, which is higher than that of the TiO<sub>2</sub>@TiO<sub>x</sub>N<sub>y</sub>/TiN (~287 mAhg<sup>-1</sup>) anode. This improved electrochemical property was attributed to the conductive nitrated layer on the surface of the TiO<sub>2</sub> nanoparticles and graphene sheet which enhanced the lithium insertion/extraction kinetics. Furthermore, the TiO<sub>2</sub>@TiO<sub>x</sub>N<sub>y</sub>/TiN-GS hybrid delivered the specific capacitances of 166 mAhg<sup>-1</sup>, 150 mAhg<sup>-1</sup>, and 130 mAhg<sup>-1</sup> at a rate of 1C, 3C, and 12C, respectively. In contrast, the TiO<sub>2</sub>@TiO<sub>x</sub>N<sub>y</sub>/TiN hybrid could deliver the specific capacities, only ~149 mAhg<sup>-1</sup>, ~110 mAhg<sup>-1</sup>, and ~86 mAhg<sup>-1</sup> under the same conditions.<sup>175</sup>

A unique 3-D hybrid of graphene and TiO<sub>2</sub> as a binder-free paper was fabricated by Hu et al.<sup>176</sup> In this structure, TiO<sub>2</sub> forms pillars between the graphene layers and significantly enhances the insertion and extraction rate of Li<sup>+</sup>. As a result, compared to bare TiO<sub>2</sub> and graphene, significantly improved electrochemical performance was observed with this hybrid electrode.<sup>176</sup> Li et al.<sup>177</sup> fabricated anisotropic and isotropic TiO<sub>2</sub>/graphene sandwich paper via vacuum filtration route assisted by hydrothermal reaction. A controlled chemical reaction under a hydrothermal condition led to the formation of TiO<sub>2</sub> nanosheets parallel to the surface of the graphene paper. Fig. 8 shows SEM and TEM images of the TiO<sub>2</sub>/graphene hybrid material. It was observed that the anisotropic TiO<sub>2</sub>/graphene hybrid paper electrode exhibited the capacity of 112 mAhg<sup>-1</sup> at a high rate of 100 C (corresponding to 36 s of charge/discharge), which was found to be 3 times higher than that of the isotropic TiO<sub>2</sub>/graphene paper electrode. Moreover, the anisotropic TiO<sub>2</sub>/graphene paper electrode exhibited stable cyclic performance when tested at 10 C up to 100 cycles, much better than that of the isotropic TiO<sub>2</sub>/graphene paper electrode. As shown in [Fig. 9], the anisotropic TiO<sub>2</sub>/graphene paper also demonstrated rate capability superior to the isotropic TiO<sub>2</sub>/graphene paper electrode. This improved performance was ascribed to the easy intercalation of Li<sup>+</sup> into the reactive surface of TiO<sub>2</sub> of the anisotropic TiO<sub>2</sub>/graphene hybrid paper electrode during the electrochemical process. Qiu et al.<sup>178</sup> synthesized a TiO<sub>2</sub>/RGO hybrid using a TiO<sub>2</sub> assisted photo-catalytic reaction approach. Using this method, a homogeneous suspension of pre-synthesized TiO<sub>2</sub> nanoparticles and GO was placed under the UV irradiation, which leads to the formation of a TiO<sub>2</sub>/RGO hybrid. The TiO<sub>2</sub>/RGO hybrid exhibited a reversible charge and discharge capacity of 270 and 310 mAhg<sup>-1</sup> (at a current density 100 mA g<sup>-1</sup>), respectively, which was better than that of TiO<sub>2</sub>/GO and bare TiO<sub>2</sub> nanoparticles electrode. In addition, the TiO<sub>2</sub>/RGO hybrid electrode delivered a capacity of ~200 mAhg<sup>-1</sup>, even after 100 cycles and shows a good rate performance. It has also been reported that the graphene improves the thermal stability of the hybrid electrode and prevents the phase transformation in TiO<sub>2</sub>; i.e., from monoclinic [TiO<sub>2</sub> (B)] to anatase.<sup>179</sup> The specific capacity in the TiO<sub>2</sub>-(B)/graphene hybrid was observed to be 215, 182, and 150 mAhg<sup>-1</sup> at the current rates of 1, 5, and 10 C, respectively. On the other hand, bare TiO<sub>2</sub> (B) exhibited the specific capacity of 184, 121, and 99 mAhg<sup>-1</sup> at 1, 5, and 10 C, respectively. The cycling performance of TiO<sub>2</sub>-(B)/graphene hybrid and bare

TiO<sub>2</sub>-(B) electrode were examined at 1 C for 100 cycles. The TiO<sub>2</sub>-(B)/graphene hybrid electrode exhibited a discharge capacity starting at 232 mAhg<sup>-1</sup> and retained ~189 mAhg<sup>-1</sup> after 100 cycles, with a capacity loss of 18%. In contrast, the bare TiO<sub>2</sub>-(B) electrode showed much faster decay in capacity with a loss of 49% under the same conditions.<sup>179</sup> This superior performance in the TiO<sub>2</sub>-(B)/graphene hybrid electrode was ascribed to the enhanced electrical conductivity and better accommodation to volume/strain change during the cycling process.<sup>180</sup>

Recently, Li et al.<sup>181</sup> synthesized graphene nanoscrolls encapsulated TiO<sub>2</sub> (B) nanowires through a self-scrolling and template-free approach via a hydrothermal route followed by ion-exchange and subsequent heat treatment. TEM investigations revealed that GNS encompassed the TiO<sub>2</sub> (B) nanowires to construct nanoscrollled architectures. The electrochemical measurement revealed that this hybrid electrode delivers a reversible specific capacity of 153 mAhg<sup>-1</sup> after 300 cycles at 10 C and retains a capacity of ~94%, which was much higher than that of the bare TiO<sub>2</sub> (B) (60 mAhg<sup>-1</sup>) electrode. Furthermore, it has been proposed that the porous nanoscrollled architectures expedite the transportation of Li<sup>+</sup> and alleviate the volume change during the process of lithiation and delithiation, thus improving the electrochemical performance of the hybrid electrode. The unique structural morphology of TiO<sub>2</sub> nanowires/graphene may demonstrate that it is a promising electrode material for LIBs.<sup>182</sup> A hydrothermal method was used to prepare the hybrid of TiO<sub>2</sub>/mesoporous 3D-graphene aerogels (GAs).<sup>183</sup> This hybrid was composed of TiO<sub>2</sub> single nanocrystals, uniformly grown on the surface of GAs. In the synthesis method, glucose was used as the linker and face-controlling agent, which led to the growth of (001) facets TiO<sub>2</sub> and a hierarchical mesoporous structure. The TiO<sub>2</sub>/GAs hybrid electrode exhibited a high rate capability, and cycling stability for LIBs compared to bare TiO<sub>2</sub>. The TiO<sub>2</sub>/GAs hybrid could deliver a capacity of 200 mAhg<sup>-1</sup> at a current density 0.1 Ag<sup>-1</sup> after 50 cycles, whereas a reversible capacity of 99 mAhg<sup>-1</sup> was delivered at a very high rate of 5 Ag<sup>-1</sup>. These reversible capacities were 4 times higher than that of bare TiO<sub>2</sub> nanocrystals electrode, achieved under the same condition. The doping of N further enhances the electrical conductivity and leads to more defects, therefore significantly improving the electrochemical performance of the N-TiO<sub>2</sub>/graphene hybrid compared to TiO<sub>2</sub>/graphene, TiO<sub>2</sub>, and graphene electrode.<sup>184-186</sup> Ban et al.<sup>187</sup> fabricated TiO<sub>2</sub>/graphene hybrid through atomic layer deposition (ALD) techniques. In order to avoid the poor nucleation of TiO<sub>2</sub>, a layer of Al<sub>2</sub>O<sub>3</sub> was initially deposited onto the graphene using the ALD technique, where the Al<sub>2</sub>O<sub>3</sub> adhesion layers were nearly amorphous in nature. The TiO<sub>2</sub>/graphene hybrid electrode could deliver a capacity of ~120 mAhg<sup>-1</sup> at a high current density of 1 Ag<sup>-1</sup> and retained 95% of the initial capacity, even after 500 charge/discharge cycles. In addition, when cycled at different current rates (after 100 cycles) it delivered a reversible capacity of ~175 mAhg<sup>-1</sup> at 100 mA g<sup>-1</sup>, which was nearly the same when measured after 20 cycles. Menéndez et al.<sup>188</sup> synthesized titania nanotubes (nt-TiO<sub>2</sub>)/RGO hybrid using an electro-deposition technique. In this method, amorphous TiO<sub>2</sub> nanotubes were first grown on TiO<sub>2</sub> foil through the electrochemical anodization process. Graphene was then electrophoretically deposited on the surface of nt-TiO<sub>2</sub>. The FE-SEM micrographs of nt-TiO<sub>2</sub>, obtained through the anodization of Ti foil revealed that the nanotubes were self-arranged with open mouths. The diameter and length of the nanotubes were about 50-80 nm and 5 μm, respectively. Subsequently, the deposition of graphene covered the mouths of nt-TiO<sub>2</sub> with a 100 nm thick flat surface. The nt-TiO<sub>2</sub>/RGO hybrid electrode retained capacities values > 200 mAhg<sup>-1</sup> after 100 cycles for 1.0-2.6 V of potential range and > 300 mAhg<sup>-1</sup> for 0.0-3.0 V. Also, the capacities

of 200 mAhg<sup>-1</sup>, 100 mAhg<sup>-1</sup>, and 50 mAhg<sup>-1</sup> were achieved at rates of 15 C, 85 C, and 300 C, respectively.

## 6.2 Iron oxides/graphene hybrid

Iron oxide, particularly Fe<sub>2</sub>O<sub>3</sub> and Fe<sub>3</sub>O<sub>4</sub>, is considered to be one of the most important and promising anode materials due to its natural abundance, non-toxicity, and low cost. Fe<sub>3</sub>O<sub>4</sub> possesses a high theoretical capacity of 924 mAhg<sup>-1</sup>, whereas that of Fe<sub>2</sub>O<sub>3</sub> is 1005 mAhg<sup>-1</sup>. However, during the cycling process, a large volume change usually occurs, which results in rapid fading of the capacity. In order to improve the reversible capacity and rate capability of the electrodes, graphene has been used as a conductive additive with these nanoparticles.<sup>189-195</sup> Recently, Fe<sub>3</sub>O<sub>4</sub>/graphene hybrids have been extensively studied as anode materials for LIBs.<sup>196-210</sup> Yang et al.<sup>211</sup> synthesized iron oxide nanoribbons/graphene hybrid nanostructured by the controlled nucleation and growth of the iron precursor onto the surface of RGO and following the post calcination treatment at different temperatures (250-400 °C). It was observed that in the hybrid form, the unique structural features of iron oxide nanoribbons, including a large aspect ratio, porous structure, and enhanced open-edge, results in electrochemical performance superior to bare iron oxide nanostructured. This hybrid could deliver a reversible capacity of 1046 mAhg<sup>-1</sup> at a current density of 74 mA g<sup>-1</sup> during the initial charging process, and maintained nearly 100% even after 130 cycles. Moreover, after 30 cycle capacities, reversible capacities of ~ 900 mAhg<sup>-1</sup>, 615 mAhg<sup>-1</sup>, and 400 mAhg<sup>-1</sup> were achieved at high current densities of 372, 1860, and 3720 mA g<sup>-1</sup>, respectively. This improved electrochemical performance of the Fe<sub>3</sub>O<sub>4</sub>/graphene hybrid was attributed to the fact that Fe<sub>3</sub>O<sub>4</sub> nanoparticles act as redox sites and spacers. Moreover, the 3D architecture of the hybrid effectively facilitates the ionic diffusion of Li<sup>+</sup>, and improves the storage capacity.<sup>212-213</sup> Using the *in-situ* thermal decomposition of Fe(NO<sub>3</sub>)<sub>3</sub>·9H<sub>2</sub>O, mesoporous iron oxide (MIO) nanofilm was directly grown on GNS.<sup>214</sup> The SEM and TEM investigations revealed that in the MIO/GNS hybrid, GNS were tightly sandwiched between the MIO nanofilms with an average thickness of ~7 nm. The mesoporous structure partially accommodates the lithiation-induced strain and assists the access of the electrolyte while improving the Li<sup>+</sup> diffusion. Consequently, this hybrid electrode exhibited an excellent cycling stability and rate capability with negligible fading of capacity. At a current density of 100 mA g<sup>-1</sup>, this hybrid electrode delivered a high specific capacity of 1000 mAhg<sup>-1</sup> with a Coulombic efficiency of ~ 100% after 400 cycles.<sup>214</sup> Besides, microsphere-type Fe<sub>3</sub>O<sub>4</sub> with an interstitial cluster structure allows for better percolation of the electrolyte, and efficient accommodation with stress and strain of volume change. Therefore, the electrochemical performance of the Fe<sub>3</sub>O<sub>4</sub>/pyrolytic GO hybrid was significantly improved compared to the bare Fe<sub>3</sub>O<sub>4</sub> nanoparticles electrode.<sup>215</sup> Luo et al.<sup>216</sup> fabricated 3-D graphene foam supported by a mesoporous Fe<sub>3</sub>O<sub>4</sub> nanostructure, using a bottom-up strategy with ALD. In this method, the bi-continuous mesoporous nanostructure of Fe<sub>3</sub>O<sub>4</sub> was deposited on the GNS using ZnO sacrificial layer assisted hydrolysis. Fig. 10 shows a schematic diagram of the sample structure. Due to the unique bicontinuous mesoporous structure, the 3-D graphene/Fe<sub>3</sub>O<sub>4</sub> hybrid electrode exhibited a capacity of ~ 785 mAhg<sup>-1</sup> at a 1C discharge/charge rate and maintained this capacity even up to 500 cycles. Also, a capacity of 800 mAhg<sup>-1</sup> was measured when the C rate was reduced from 60 C to 1C (after 60 cycles), implying a good stability and excellent reversibility. As shown in Fig. 11, the cyclic capacity profiles at rates of 6 C and 10 C measured during 500 cycles were reasonable and were retained at ~400 and 300 mAhg<sup>-1</sup>, respectively.

Zhao et al.<sup>217</sup> synthesized graphene nanoscroll wrapped on Fe<sub>3</sub>O<sub>4</sub> nanoparticles with a 1D tubular form resembling that of the

MWCNT structure. This method involved quenching of GO in the presence of Fe<sub>3</sub>O<sub>4</sub> nanoparticles in liquid nitrogen. It was observed that the wrapping structures depend on several factors, including the zeta potential of Fe<sub>3</sub>O<sub>4</sub> nanoparticles, the initial temperature of the mixed solution, and the mode of quenching. Moreover, the wrapping structures greatly influence the electrochemical performance, and the 1D wrapping was more favorable over 2D wrapping for better lithium storage. The hybrid electrode with 1D wrapping of graphene on Fe<sub>3</sub>O<sub>4</sub> nanoparticles delivered a capacity of ~ 1010 mAhg<sup>-1</sup> at 0.1 C (100 mA g<sup>-1</sup>) after 50 cycles and retained about 300 mAhg<sup>-1</sup> at a high rate of 5 C, which was ~ 33% of the initial capacity, measured at 0.1 C. In contrast, the 2D wrapped Fe<sub>3</sub>O<sub>4</sub>/graphene hybrid exhibited a capacity of ~ 840 mAhg<sup>-1</sup> at 0.1 C after 50 cycles. Chen et al.<sup>218</sup> synthesized an  $\alpha$ -Fe<sub>2</sub>O<sub>3</sub>/graphene hybrid using an *in-situ* wet chemical method under atmospheric pressure. The SEM/TEM studies revealed that this hybrid comprised of 3D quasi-laminated architecture, where  $\alpha$ -Fe<sub>2</sub>O<sub>3</sub> nanoparticles with a diameter of ~ 130 nm were homogeneously anchored on the GNS. The cycling performance of bare  $\alpha$ -Fe<sub>2</sub>O<sub>3</sub> and  $\alpha$ -Fe<sub>2</sub>O<sub>3</sub>/graphene hybrid electrode were measured at a current density of 100 mA g<sup>-1</sup> for 50 cycles. The experimental measurements revealed that the bare  $\alpha$ -Fe<sub>2</sub>O<sub>3</sub> nanoparticle electrode lost its capacity from 809 mAhg<sup>-1</sup> to 97 mAhg<sup>-1</sup>, which was only ~ 6% of the initial capacity, suggesting poor capacity retention. In contrast, the  $\alpha$ -Fe<sub>2</sub>O<sub>3</sub>/graphene hybrid electrode exhibited a relatively high discharge capacity of ~ 827 mAhg<sup>-1</sup> in the second cycle. Subsequently, the capacity slowly dropped to 742 mAhg<sup>-1</sup> during the first 30 cycles, and then stabilized at ~ 742 mAhg<sup>-1</sup> without further loss in capacity up to the 50<sup>th</sup> cycle. This improved performance was ascribed to the combined effects of the 3D quasi-laminated, flexible architecture and the highly conductive/good structural stability of electrode due to the presence of graphene.<sup>218</sup> Using the ferrous ions as both a reducing agent and iron source, the synthesis of Fe<sub>2</sub>O<sub>3</sub>/graphene hybrids was reported by Zhang et al.<sup>119</sup> With this synthesis approach, a mixture of GO, FeCl<sub>2</sub>, and urea was refluxed under ambient conditions using a microwave heater and subsequent heat treatment at 493 K under an Ar atmosphere. The morphological studies further suggest that Fe<sub>2</sub>O<sub>3</sub> nanoparticles (~50 nm) were firmly wrapped by graphene sheets resembling crumpled paper. When used as the anode material, this hybrid electrode delivered a reversible capacity of 800 mAhg<sup>-1</sup> at a charge/discharge rate of 0.2 after 100 cycles. In addition, after 30 cycles, a capacity of as high as 420 mAhg<sup>-1</sup> at a rate of 5 C was achieved.

Recently, Yang et al.<sup>220</sup> fabricated self-assembled 3-D nanoporous Fe<sub>2</sub>O<sub>3</sub>/Fe<sub>3</sub>C-graphene heterogeneous thin films using the CVD technique. It was observed that the electrode kinetics during the Li<sup>+</sup> insertion/extraction was significantly improved due to the formation of a graphene protective shell and a heterogeneous structure in the thin film. This hybrid exhibits enhanced cyclability and rate capacity compared to that of pristine Fe<sub>2</sub>O<sub>3</sub>. The specific capacity of 1118 mAhg<sup>-1</sup> was obtained at a discharge current density of 0.17 C with 88% retention after 100 cycles, whereas 518 mAhg<sup>-1</sup> at a discharge current density of 6.6 C for 1000 cycles. Furthermore, a power density of 1834 Wkg<sup>-1</sup> and an energy density of 924 Whkg<sup>-1</sup> could also be attained. Wang et al.<sup>221</sup> synthesized a hybrid electrode of Fe<sub>2</sub>O<sub>3</sub>/graphene sheet aerogels using a solvothermal-induced self-assembly approach. The Fe<sub>2</sub>O<sub>3</sub>/graphene sheet aerogels hybrid consists of an interconnected macroporous framework where the Fe<sub>2</sub>O<sub>3</sub> nanoparticles are uniformly dispersed on GNS. Due to the unique macroporous structures, high electrical conductivity, and large specific surface area, this hybrid electrode showed a superior rate capability (930 and 520 mAhg<sup>-1</sup> at current density of 500 and 4000 mA g<sup>-1</sup>, respectively) and prolonged cycling stability at high rates (733 mAhg<sup>-1</sup> at current density of 2000 mA g<sup>-1</sup> for 1000

cycles). It has also been reported that the sheet type nanostructured  $\text{Fe}_2\text{O}_3$  encapsulated with GNS are more beneficial than the spherical nanoparticles and exhibit superior electrochemical performance for lithium storage.<sup>222</sup> Wu et al.<sup>223</sup> synthesized  $\text{Fe}@\text{Fe}_2\text{O}_3$  (core-shell) nanoparticles/graphene hybrid via a hydrothermal route followed by an *in-situ* thermal reduction process. This hybrid exhibits a 3D porous structure, where the shell region of  $\text{Fe}@\text{Fe}_2\text{O}_3$  consisted of amorphous  $\text{Fe}_2\text{O}_3$ . The electrochemical measurements suggest that the  $\text{Fe}@\text{Fe}_2\text{O}_3$ /graphene hybrid electrode delivered a reversible charge capacity of  $959.3 \text{ mAhg}^{-1}$  at a current density of  $100 \text{ mA g}^{-1}$  for up to 90 cycles. Additionally, the  $\text{Fe}@\text{Fe}_2\text{O}_3$ /graphene hybrid exhibits long-life cycling performance at high current density. When the current density was increased to  $2000 \text{ mA g}^{-1}$ , the  $\text{Fe}@\text{Fe}_2\text{O}_3$ /graphene hybrid electrode achieved a reversible capacity of  $524.8 \text{ mAhg}^{-1}$  after 200 cycles. Further, when the current was reduced to the initial rate of  $100 \text{ mA g}^{-1}$  (after 66 cycles), this hybrid electrode recovered to a slightly higher capacity ( $1090 \text{ mA g}^{-1}$  for the 125 cycles), thus suggesting a good reversibility and its suitability as a high rate anode material.

Doping of nitrogen into graphene is another possible approach to enhance the performance of the  $\text{Fe}_2\text{O}_3$ /graphene hybrid for lithium storage. The uniqueness of the hybrid including thin nanoplatelets and sandwiched space helps in the buffering of the volume expansion, which results in a high reversible capacity of  $1100 \text{ mAhg}^{-1}$  after 50 cycles at a rate of C/5.<sup>224</sup> Moreover, a specific capacity was achieved as high as  $887 \text{ mAhg}^{-1}$ ,  $739 \text{ mAhg}^{-1}$ , and  $531 \text{ mAhg}^{-1}$  when the current density was increased to 1C, 2C, and 5C, respectively. In contrast, the un-doped  $\text{Fe}_2\text{O}_3$ /graphene hybrid electrode could deliver relatively low capacity ( $135 \text{ mAhg}^{-1}$  at a rate of 1C) even after only 15 cycles.<sup>224</sup> This improved electrochemical performance was attributed to the small particle size of  $\text{Fe}_2\text{O}_3$  and improved electronic conductivity due to the doping of N in graphene, which causes a synergistic effect.<sup>225</sup> Hu et al.<sup>226</sup> synthesized porous  $\text{Fe}_2\text{O}_3$  nanorods anchored on N-doped graphene ( $\text{Fe}_2\text{O}_3$ /N-graphene) by a hydrothermal route, assisted by microwave treatment. The  $\text{Fe}_2\text{O}_3$ /N-graphene hybrid was further coated with ultrathin  $\text{Al}_2\text{O}_3$  film through the ALD technique. The electrochemical results suggest that the coating of  $\text{Al}_2\text{O}_3$  onto  $\text{Fe}_2\text{O}_3$ /N-graphene improved the rate performance, cycling stability, and Coulombic efficiency. The  $\text{Al}_2\text{O}_3$  coated  $\text{Fe}_2\text{O}_3$ /N-graphene hybrid electrode exhibited a stable capacity of  $508 \text{ mAhg}^{-1}$  at a current density of  $2 \text{ Ag}^{-1}$  during 200 cycles. Moreover, a capacity of  $\sim 249 \text{ mAhg}^{-1}$  at a current density of  $20 \text{ Ag}^{-1}$  was maintained without capacity fading for 2000 cycles as shown in [Fig. 12]. This improved electrochemical performance was attributed to the porous structure of the  $\text{Fe}_2\text{O}_3$  nanorods, N-doped graphene framework, and ultrathin coating of  $\text{Al}_2\text{O}_3$ . Recently, a non-aqueous sol-gel method was used to synthesize iron oxide/RGO hybrids in the presence of organic solvents (such as benzyl alcohol), following microwave treatment.<sup>227</sup> The relationship between the structural properties and electrochemical performance of the iron oxide/RGO hybrids was thoroughly investigated using XPS and Raman spectroscopy. It was concluded that GO having features of homogeneity and fewer defects exhibited better electrochemical performance, even at high current density. In addition, it was suggested that poly (acrylic acid) acts as an efficient binder for  $\gamma\text{-Fe}_2\text{O}_3$ /RGO hybrid electrodes and the specific hybrid structures of  $\gamma\text{-Fe}_2\text{O}_3$ /RGO significantly suppress the agglomeration of nanoparticles and provide buffering spaces.<sup>227-229</sup> Therefore, a reversible capacity of  $690 \text{ mAhg}^{-1}$  for up to 100 cycles even at a high current density of  $500 \text{ mA g}^{-1}$  was achieved by the  $\gamma\text{-Fe}_2\text{O}_3$ /RGO hybrid electrode. Furthermore, this hybrid exhibited good rate capability of  $280 \text{ mAhg}^{-1}$  at a current rate of 10C ( $10,000 \text{ mA g}^{-1}$ ) after 35 cycles.<sup>227</sup>

Chen et al.<sup>230</sup> studied the electrochemical performance of  $\text{Fe}_2\text{O}_3$ /CNT/graphene hybrid materials for LIB. The  $\text{Fe}_2\text{O}_3$ /CNT/GNS hybrid was synthesized using the CVD technique. In the synthesis process, a colloidal solution of GO and  $\text{Fe}(\text{NO}_3)_3 \cdot 9\text{H}_2\text{O}$  were mixed using ultra-sonication. This mixed solution was further dried in a vacuum oven at  $80^\circ\text{C}$  to obtain a precursor of  $\text{Fe}(\text{NO}_3)_3$ /GO. Subsequently, this precursor was heated at  $550^\circ\text{C}$  in a tubular furnace with Ar flow.  $\text{C}_2\text{H}_2$  gas ( $\text{C}_2\text{H}_2$ : 10%, Ar: 90%) was then introduced before the furnace was gradually cooled to room temperature in an Ar atmosphere. The obtained product was once again calcined at  $400^\circ\text{C}$  for 2h in air to fabricate the  $\text{Fe}_2\text{O}_3$ /CNT/GNS hybrid material.<sup>230</sup> This hybrid electrode exhibited the specific capacity of  $984 \text{ mAhg}^{-1}$  at a current density of  $74.4 \text{ mA g}^{-1}$  in the first cycle and maintained  $\sim 812 \text{ mAhg}^{-1}$  after 100 cycles. Furthermore, when the current density was increased to  $3720 \text{ mA g}^{-1}$  (5C), it achieved a reversible capacity of  $534 \text{ mAhg}^{-1}$  and maintained  $403 \text{ mAhg}^{-1}$  after 100cycles, with a retention ratio of 75.5%. On the other hand, bare  $\text{Fe}_2\text{O}_3$  electrode could only deliver a reversible capacity of  $112 \text{ mAhg}^{-1}$  at a current density of  $74.4 \text{ mA g}^{-1}$  after 100 cycles. The enhanced electrochemical properties were ascribed to the short path for the diffusion of  $\text{Li}^+$  through the bamboo-like CNTs and the extra lithium storage sites provided by the arc-like graphene layers inside the CNTs. The flexible and highly conductive GNS and open 3D architecture also contribute to improve the electrochemical performance.<sup>230-233</sup> Lee et al.<sup>234</sup> synthesized a bio-inspired 3D hierarchical structure based on graphene, carbon nanotubes, and iron oxide using a microwave-assisted irradiation method. In this 3D hierarchical structure, nanostructured CNTs were vertically grown on a graphene sheet and some of the iron nanoparticles were decorated on both the CNTs and the graphene surface. This hybrid electrode could deliver a reversible capacity of  $\sim 1024 \text{ mAhg}^{-1}$  at a current density of  $100 \text{ mA g}^{-1}$  with a 99% Coulombic efficiency after 40 cycles. The coating of carbon onto the surface of  $\text{Fe}_2\text{O}_3$  (core-shell type structure) in the presence of graphene can significantly improve the performance of the anode materials compared to bare  $\text{Fe}_2\text{O}_3$  and  $\text{Fe}_2\text{O}_3$ /graphene hybrid electrode.<sup>235</sup>

### 6.3 Tin oxide/graphene hybrid

Tin oxide ( $\text{SnO}_2$ ) exhibits a high theoretical  $\text{Li}^+$  storage capacity of  $782 \text{ mAhg}^{-1}$ , more than double that of graphite ( $372 \text{ mAhg}^{-1}$ ). Therefore, it could be a better replacement for the carbon in LIBs. However, during the cycling process, a large volume change of  $\sim 300\%$  causes cracking and degeneration of the electrode, which leads to inferior electrochemical performance. Enhanced lithium storage capacities have been achieved in  $\text{SnO}_2$ /graphene hybrid electrode compared to bare  $\text{SnO}_2$ .<sup>236-246</sup> Kim et al.<sup>247</sup> synthesized  $\text{SnO}_2$ /graphene hybrid using a pH-controlled chemical method. In this synthesis method, tuning of the electrostatic attraction between the GNS and echinoid-like  $\text{SnO}_2$  particles under a controlled pH leads to the growth of uniformly dispersed  $\text{SnO}_2$  nanoparticles over the wrinkled GNS. Combined studies through SEM, TEM, and Zeta potential measurements suggest that a more uniform growth of  $\text{SnO}_2$  nanoparticles on the graphene could be achieved when the surface charge of  $\text{SnO}_2$  and graphene were opposed. This hybrid electrode exhibited a Coulombic efficiency of 98% and a reversible capacity  $634 \text{ mAhg}^{-1}$  at a current density of  $0.1 \text{ Ag}^{-1}$  after 50 cycles. Furthermore, after cycling at different rates, the reversible capacity of  $\sim 389 \text{ mAhg}^{-1}$  at a current density of  $2 \text{ Ag}^{-1}$  was achieved.<sup>247</sup> It has also been observed that the initial source of tin ( $\text{Sn}^{2+}$  or  $\text{Sn}^{4+}$ ) affects the morphology and electrochemical performance of these hybrids.<sup>248</sup> GO plays a critical role in the oxidation of  $\text{Sn}^{2+}$  to  $\text{Sn}^{4+}$ , and the growth of  $\text{SnO}_2$ , rather than  $\text{SnO}$ , was observed in the presence of GO. The electrochemical

performance was found to be better when  $\text{Sn}^{2+}$  was used as the initial source.<sup>248</sup> Chen et al.<sup>249</sup> also reported that precursors of tin influence the electrochemical performance. It was observed that the  $\text{SnO}_2/\text{graphene}$  hybrids, synthesized using stannous oxalate as the tin precursor exhibited better electrochemical performance compared to  $\text{SnCl}_4$ . In addition, a change in the ratio of GO to  $\text{Sn}^{2+}$  also influenced the morphology of the  $\text{SnO}_2/\text{GNS}$  hybrids, and the better electrochemical performance was the result of the proper dispersion of  $\text{SnO}_2$  nanoparticles over the large GNS.<sup>250-263</sup> Thomas et al.<sup>264</sup> observed that the phase of tin oxide also varies with morphology, and the  $\text{SnO}$  phase with the nanoplates morphology exhibited higher discharge capacity and Coulombic efficiency. Furthermore, the platelet type morphology of  $\text{SnO}$  shows better reversible capacity compared to spherical nanoparticles of  $\text{SnO}_2$ . At a current density of  $23 \mu\text{Acm}^{-2}$ , the initial discharge capacity for the  $\text{SnO}@/\text{GNS}$  and  $\text{SnO}_2@/\text{GNS}$  hybrid electrodes was observed to be 1393 and 950  $\text{mAhg}^{-1}$ , respectively. After 40 cycles, a stable capacity of 1022 and 715  $\text{mAhg}^{-1}$  was achieved at a current rate of  $23 \mu\text{Acm}^{-2}$  for the  $\text{SnO}@/\text{GNS}$  and  $\text{SnO}_2@/\text{GNS}$  hybrids, respectively. Meanwhile, Coulombic efficiency for the  $\text{SnO}@/\text{GNS}$  and  $\text{SnO}_2@/\text{GNS}$  hybrids were 94% and 89%, respectively.<sup>264</sup>

Ara et al.<sup>265</sup> prepared  $\text{SnO}_2/\text{graphene}$  hybrids by varying the content of  $\text{SnO}_2$  (25, 43, 60, and 82 wt%) through a controlled hydrothermal synthesis route. The TEM investigation suggests that the 25/75 wt%  $\text{SnO}_2/\text{graphene}$  hybrid shows better dispersion of the particles (2-3 nm) along with  $\sim 2$  nm inter-particle spacing. However, a higher content of  $\text{SnO}_2$  led to a relatively larger particle size and reduction of the inter-particle spacing. Furthermore, the 25/75 wt%  $\text{SnO}_2/\text{graphene}$  hybrid could deliver an enhanced specific capacity of  $\sim 662 \text{mAhg}^{-1}$  at  $50 \text{mA}^{-1}$  after 150 cycles, and better rate capability of 230, 445, and 525  $\text{mAhg}^{-1}$  at current densities of 1000, 500, and 300  $\text{mA}^{-1}$ , respectively. The TEM and EIS results further suggest that after 100 cycles, the nanoparticles retained their original size (2-3 nm) and the charge transfer resistance was decreased by 52%.<sup>265</sup> Investigations of the effects of the structural phase/crystallinity on the electrochemical performance of the  $\text{SnO}_2/\text{graphene}$  hybrid suggest that the amorphous-type  $\text{SnO}_2/\text{GNS}$  could effectively buffer the shrinkage of the Sn lattice and volume expansion. Therefore, the amorphous-type  $\text{SnO}_2/\text{GNS}$  hybrid was found to be more effective over the crystalline  $\text{SnO}_2/\text{GNS}$  hybrid for better lithium storage.<sup>266-269</sup> Lin et al.<sup>270</sup> synthesized  $\text{SnO}_2/\text{graphene}$  nanoribbon hybrid material. In this synthesis method, graphene nanoribbons (GNRs) were prepared by unzipping MWCNTs using sodium/potassium; chemical treatment of GNRs in the presence of  $\text{SnCl}_2 \cdot 2\text{H}_2\text{O}$  and 2-pyrrolidinone was then performed, which lead to the formation of  $\text{SnO}_2/\text{GNR}$  hybrids. The  $\text{SnO}_2/\text{GNR}$  hybrid electrodes exhibited a reversible capacity of  $\sim 825 \text{mAhg}^{-1}$  at a current density of  $100 \text{mA}^{-1}$ , even after 50 cycles with a Coulombic efficiency of  $\sim 98\%$ . Moreover, the  $\text{SnO}_2/\text{GNRs}$  hybrid electrode showed good power performance with a reversible capacity of  $\sim 580 \text{mAhg}^{-1}$  at a current density of  $2 \text{Ag}^{-1}$  [Fig. 13]. Ravikumar et al.<sup>271</sup> synthesized GNS/ $\text{SnO}_2$  hybrid electrode materials. With this method, N-methylpyrrolidone was used as a solvent to exfoliate graphene, which was further treated with  $\text{SnCl}_2 \cdot 2\text{H}_2\text{O}$  and CTAB in the presence of  $\text{NH}_4\text{OH}$  to produce a sandwiched type GNS- $\text{SnO}_2$  hybrid material. The  $\text{SnO}_2/\text{GNS}$  hybrid electrode delivered a capacity of  $\sim 1009.8 \text{mAhg}^{-1}$  at a current density of  $100 \text{mA}^{-1}$  after 10 cycles and retained 57% of the initial capacity, whereas at a high current density of  $300 \text{mA}^{-1}$ , it retained 81% of the initial capacity ( $305.8 \text{mAhg}^{-1}$ ).  $\text{SnO}_2/\text{graphene}$  hybrids were synthesized using a ball milling process with a mechanochemical reaction between GO and Sn particles.<sup>272</sup> The  $\text{SnO}_2$  nanocrystal/graphene composites were synthesized with different grinding times and various raw materials ratios of Sn:GO. The experimental observations revealed that

$\text{SnO}_2/\text{graphene}$  composite with a grinding time of 8 h and raw material ratio of 1:1 formed  $\mu\text{m}$  sized architected chips composed of composites sheets and exhibited a high tap density of  $1.53 \text{gcm}^{-3}$ . When used as the anode material for LIBs, the specific capacity of  $\sim 891 \text{mAhg}^{-1}$  at a current density of  $100 \text{mA}^{-1}$  was achieved even after 50 cycles, with a Coulombic efficiency of  $\sim 94\%$ . In addition, the capacities of 1017  $\text{mAhg}^{-1}$  (3rd cycle), 817  $\text{mAhg}^{-1}$  (8th cycle), 709  $\text{mAhg}^{-1}$  (13th cycle), and 566  $\text{mAhg}^{-1}$  (18th cycle) were delivered at a current density of  $100 \text{mA}^{-1}$ ,  $200 \text{mA}^{-1}$ ,  $500 \text{mA}^{-1}$ , and  $1000 \text{mA}^{-1}$ , respectively.<sup>272</sup> Xu et al.<sup>273</sup> synthesized a nitrogen doped graphene/ $\text{SnO}_2$  hybrid material using a direct hydrothermal method. Using this method, stannic chloride hydrate was dissolved in the aqueous solution of GO, then urea, and concentrated HCl were added. The as prepared solution was hydrothermally treated at  $120^\circ\text{C}$  for 24 h. The size/shape and morphological studies performed through the TEM showed that the  $\text{SnO}_2$  nanorods with sizes of 10-15 nm in length and 2.5-4.0 nm in diameter were uniformly and monodispersed on the surface of graphene. This hybrid electrode could deliver reversible discharge capacities of 803.1  $\text{mAhg}^{-1}$  and 773.5  $\text{mAhg}^{-1}$  after 100 cycles at current densities of  $100 \text{mA}^{-1}$  and  $200 \text{mA}^{-1}$ , respectively. Furthermore, at a high current density 400  $\text{mA}^{-1}$ , stable reversible capacity of 642  $\text{mAhg}^{-1}$  and Coulombic efficiency of  $\sim 99.2\%$  were achieved at the 80<sup>th</sup> cycle. Remarkably, the Coulombic efficiency was increased with increasing current density from 96.1% (at  $50 \text{mA}^{-1}$ ) to 97.2% (at  $100 \text{mA}^{-1}$ ), then to 98.5% (at  $200 \text{mA}^{-1}$ ), and then to 99.2% (at  $400 \text{mA}^{-1}$ ). The high capacity and good stability of the RGO/ $\text{SnO}_2$  hybrid electrode was attributed to the intimate contact between the RGO platelets and  $\text{SnO}_2$  nanoparticles, and to the enhanced electrical conductivity of the hybrid due to N-doping.<sup>274-276</sup>

The synthesis of the carbon-coated  $\text{SnO}_2/\text{graphene}$  hybrid through a hydrothermal method assisted by a post calcination treatment has been reported by Zhang et al.<sup>277</sup> The HR-TEM micrographs further suggest that, in addition to the crumpled GNS and  $\text{SnO}_2$  nanoparticles ( $\sim 5$  nm in diameter), thin layers of carbon were developed on the edges of the  $\text{SnO}_2$  nanoparticles. The thin carbon layer was not only in contact with the GNS, but also covered the  $\text{SnO}_2$  nanoparticles. Therefore, the  $\text{SnO}_2$  nanoparticles were wrapped between the amorphous carbon coating layers and GNS. The combined effect of graphene layer and carbon coating can effectively maintain the stability and significantly prevent the detachment of  $\text{SnO}_2$  nanoparticles, thus affording better electrochemical properties than those of the pristine  $\text{SnO}_2$  electrode. When used as an anode in LIBs, this hybrid exhibited a capacity of  $\sim 757 \text{mAhg}^{-1}$  at a current density of  $200 \text{mA}^{-1}$ , even after 150 cycles. Meanwhile, the corresponding Coulombic efficiency was observed to be nearly 100%. In addition, it showed better capacity retention than the  $\text{SnO}_2/\text{carbon}$  and  $\text{SnO}_2/\text{graphene}$  hybrid electrodes.<sup>277</sup> It was noticed that the introduction of carbon shell restricts the undesirable reactions, whereas a porous structure can improve the diffusion of liquid electrolyte into the bulk materials.<sup>278,279</sup> Zhang et al.<sup>280</sup> fabricated  $\text{SnO}_2/\text{graphene}/\text{CNT}$  hybrid based flexible paper. Using the synthesis method, GO and CNTs were mixed to obtain a homogeneous GO/CNT solution. Subsequently,  $\text{SnCl}_4 \cdot 5\text{H}_2\text{O}$  was mixed in this solution and the supernate obtained through the centrifugation process was then passed through a membrane filter to produce a flexible paper. This paper was further calcined in an  $\text{N}_2$  atmosphere at  $450^\circ\text{C}$  for 2h to reduce the GO in graphene. In this hybrid,  $\text{SnO}_2$  nanoparticles (3-5 nm) were attached onto the surface of GNS (anchored with surface functional groups) and were encapsulated in pore channels formed by entangled GNS. It was perceived that the 3D conductive network and the presence of CNTs reduce the charge transfer resistance; therefore, the  $\text{SnO}_2/\text{graphene}/\text{CNT}$  hybrid electrode exhibited better

electrochemical performance than the SnO<sub>2</sub>/graphene hybrid, SnO<sub>2</sub>, and bare graphene anode. The SnO<sub>2</sub>/graphene/CNT hybrid electrode delivered capacities of 635 mAhg<sup>-1</sup> and 345 mAhg<sup>-1</sup> at current densities of 0.25 and 1.5 Ag<sup>-1</sup>, respectively. In addition, it showed a stable capacity of 387 mAhg<sup>-1</sup> at a current density of 0.1 Ag<sup>-1</sup> after 50 cycles.<sup>280,281</sup>

It has been reported that the sulphur-coated SnO<sub>2</sub> further improves the performance of the SnO<sub>2</sub>/graphene hybrid electrode. The electrochemical performance revealed that compared to the SnO<sub>2</sub>/graphene hybrid, the sulphur-coated SnO<sub>2</sub>/graphene hybrid electrode exhibited a better response, which was attributed to the buffering effects of sulphur.<sup>282,283</sup> Liu et al.<sup>284</sup> fabricated flexible graphene film, decorated with spindle type Fe<sub>2</sub>O<sub>3</sub>@SnO<sub>2</sub> nanoparticles. Using the synthesis approach, FeOOH@SnO<sub>2</sub> nanospindles were synthesized using the hydrothermal method and FeOOH@SnO<sub>2</sub>/GO film was then prepared through a vacuum filtration technique (using a solution of FeOOH@SnO<sub>2</sub>/GO) and changed to hybrid Fe<sub>2</sub>O<sub>3</sub>@SnO<sub>2</sub>/GS films when annealed at 500 °C in Ar atmosphere. It was observed that the Fe<sub>2</sub>O<sub>3</sub>@SnO<sub>2</sub>/GS films behave as a binder free electrode and exhibit a reversible discharge capacity of 1015 mAhg<sup>-1</sup> at a current density of 100 mA g<sup>-1</sup> even after 200 cycles. Notably, a charge/discharge efficiency of ~ 100% was maintained during the 100 cycles with a specific capacity of > 700 mAhg<sup>-1</sup> at a current density of 400 mA g<sup>-1</sup>. Furthermore, the Fe<sub>2</sub>O<sub>3</sub>@SnO<sub>2</sub>/GS hybrid film also showed much better electrochemical performance compared to the Fe<sub>2</sub>O<sub>3</sub>/GS and SnO<sub>2</sub>/GS hybrid electrodes.<sup>284</sup> This phenomena was attributed to the uniform dispersion of Fe<sub>2</sub>O<sub>3</sub> around the SnO<sub>2</sub> nanoparticles, which also contributed to suppress the aggregation of the SnO<sub>2</sub> nanoparticles, therefore improving the electrochemical performance of the Fe<sub>2</sub>O<sub>3</sub>@SnO<sub>2</sub>/GS hybrids electrode.<sup>285</sup> Electrochemical investigations suggested that a synergetic effect not only occurred between the graphene and metal-oxide nanoparticles, but also between the SnO<sub>2</sub> and Fe<sub>3</sub>O<sub>4</sub> nanoparticles. In the same way, the SnO<sub>2</sub>/In<sub>2</sub>O<sub>3</sub>/GNS,<sup>286</sup> ZnO/SnO<sub>2</sub>/graphene,<sup>287</sup> and SnO<sub>2</sub>/Sn/RGO hybrid<sup>288</sup> electrodes exhibited better electrochemical performance than their single metal oxide NPs hybridized with graphene as summarized in Table 2].

#### 6.4 Cobalt oxide/graphene hybrid

Cobalt oxides are well known as potential alternative anode materials because of their promising high theoretical capacities (Co<sub>3</sub>O<sub>4</sub> ~ 890 mAhg<sup>-1</sup> & CoO ~ 715 mAhg<sup>-1</sup>), low cost, and eco-friendliness. However, these materials have issues such as a large volume variation and poor electronic conductivity during the cycling process. To circumvent these issues, graphene has been used as the template and the electrochemical performance of cobalt oxide nanomaterial was greatly improved in the hybrid form. Several studies on Co<sub>3</sub>O<sub>4</sub>/graphene<sup>289-302</sup> and CoO/graphene<sup>303-305</sup> hybrid electrode materials for LIB have been reported. Zhu et al.<sup>291</sup> synthesized cobalt-oxide/graphene hybrid via hydrothermal method assisted by thermal pyrolysis at different temperatures. In this hybrid, cobalt-oxide nanowall arrays were grown on RGO sheets. It was observed that the porosity of cobalt-oxide/RGO hybrids and the grain size of Co<sub>3</sub>O<sub>4</sub> nanoparticles affect the electrochemical performance of these hybrids, which can be tailored by varying the annealing temperature. The Co<sub>3</sub>O<sub>4</sub>/RGO hybrid exhibited an optimized specific capacity of ~ 673 mAhg<sup>-1</sup> after 100 cycles at a current density of 180 mA g<sup>-1</sup> (0.2 C). On the other hand the CoO/RGO hybrid delivered the specific capacity of 732 mAhg<sup>-1</sup> at a discharge current density of 150 mA g<sup>-1</sup> (0.2 C) after 100 cycles.<sup>291</sup> Li et al.<sup>292</sup> fabricated mesoporous Co<sub>3</sub>O<sub>4</sub> with a controlled nanostructure, directly grown on graphene membrane by

hydrothermal reaction assisted by annealing process. This Co<sub>3</sub>O<sub>4</sub> nanowall@graphene hybrid membrane anode delivered a reversible capacity of ~ 800 mAhg<sup>-1</sup> at a current density of 100mA g<sup>-1</sup>. Furthermore, it demonstrated good cyclic stability of > 600 mAhg<sup>-1</sup>, without fading the capacity and a Coulombic efficiency of nearly 100% over 500 cycles. The mesoporous structure and uniform distribution of Co<sub>3</sub>O<sub>4</sub> over the graphene can be favorable for better diffusion of Li<sup>+</sup> and strain buffer of Co<sub>3</sub>O<sub>4</sub> during the cycling process, rendering high performance for the electrodes.<sup>293-298</sup> The improved performance of the Co<sub>3</sub>O<sub>4</sub>/GNS hybrid was attributed to the buffering effects of GNS on the aggregation and volume change of Co<sub>3</sub>O<sub>4</sub> nanoparticles during the cycling processes, as well as the increased conductivity.<sup>289</sup> In addition, the size and shape of the Co<sub>3</sub>O<sub>4</sub> nanostructures can significantly affect the reversible capacity and cyclic stability. The Co<sub>3</sub>O<sub>4</sub> nanorod/GNS hybrids electrode exhibited a high reversible lithium storage capacity and much better rate capability compared to bare nanostructured Co<sub>3</sub>O<sub>4</sub>. The Co<sub>3</sub>O<sub>4</sub> nanorod/GNS hybrid anode exhibited capacities of ~ 1310 mAhg<sup>-1</sup> and ~ 1090 mAhg<sup>-1</sup> after 40 cycles at current densities of 100 mA g<sup>-1</sup> and 100 mA g<sup>-1</sup>, respectively. On the contrary, bare Co<sub>3</sub>O<sub>4</sub> and GNS electrode could only deliver a capacity of 85 mAhg<sup>-1</sup> and 252 mAhg<sup>-1</sup>, respectively, when measured at a current density of 100 mA g<sup>-1</sup> after 40 cycles. Moreover, after 40 cycles, when the current density was returned to the initial 100 mA g<sup>-1</sup>, this hybrid electrode recovered its original capacity or even a slightly higher capacity (reversible capacity was 1378 mAhg<sup>-1</sup> for the 45th cycle), suggesting good rate capability.<sup>302</sup>

Pan et al.<sup>306</sup> synthesized Co<sub>3</sub>O<sub>4</sub>/RGO hybrid electrode material using polyvinylpyrrolidone (PVP) as the surfactant under reflux conditions, assisted by post calcination treatment under a nitrogen atmosphere. The morphological investigation through FE-SEM/TEM micrographs revealed that when PVP was used during the synthesis, the loading of the Co<sub>3</sub>O<sub>4</sub> nanoparticles (~100 nm) over RGO was significantly enhanced with uniform distribution. Also, the Co<sub>3</sub>O<sub>4</sub> nanoparticles were tightly wrapped by RGO. This hybrid electrode exhibited a discharge capacity of 860 mAhg<sup>-1</sup> during 120 cycles at a current density of 40 mA g<sup>-1</sup>. The higher loading of the Co<sub>3</sub>O<sub>4</sub> nanoparticles over RGO influenced the electrochemical performance and the Co<sub>3</sub>O<sub>4</sub>/RGO hybrid synthesized using PVP exhibited an improved rate performance. Particularly, when the current density was increased to 1000 mA g<sup>-1</sup>, the specific capacity of ~ 400 mAhg<sup>-1</sup> was maintained. However, the capacities of the hybrid synthesized without using the PVP reduced dramatically and retained only 10% of the initial capacity at the same current rate. Hu et al.<sup>307</sup> synthesized a binder free Co<sub>3</sub>O<sub>4</sub>/graphene hybrid, directly deposited on Cu foil using an electrostatic spray technique. Fig. 14 shows a schematic diagram of the synthesis process. A synergistic effect from spraying and subsequent heat treatment led to the formation of porous and 3D cross-linked nanostructured Co<sub>3</sub>O<sub>4</sub>/graphene hybrid. This hybrid electrode delivered a capacity of ~ 631 mAhg<sup>-1</sup> at a current density of 1Ag<sup>-1</sup>, even after 58 cycles with a columbic efficiency of > 97%. Moreover, at a higher current density of 5 Ag<sup>-1</sup>, it retained a capacity of ~ 321 mAhg<sup>-1</sup> [Fig. 15]. The morphological compatibility, along with a strong interfacial interaction between the graphene and Co<sub>3</sub>O<sub>4</sub> nanoparticles, significantly stimulated the interfacial electron and Li<sup>+</sup> transport, therefore improving the performance of these hybrid electrodes compare to bare Co<sub>3</sub>O<sub>4</sub> electrodes.<sup>308-309</sup>

The synthesis of CoO/RGO hybrid by directly employing C<sub>4</sub>H<sub>6</sub>O<sub>4</sub>·Co·4H<sub>2</sub>O and hydrophilic GO as raw materials using *in-situ* chemical reduction assisted by post calcination treatment has been reported.<sup>303</sup> It was observed that dense and small-size CoO (~ 5 nm) nanoparticles, uniformly anchored onto the disordered RGO nanosheets provide an interfacial interaction between CoO

nanoparticles and RGO nanosheets. This strong interfacial interaction efficiently improved the reversible capacity, rate capability, and cycle life of these hybrids.<sup>303</sup> The CoO/RGO hybrid electrode could deliver a reversible capacity of  $\sim 701.7 \text{ mAhg}^{-1}$  at a current density of  $100 \text{ mAg}^{-1}$  after 50 cycles. Furthermore, at even over 435 cycles after cycled at different current rates from 100 to  $4000 \text{ mAg}^{-1}$ , the specific capacity of  $\sim 577.9 \text{ mAhg}^{-1}$  was retained when the current density was returned to  $100 \text{ mAg}^{-1}$ . In contrast, the bare CoO nanoparticles electrode could deliver the specific capacity of  $\sim 463.2 \text{ mAhg}^{-1}$  at a current density of  $100 \text{ mAg}^{-1}$  after 50 cycles. Peng et al.<sup>304</sup> synthesized a CoO quantum dot/GNS hybrid using a facile ultrasonic method. With this method, GNS was mixed in hexane through ultra-sonication, and  $\text{Co}_4(\text{CO})_{12}$  was then directly added and mixed under sonication. The obtained products were then collected via centrifugation and dried at  $60^\circ\text{C}$  in air to yield the amorphous CoO quantum dot (QDs)/GNS hybrid. In order to increase the crystallinity, it was calcined at  $550^\circ\text{C}$  under an  $\text{N}_2$  atmosphere. The morphological investigations revealed that in this hybrid, CoO QDs ( $\sim 5 \text{ nm}$ ) were uniformly dispersed on the surface of GNS. It has been reported that such a hybrid structure could be an ideal candidate for high lithium storage due to several unique characteristics. First, the very small size of CoO QD with high mass loading can provide very large electrochemical active sites, which was mainly responsible for the high capacity. Second, the firm anchoring of the CoO QDs on GNS could significantly restrict the aggregation and volume change of the particles during the cycling process, therefore providing high reversibility and cycling stability. Furthermore, the isolated CoO QDs on the highly conductive GNS support provides each CoO QD not only the required conductivity, but also a short diffusion length for  $\text{Li}^+$ .<sup>310-312</sup> The CoO quantum-dot/graphene hybrid electrode exhibited a high reversible storage capacity of  $1592 \text{ mAhg}^{-1}$  at a current density of  $50 \text{ mAg}^{-1}$  after 50 cycles, along with a high Coulombic efficiency of over 95%. In addition, it exhibited high rate capability (capacity of  $\sim 1008 \text{ mAhg}^{-1}$  with a retention of  $\sim 77.6\%$  after 50 cycles, measured at a current density of  $1000 \text{ mAg}^{-1}$ ), which was dramatically increased from the capacity at  $50 \text{ mAg}^{-1}$  after 10 cycles).<sup>304</sup>

3D-RGO hydrogels anchored with CoO nanoparticles were prepared using hydrothermal method and a subsequent heat-treatment process.<sup>313</sup> In the 3D-RGO hydrogel/CoO hybrid, CoO nanoparticles ( $\sim 10 \text{ nm}$ ) were encapsulated within graphene-based hydrogel with robust interconnected networks. This hybrid electrode could deliver capacities of 457.0, 543.8, 690.4, and  $890.2 \text{ mAhg}^{-1}$  at current densities of 2400, 1600, 800, and  $200 \text{ mAg}^{-1}$ , respectively. Additionally, the specific capacity was increased up to  $1025.8 \text{ mAhg}^{-1}$  after 82 cycles, when the current density returned to  $100 \text{ mAg}^{-1}$ , which suggests good rate capability and cyclic stability. Qi et al.<sup>314</sup> synthesized highly CoO nanoparticles loaded CoO/graphene hybrids using a self-assembly approach via an oil-phase solution synthesis technique. This method involved the thermal decomposition of Co-acetylacetonate by oleylamine (OAm) in the presence of graphene, where Co nanoparticles of  $\sim 15 \text{ nm}$  were uniformly distributed onto GNS because of the complete miscibility between graphene and OAm. The CoO/graphene hybrids with different mass ratios (CoO/graphene) of 9 : 1, 7 : 3, and 4 : 6 exhibited reversible capacities of 1401, 937, and  $669 \text{ mAhg}^{-1}$ , respectively, and were found to be much better than bare graphene ( $421 \text{ mAhg}^{-1}$ ) at a current density of  $100 \text{ mAg}^{-1}$ . In addition, at a high current density of  $8.0 \text{ Ag}^{-1}$ , this hybrid electrode was capable of delivering a stable capacity of  $\sim 500 \text{ mAhg}^{-1}$  after 35 cycles. Nevertheless, when the current density was decreased from  $8.0$  to  $0.25 \text{ Ag}^{-1}$ , about 83% of the initial capacity obtained at  $0.25 \text{ Ag}^{-1}$  ( $\sim 950 \text{ mAhg}^{-1}$ ) could be recovered.<sup>314</sup> The superior electrochemical performance of the CoO/graphene hybrids electrode was attributed

to structural stability and inhibited electrode pulverization during the cycling processes.<sup>315</sup> Zhang et al.<sup>316</sup> synthesized flexible mats composed of CoO, graphene, and carbon nanofibers by electrospinning and a subsequent thermal treatment. This CoO/graphene/carbon hybrid electrode exhibited discharge capacities of 760 (after 252 cycles) and  $690 \text{ mAhg}^{-1}$  (after 352 cycles), respectively, at a current density of  $500 \text{ mAg}^{-1}$ . These storage capacities were found to be much higher than those of graphene/carbon, CoO/carbon nanofibers, and pure carbon electrodes at the respective cycles. In addition, after cycling at various current rates from  $0.1 \text{ Ag}^{-1}$  to  $2 \text{ Ag}^{-1}$  when the current density was returned to  $0.1 \text{ Ag}^{-1}$  (after 30 cycles), this hybrid could deliver relatively higher capacity ( $\sim 800 \text{ mAhg}^{-1}$ ), signifying good rate capability. The improved electrochemical performance was ascribed to a number of factors, including fast diffusion of  $\text{Li}^+$  due to the presence of carbon nanofiber, whereas enhanced electrical conductivity and mechanical properties were offered by graphene.<sup>316</sup>

## 6.5 Manganese oxide/graphene hybrid

Manganese oxide ( $\text{MnO}_2$ ) is an attractive anode material (theoretical capacity of  $\sim 1232 \text{ mAhg}^{-1}$ ) that has been widely used for LIBs. It possesses unique properties, including high energy density, low conversion potential ( $< 0.8 \text{ V}$ ), low electrochemical motivation force ( $1.032 \text{ V vs. Li/Li}^+$ ), high abundance, low cost, and environmental friendliness. Unfortunately, the practical application is mainly hampered by poor electrical conductivity and large volume expansion during the charge/discharge process. Nanostructured  $\text{MnO}_2$ , hybridized with graphene, has shown an effective approach to accommodate the strain of volume change with improved electrical conductivity.<sup>317-321</sup> The electrochemical performances can significantly be improved in the hybrid state. Li et al.<sup>320</sup> synthesized  $\text{MnO}_2$  nanoplatelet/graphene hybrid material using a chemical method. It was suggested that the unique porous structure of the hybrid could facilitate rapid transport of electrons and electrolyte ions throughout the hybrid material. Therefore, this hybrid electrode exhibited a much higher capacity of  $905 \text{ mAhg}^{-1}$  compared to pure  $\text{MnO}_2$  ( $416 \text{ mAhg}^{-1}$  at a current density of  $50 \text{ mAg}^{-1}$ ). Furthermore, this hybrid electrode exhibited an irreversible capacity loss of  $\sim 36\%$  in comparison with 55% for the bare  $\text{MnO}_2$  electrode. In addition, the hybrid electrode exhibited much better rate capability compared to bare GNS and  $\text{MnO}_2$  electrodes at different rates. Notably, a reversible capacity of  $\sim 341 \text{ mAhg}^{-1}$  was achieved at the current density of  $500 \text{ mAg}^{-1}$ , and a stable capacity of  $\sim 630 \text{ mAhg}^{-1}$  could be retained when the current rate was backed to  $50 \text{ mAg}^{-1}$ .<sup>320</sup> Radich et al.<sup>322</sup> reported that RGO assists in the expulsion of ions from the  $\text{MnO}_2$  lattice and also enhances the crystallinity. Moreover, it was able to repair the impure phases within the  $\text{MnO}_2$ .<sup>322-323</sup> Recently, Li et al.<sup>324</sup> reported  $\text{MnO}_2/3\text{D porous graphene (3D PG-Mn)}$  hybrid, synthesized through a self-controlled redox deposition process. The 3D porous network of graphene [Fig. 16] offers a highly conductive structure and a large surface area which intensify the contact between  $\text{MnO}_2$  nanoparticles and increases the mechanical strength of the 3D PG-Mn hybrid during the cycling process. Therefore, 3D PG-Mn hybrid exhibited an electrochemical performance superior to the bare  $\text{MnO}_2$  nanoparticles electrode. Furthermore, it was observed that 3D PG-Mn hybrid electrode with 62.7 wt% of  $\text{MnO}_2$  exhibited a stable capacity of  $\sim 836 \text{ mAhg}^{-1}$  at a current density of  $100 \text{ mAg}^{-1}$  after 200 cycles ( $\sim 84.6\%$  capacity retention). Moreover, after cycling at different current rates ( $100 \text{ mAg}^{-1}$  to  $1600 \text{ mAg}^{-1}$ ), when the current was reduced to  $100 \text{ mAg}^{-1}$ , the discharge capacity of  $\sim 869 \text{ mAhg}^{-1}$  could be achieved after 45 cycles (compared to  $\sim 926 \text{ mAhg}^{-1}$  after 10 cycles), suggesting good rate capability [Fig. 17].

Wang et al.<sup>325</sup> synthesized Mn<sub>3</sub>O<sub>4</sub>/graphene hybrid using a hydrothermal method. The SEM/TEM studies revealed that Mn<sub>3</sub>O<sub>4</sub> nanoparticles with a size of ~10-20 nm were grown on RGO sheets. The intimate interaction between Mn<sub>3</sub>O<sub>4</sub> nanoparticles and RGO causes a synergetic effect. Therefore, the Mn<sub>3</sub>O<sub>4</sub>/RGO hybrid electrode could afford a capacity of ~ 900 mAhg<sup>-1</sup> at a current density of 40 mA g<sup>-1</sup>. In addition, after cycling at different current rates, a capacity of ~730 mAhg<sup>-1</sup> (after 40 cycles) at 400 mA g<sup>-1</sup> was retained compared to ~780 mAhg<sup>-1</sup> (after 15 cycles), suggesting good rate capability. In contrast, bare Mn<sub>3</sub>O<sub>4</sub> electrode could deliver a capacity below 300 mAhg<sup>-1</sup>, which was further decreased to ~ 115 mAhg<sup>-1</sup> (at 40 mA g<sup>-1</sup>) after only 10 cycles.<sup>325-326</sup> Lavoie et al.<sup>327</sup> studied the electrochemical performance of Mn<sub>3</sub>O<sub>4</sub>/graphene hybrids for LIB. In the process of electrode preparation they used two different types of binders: carboxymethyl cellulose and PVDF. On the basis of experimental results, they claimed that lithium carboxymethyl cellulose (LICMC) could be a better binder than the conventional PVDF, due to its easy processability in water. Furthermore, when LICMC was used as the binder, the hybrid electrode exhibited much better capacity than that of PVDF. At a current density 75 mA g<sup>-1</sup>, the capacities of ~ 720 mAhg<sup>-1</sup> (using LICMC) and ~ 365 mAhg<sup>-1</sup> (using PVDF) were obtained after 100 cycles. This superior capacity retention was attributed to the formation of bonds between the hydroxyl groups present at the surface of the nanoparticles and carboxyl groups of the binder, which resulted in an enhanced interface interaction with the active materials.<sup>327</sup> Recently, Park et al.<sup>328</sup> synthesized an N-doped Mn<sub>3</sub>O<sub>4</sub>/graphene hybrid material using hydrothermal method with hydrazine as a reducing agent and nitrogen source both. N-doping can allow fast electron/ion transfer by decreasing the energy barrier, whereas uniform dispersion of the Mn<sub>3</sub>O<sub>4</sub> nanoparticle graphene significantly enhances the electro-active surface area.<sup>329-331</sup> Therefore, the N-doped Mn<sub>3</sub>O<sub>4</sub>/graphene hybrid electrode exhibited superior capacity and good rate capability. The electrochemical results suggest that without doping of nitrogen, the Mn<sub>3</sub>O<sub>4</sub>/graphene electrode exhibited a capacity of ~ 703 mAhg<sup>-1</sup> at a current density of 200 mA g<sup>-1</sup>, after 40 cycles. In contrast, the nitrogen doped Mn<sub>3</sub>O<sub>4</sub>/graphene (N-Mn<sub>3</sub>O<sub>4</sub>/graphene) electrode exhibited a specific capacity of 800 mAhg<sup>-1</sup> under the same conditions. Additionally, the N-Mn<sub>3</sub>O<sub>4</sub>/graphene hybrid electrode showed a rate capability superior to bare Mn<sub>3</sub>O<sub>4</sub>, graphene and the Mn<sub>3</sub>O<sub>4</sub>/graphene hybrid electrode. When cycled at various current rate (100 mA g<sup>-1</sup> to 2 Ag<sup>-1</sup>), the N-Mn<sub>3</sub>O<sub>4</sub>/graphene hybrid electrode could deliver a capacity of ~ 400 mAhg<sup>-1</sup> at 2.0 Ag<sup>-1</sup> after 25 cycles.

Mai et al.<sup>332</sup> synthesized MnO/RGO hybrid via liquid phase deposition of MnCO<sub>3</sub> nanoparticles over the surface of GNS and subsequent heat treatment in a nitrogen environment. In this hybrid, the surfaces of RGO sheets which were comprised of 35 layers, were homogeneously covered with several MnO nanoparticles having a size ~ 10 nm. After 50 cycles, a reversible capacity of 665.5 mAhg<sup>-1</sup> was observed at a current density of 100 mA g<sup>-1</sup> in the case of the MnO/RGO hybrid electrode. On the other hand, the bare MnO electrode showed a continuous decay in reversible capacity as the cyclic number was increased, and after 20 cycles it levelled off with a capacity of ~ 260 mAhg<sup>-1</sup>. Furthermore, upon increasing the current density to 400 and 800 mA g<sup>-1</sup>, the hybrid electrode could maintain a capacity of ~ 454.2 and ~ 325.6 mAhg<sup>-1</sup>, respectively. Also, the MnO/RGO hybrid electrode could regain higher specific capacity and better cyclic stability than the bare MnO electrode by reverting to a lower current density of 200 mA g<sup>-1</sup> even after 40 cycles.<sup>332</sup>

Lithium intercalation behaviors in manganese oxides/graphene hybrid have been investigated by Sun et al.<sup>333</sup> The electrochemical

observation showed that a change of the oxidation state of Mn (II) to Mn (IV) and the interfacial lithium storage during the cycling process can enhance the specific capacity.<sup>333-334</sup> The electrochemical studies revealed that the valence state of manganese oxide significantly influences the lithium storage capacity of the manganese-oxide/graphene hybrid material.<sup>335-340</sup> Cheekati et al.<sup>335</sup> reported that the MnO/graphene hybrid electrode has better storage and cycling stability than the Mn<sub>3</sub>O<sub>4</sub>/graphene hybrid electrode. Lee et al.<sup>341</sup> synthesized graphene-MnO hybrid via spray pyrolysis method using the colloidal solution of GO and manganese nitrate hexahydrate. Morphological studies through SEM/TEM micrographs revealed that the MnO/graphene hybrid possessed a crumpled structure (size ~1 μm), where the MnO nanoparticles (several tens of nm) were uniformly distributed over the graphene sheets. In contrast, bare MnO showed a hollow structure with a size of several μm. This graphene-MnO hybrid electrode exhibited initial charge and discharge capacities of 849 and 1207 mAhg<sup>-1</sup>, respectively, at a current density of 500 mA g<sup>-1</sup>. In contrast, the hollow-structured MnO electrode exhibited charge and discharge capacities of 673 and 1004 mAhg<sup>-1</sup>, respectively. Further, the hollow-structured MnO and graphene/MnO hybrid electrode could deliver discharge capacities of ~ 701 and 1313 mAhg<sup>-1</sup>, respectively, after 130 cycles. The MnO/graphene hybrid also exhibited a rate capability superior to bare MnO electrode. Such a superior electrochemical performance was attributed to the very small size of MnO nanoparticles, high specific surface area, small charge transfer resistance, and high lithium diffusion coefficient in the MnO/graphene hybrid.

### 6.6 Nickel oxide/ graphene hybrid

Because of the low cost, high safety, and ecofriendly features, NiO is considered to be a promising anode material. NiO exhibits a theoretical capacity of 718 mAhg<sup>-1</sup>, but it suffers problems associated with poor conductivity and cycling stability. To overcome these obstacles, strategies have been employed to fabricate NiO/graphene hybrid materials. Kottegoda et al.<sup>342</sup> synthesized graphene/NiO hybrid via a controlled hydrothermal reaction method. Using this method, an appropriate amount of GO and metal salt was dispersed in ethylene glycol and then hydrothermally treated at 160 °C for 16 h. Subsequently, pyrolysis was carried out through post annealing at 500 °C. The FE-SEM studies revealed that this hybrid consisted of NiO nanoparticles (size around few nm), firmly attached to certain sites on graphene sheets. However, following the same synthesis route, a completely different structural growth was observed in the pristine NiO, which shows a much larger particle size (100–300 nm) than in the NiO/graphene hybrid. This hybrid electrode with an optimized concentration of NiO (wt % = 50%), exhibited a capacity as high as 450 mAhg<sup>-1</sup> at 1C (1 C = 300 mA g<sup>-1</sup>) after 100 cycles. Nevertheless, this electrode could deliver good capacities of ~ 450 mAhg<sup>-1</sup> and ~ 400 mAhg<sup>-1</sup> at current rates of 1 C and 2 C, respectively. In contrast, the hybrid electrode with NiO (wt % = 20%) showed a relatively higher capacity at higher current rates of 10 C and 20 C. NiO nanosheets (NS), grown on GNS, were synthesized using hydrothermal method.<sup>343</sup> The combined experimental and theoretical investigations suggested the formation of an oxygen bridge between the NiO nanosheet and graphene. It was concluded that the oxygen bridge between graphene and NiO NS contributes to good conductivity and causes a synergistic effect, thus improving the lithium storage properties. The NiO NS/graphene hybrid electrode exhibited a stable reversible capacity of ~ 883 mAhg<sup>-1</sup> at a current density of 50 mA g<sup>-1</sup> after 50 cycles, and retained ~90% of the initial capacity. This reversible capacity was observed to be superior to that of the NiO NS/graphene mixture (530 mAhg<sup>-1</sup>,

retention of ~ 76%) and the bare NiO NSs (210 mAhg<sup>-1</sup> and retention of only 35%) electrode.

Hwang et al.<sup>334</sup> synthesized a NiO/graphene hybrid by chemical precipitation followed by post calcination treatment. This hybrid material consists of plate type nanostructured NiO (90 – 120 nm), homogeneously anchored on GNS. The plate type NiO nanostructures work as spacers and keep the neighbouring GNS separated, thus forming a 3D hybrid structure. The 3D conducting network of NiO/graphene affords a fast electron transfer between the current collector and the active material. Furthermore, NiO/graphene hybrid with a higher content of NiO (59 wt.%) exhibited better performance than the hybrid consisting of NiO (37 wt.%). After 40 cycles, the NiO/graphene (NiO, 59 wt. %), NiO/graphene (NiO, 37 wt. %) and bare graphene electrode could deliver discharge capacities of ~ 856, 604, and 302, mAhg<sup>-1</sup> at 5 C (5000 mA g<sup>-1</sup>), respectively.<sup>344</sup> In addition, Zhu et al.<sup>345</sup> studied the electrochemical performance of NiO/RGO hybrid. The morphological investigations revealed that in this hybrid, NiO particles consisted of nanosheet-based microsphere structures that were uniformly anchored on the surface of RGO platelets. The NiO/RGO hybrid electrode exhibited the initial discharge and charge capacities of 1641 mAhg<sup>-1</sup> and 1097 mAhg<sup>-1</sup> (at 100 mA g<sup>-1</sup>), respectively. Moreover, after 50 cycles, a charge capacity of ~ 727 mAhg<sup>-1</sup> (at 1600 mA g<sup>-1</sup>) and a discharge capacity of ~1041 mAhg<sup>-1</sup> (at 100 mA g<sup>-1</sup>) were achieved. In contrast, after 50 cycles (at 100 mA g<sup>-1</sup>), the bare NiO electrode could deliver only a discharge and charge capacity of 91 and 90 mAhg<sup>-1</sup>, respectively. The NiO/graphene hybrid synthesized using a liquid-phase deposition method was also reported.<sup>346</sup> In this hybrid, graphene was composed of 3–5 individual graphene layers and the size of the NiO nanoparticles were ~ 5 nm. Fig. 18 shows that after 35 cycles at a current density of 100 mA g<sup>-1</sup>, this NiO/graphene hybrid electrode was able to deliver a capacity of 646.1 mAhg<sup>-1</sup>, with a retention value of ~ 86.3 %. Moreover, capacities of 509 mAhg<sup>-1</sup> and 368.5 mAhg<sup>-1</sup> were obtained at current densities of 400 and 800 mA g<sup>-1</sup>, respectively.<sup>346</sup> Recently, Zhu et al.<sup>347</sup> synthesized Ni(OH)<sub>2</sub>/RGO hybrid material using a co-precipitation method following a reduction using hydrazine. The Ni(OH)<sub>2</sub>/RGO hybrid electrode exhibited a reversible capacity of ~1003 mAhg<sup>-1</sup> at a current density of 100 mA g<sup>-1</sup> after 40 cycles. In contrast, the bare Ni(OH)<sub>2</sub> and RGO electrodes exhibited reversible capacities of ~ 160 mAhg<sup>-1</sup> and ~ 234 mAhg<sup>-1</sup>, respectively, under the same conditions. Furthermore, the performance of the Ni(OH)<sub>2</sub>/RGO hybrid electrode was observed to be even better than that of the β-Ni(OH)<sub>2</sub>@RGO hybrid electrode.<sup>348</sup>

### 6.7 Copper oxide/graphene hybrid

Although copper oxides are attractive anode materials and exhibit theoretical capacities of 674 mAhg<sup>-1</sup> (CuO) and 374 mAhg<sup>-1</sup> (Cu<sub>2</sub>O), similar to other metal oxides, it also suffers from problems related to rapid fading of the capacity due to large volume expansion and contraction during the cycling process.<sup>349-350</sup> Several studies have demonstrated that the combination of CuO/Cu<sub>2</sub>O and graphene can display some unique properties that are useful for practical application in LIB. CuO/RGO hybrid was synthesized using a pex-milled process by mixing CuO nanoparticles with GNS. The initial charge density (1043.3 mAhg<sup>-1</sup>) of the CuO/RGO hybrid electrode was found to be significantly higher than that of pure CuO nanoparticles (785.2 mAhg<sup>-1</sup> at 0.1 mAcm<sup>-2</sup>). Furthermore, after 45 cycles, the reversible capacity was maintained at ~ 516.4 mAhg<sup>-1</sup> in the case of the CuO/RGO hybrid electrode at a current density of 0.1 mAcm<sup>-2</sup> with a columbic efficiency of ~ 90%.<sup>351</sup> It was observed that tight contact between the graphene and CuO nanoparticles forms a highly conductive network, and the issues with the volume change during the cycling process therefore efficiently diminished in the

presence of the hollow CuO nanoparticles.<sup>352</sup> Zhou et al.<sup>353</sup> synthesized CuO a nano-leaves/graphene hybrid using a microwave-assisted method. The SEM/ TEM investigations showed that leaf-shaped CuOs (rhombic) were uniformly dispersed on GNS having a length of 100-140 nm and width of 40 nm. Compared to pristine CuO, the CuO/GNS hybrids electrode exhibited superior electrochemical performance. The electrochemical result showed that after 50 cycles at a current density of 100 mA g<sup>-1</sup>, the CuO/GNS hybrids electrode retained a capacity of ~ 600 mAhg<sup>-1</sup>. Also, even when cycled (during 50 cycles) at different rates, a capacity of ~ 600 mAhg<sup>-1</sup> was recovered, suggesting good rate capability.<sup>353</sup> Furthermore, parameters such as capacity, rate capability, cycling stability, and Coulombic efficiency can be controlled by tailoring the morphology of the CuO/graphene hybrids and structural features (shape/size) of CuO.<sup>354-356</sup> It was proposed that compared to granules and slab-like morphology, the CuO nanoparticles with hierarchical structures afford a larger surface area. Therefore, they offer a better contact area between the electrode and electrolyte and enhance the reactivity of the electrode.<sup>357-359</sup> Liu et al.<sup>360</sup> synthesized flexible and free-standing CuO nanosheets/RGO hybrid lamellar paper via vacuum filtration and hydrothermal assisted reduction processes. This hybrid lamellar paper exhibited a 3-D nanoporous network, where sheets type nanostructured CuOs were homogeneously embedded within RGO layers. The CuO nanosheets/RGO hybrid electrode exhibited much better specific capacity (736.8 mAhg<sup>-1</sup> after 50 cycles at 0.1 C) than the pristine CuO nanosheet (219.1 mAhg<sup>-1</sup> after 50 cycles at 0.1 C) and RGO electrode (67 mA g<sup>-1</sup> after 50 cycles at 0.1 C).<sup>360</sup>

Recently, Li et al.<sup>361</sup> fabricated core-shell Cu<sub>2</sub>O@Cu/graphene hybrids using a microwave-assisted synthesis approach. The unique dual-conducting system consisting of graphene support and a coating of a Cu layer on the surface of Cu<sub>2</sub>O nanoparticles significantly improved the electrochemical performance. The Cu<sub>2</sub>O@Cu/graphene hybrid electrode exhibited a specific capacity of ~ 775 mAhg<sup>-1</sup> at a current density of 50 mA g<sup>-1</sup>, which was higher than those of the Cu<sub>2</sub>O@Cu nanospheres (~ 100 mAhg<sup>-1</sup>) and the Cu<sub>2</sub>O-GS (416 mAhg<sup>-1</sup>) hybrid electrode. Moreover, the Cu<sub>2</sub>O@Cu/graphene electrode showed better rate capability than the Cu<sub>2</sub>O@Cu nanospheres and Cu<sub>2</sub>O/GS hybrid electrode. The Cu<sub>2</sub>O@Cu/graphene electrode could deliver the specific capacity of ~ 410 mAhg<sup>-1</sup> at 2000 mA g<sup>-1</sup>, and after cycling at different current rates, when returning to 50 mA g<sup>-1</sup> (after 50 cycles), it delivered a capacity of ~779 mAhg<sup>-1</sup>.<sup>361</sup> Zhang et al.<sup>362</sup> synthesized shape/size controlled Cu<sub>2</sub>O/GNS hierarchical nanohybrids using an ultrasound assisted approach with a mixed solution of copper acetate, glucose ethylene glycol, and GO. Fig. 19 shows TEM images of Cu<sub>2</sub>O/GNS and bare Cu<sub>2</sub>O spheres. This hierarchical Cu<sub>2</sub>O/GNS hybrid electrode exhibited the specific capacity of ~ 400 mAhg<sup>-1</sup> at a current density of 100 mA g<sup>-1</sup> after 20 cycles, which was much higher than that of bare Cu<sub>2</sub>O nanospheres (~ 100 mAhg<sup>-1</sup>) [Fig. 20]. Additionally, the Cu<sub>2</sub>O/GNS hybrid electrode could achieve a Coulombic efficiency of ~ 90%, during the entire cycling (100 cycles) process. It has been reported that the small size of Cu<sub>2</sub>O nanoparticles consisting of hollow structures can exhibit better electrochemical performances.<sup>363-364</sup>

### 6.8 Molybdenum oxides/graphene hybrid

Among the different types of transition metal oxides, MoO<sub>2</sub> possesses a layered-type structure and has been considered a promising anode material. It exhibits a theoretical specific capacity of ~ 838 mAhg<sup>-1</sup>. However, an intrinsic drawback of molybdenum oxides is volume expansion during the Li<sup>+</sup> insertion/extraction. It is known that the irreversible volume change causes these particles to pulverize and crack, which essentially detaches the active material

from the current collector and consequently leads to substantial reduction in capacity. Graphene has shown its potential to overcome the above mentioned problems by improving the electron kinetics. Sun et al.<sup>365</sup> synthesized hierarchical nanostructured MoO<sub>2</sub>/graphene. The electrochemical studies revealed that due to hierarchical topology this hybrid electrode displays high columbic efficiency and reversible capacity. After 60 cycles, a reversible capacity of 1009.9 mAhg<sup>-1</sup> was attained by the MoO<sub>2</sub>/graphene hybrid electrode at a current density of 100 mA g<sup>-1</sup> with a Coulombic efficiency of ~ 97.2 %. Furthermore, it was noticed that after the second cycle, the charge capacity was gradually increased from 468.7 mAhg<sup>-1</sup> to 1013.7 mAhg<sup>-1</sup> in the 50th cycle. This phenomenon was attributed to the activation process of the electrode material. During this process, MoO<sub>2</sub>/graphene hybrid may gradually lose its crystallinity and become amorphous, thus improving the Li<sup>+</sup> diffusion kinetics during charging/discharging.<sup>366</sup> The electronic conductivity of the MoO<sub>2</sub>/graphene hybrid was observed to be greater by eight orders of magnitude than the bare MoO<sub>2</sub>. The high electronic conductivity expedited charge transfer between the graphene and MoO<sub>2</sub> nanoparticles. Thus, an improved cycling stability (reversible capacity of ~ 550 mAhg<sup>-1</sup>) was retained after 1000 cycles and a capacity of ~ 770 mAhg<sup>-1</sup> was delivered at a current density of 540 mA g<sup>-1</sup>, even after 1000 cycles<sup>367</sup> [Fig. 21]. Furthermore, it has been reported that the presence of GO during the *in-situ* synthesis of MoO<sub>3</sub>/graphene hybrid can change the crystalline phase of the MoO<sub>3</sub> nanoparticles from orthorhombic to hexagonal.<sup>368-369</sup> In addition, the increased content of GO in the precursor solution changes the phase of the MoO<sub>3</sub> rods to MoO<sub>2</sub> nanorods and subsequently to MoO<sub>2</sub> nanoparticles. The MoO<sub>2</sub>/GO hybrid with 10 wt % GO could deliver a reversible capacity of ~ 720 mAhg<sup>-1</sup> at 100 mA g<sup>-1</sup> and 560 mAhg<sup>-1</sup> at a current density of 800 mA g<sup>-1</sup> after 30 cycles.<sup>370</sup> Also, the uniform dispersion of MoO<sub>2</sub> nanoparticles on graphene helps to improve the capacity and cycling stability.<sup>371</sup>

Noerochim et al.<sup>372</sup> synthesized a MoO<sub>3</sub> nanobelt/graphene hybrid via microwave-assisted hydrothermal method. With the synthesis method, an ultra-fast microwave-hydrothermal method was used to prepare GNS which was then mixed with MoO<sub>3</sub> solution. The morphological investigation revealed that this hybrid was composed of stacked GNS and uniform MoO<sub>3</sub> nanobelts having lengths of 5-10 μm and widths of around 200-500 nm. Furthermore, the MoO<sub>3</sub> nanobelt/graphene hybrid film displayed features of high flexibility and a binder-free electrode. Compared to the pristine MoO<sub>3</sub>, this hybrid electrode could deliver superior reversible capacity. After 100 cycles, the MoO<sub>3</sub>/graphene hybrid electrode delivered a discharge capacity of ~ 172 mAhg<sup>-1</sup> at 100 mA g<sup>-1</sup> with an initial Coulombic efficiency of ~ 98%. On the contrary, the discharge capacity for bare MoO<sub>3</sub> electrode was observed to be only 101 mAhg<sup>-1</sup> at 100 mA g<sup>-1</sup>, with an initial Coulombic efficiency of ~ 96%.<sup>372</sup> Choi et al.<sup>373</sup> synthesized a MoO<sub>2</sub>/graphene hybrid material using a spray pyrolysis method with a colloidal solution of GO in the presence of Mo ions. This crumpled MoO<sub>2</sub>/graphene hybrid was further transformed into a MoO<sub>3</sub>/graphene hybrid after post annealing treatment, and exhibited superior electrochemical behaviour compared to the bare MoO<sub>3</sub> nanoparticle. The MoO<sub>3</sub>/graphene hybrid electrode delivered a reversible discharge capacity of 845 mAhg<sup>-1</sup> at a current density of 3 Ag<sup>-1</sup>. The capacity retention for the graphene/MoO<sub>3</sub> hybrid electrode was ~ 87% after the first cycle, while that of bare MoO<sub>3</sub> electrode was observed to be only ~ 47% when measured after 100 cycles. Recently, graphene-encapsulated α-MoO<sub>3</sub> nanoribbons as a hybrid material have been synthesized using a self-assembly approach by exploiting the interaction of positively charged MoO<sub>3</sub> nanoribbons and negatively charged GO.<sup>374</sup> The hybrid structure of graphene-encapsulated MoO<sub>3</sub> nanoribbons not only exhibited high specific capacitance (~ 823

mAhg<sup>-1</sup> at 200 mA g<sup>-1</sup> after 70 cycles), but also superior cycling stability (>754 mAhg<sup>-1</sup> at 1000 mA g<sup>-1</sup> after 200 cycles) and enhanced rate capability (discharge capacity ~ 710 mAhg<sup>-1</sup> at 3000 mA g<sup>-1</sup> after 30 cycles). The improved electrochemical performances are attributed to the inhibited volume change/aggregation of MoO<sub>3</sub> nanobelts during the Li<sup>+</sup> insertion/extraction, enhanced electrical conductivity, high surface area, and short diffusion length for Li<sup>+</sup>, offered by graphene as the substrate.<sup>375-376</sup>

### 6.9 Lithium-titanate/graphene hybrid

Spinel Li<sub>4</sub>Ti<sub>5</sub>O<sub>12</sub> has attracted considerable attention as an anode material for LIBs because of the good reversibility of Li<sup>+</sup> intercalation and deintercalation and the nearly zero structural changes during the charging and discharging process. However, its low conductivity (10<sup>-9</sup> Scm<sup>-1</sup>) results in initial capacity loss and poor rate capability. The electrochemical performance of the Li<sub>4</sub>Ti<sub>5</sub>O<sub>12</sub>/graphene hybrid materials was significantly improved compared to bare Li<sub>4</sub>Ti<sub>5</sub>O<sub>12</sub>.<sup>377</sup> Kim et al.<sup>378</sup> synthesized Li<sub>4</sub>Ti<sub>5</sub>O<sub>12</sub> nanoplatelet/RGO hybrid via a two-step microwave-assisted solvothermal reaction and post calcination treatment. TEM study revealed that the Li<sub>4</sub>Ti<sub>5</sub>O<sub>12</sub> nanoplatelets (sizes of 10–20 nm) were well dispersed on RGO nanosheets. The Li<sub>4</sub>Ti<sub>5</sub>O<sub>12</sub> nanoplatelet/RGO hybrid electrode could deliver a discharge capacity of ~101 mAhg<sup>-1</sup> at a 100 C-rate. Moreover, it retained a capacity of ~ 95% at 1 C-rate and ~ 96% at 10 C-rate over 100 cycles. This improved performance was attributed to the short diffusion lengths of Li<sup>+</sup> through the Li<sub>4</sub>Ti<sub>5</sub>O<sub>12</sub> nanoplatelets, and its uniform dispersion over the highly conductive RGO. In the hybrid form, graphene not only reduces the resistance and polarization of the electrode effectively, but also balances the electrical conductivity and initial Coulombic efficiency.<sup>379</sup> The increased electrical conductivity and numerous electroactive sites of the hybrid electrode materials can improve the electrochemical properties.<sup>380-384</sup>

Guo et al.<sup>385</sup> synthesized Li<sub>4</sub>Ti<sub>5</sub>O<sub>12</sub>/graphene hybrid using an *in-situ* solid state reaction method. Using this method, Li<sub>4</sub>Ti<sub>5</sub>O<sub>12</sub> nanoparticles were first coated with carbon. The carbon coating not only confines the aggregation of the Li<sub>4</sub>Ti<sub>5</sub>O<sub>12</sub> particles, but also enhances the combination between graphene sheets and Li<sub>4</sub>Ti<sub>5</sub>O<sub>12</sub> particles. Therefore, even at 80 C (after 30 cycles), the carbon coated Li<sub>4</sub>Ti<sub>5</sub>O<sub>12</sub>/graphene (C-Li<sub>4</sub>Ti<sub>5</sub>O<sub>12</sub>/graphene) hybrid electrode could deliver a capacity of ~ 155 mAhg<sup>-1</sup>, which was twice that of the Li<sub>4</sub>Ti<sub>5</sub>O<sub>12</sub>/graphene hybrid electrode (70 mAhg<sup>-1</sup> at 80 C). In addition, these authors studied the temperature dependent electrochemical performance of C-Li<sub>4</sub>Ti<sub>5</sub>O<sub>12</sub>/graphene and Li<sub>4</sub>Ti<sub>5</sub>O<sub>12</sub>/graphene, which showed that even at a lower temperature, C-Li<sub>4</sub>Ti<sub>5</sub>O<sub>12</sub>/graphene hybrid exhibits better reversible capacities than Li<sub>4</sub>Ti<sub>5</sub>O<sub>12</sub>/graphene.<sup>385</sup> In the same way, compared to Li<sub>4</sub>Ti<sub>5</sub>O<sub>12</sub>/carbon hybrid, the Li<sub>4</sub>Ti<sub>5</sub>O<sub>12</sub>/graphene hybrid exhibited superior performance in terms of capacity and rate capability.<sup>386</sup> The electrochemical measurements have also shown that the presence of graphene in Li<sub>4</sub>Ti<sub>5</sub>O<sub>12</sub>/graphene hybrid (wrapping of graphene on individual Li<sub>4</sub>Ti<sub>5</sub>O<sub>12</sub> grains) offers better stability in Li<sub>4</sub>Ti<sub>5</sub>O<sub>12</sub> crystal and enhanced reversible Li<sup>+</sup> insertion/extraction even at high current rates, therefore improving the performance of the electrode material in the hybrid state.<sup>387-388</sup> Ri et al.<sup>389</sup> synthesized Li<sub>4</sub>Ti<sub>5</sub>O<sub>12</sub>/graphene-IL (IL implies ionic liquid) hybrid material using the microwave-assisted hydrothermal method. In this synthesis method, ionic liquid of C<sub>12</sub>H<sub>23</sub>ClN<sub>2</sub> ([Omim]Cl) was used as the exfoliating agent, which controlled the microstructures of graphene sheets and induced the growth of Li<sub>4</sub>Ti<sub>5</sub>O<sub>12</sub> nanoparticles (18–20 nm) on the graphene sheet. TEM studies also suggest that when synthesis was completed without using the [Omim]Cl, only a few Li<sub>4</sub>Ti<sub>5</sub>O<sub>12</sub> nanoparticles were anchored on the graphene sheet, whereas most of the particles were aggregated and detached from the graphene sheets. The

$\text{Li}_4\text{Ti}_5\text{O}_{12}$ /graphene-IL hybrid electrode delivered a reversible capacity of  $\sim 159 \text{ mAhg}^{-1}$  at 0.5 C after 100 cycles.<sup>389</sup> In addition, the  $\text{Li}_4\text{Ti}_5\text{O}_{12}$ /graphene-IL hybrid exhibited good rate capability. After cycling at different rates from 0.2 to 20 C, when the current rate was reduced to 0.2 C, the reversible capacity could be completely recovered and  $\sim 162 \text{ mAhg}^{-1}$  could be maintained after 80 cycles [Fig. 22]. The EIS study further suggests that the low charger transfer resistance and higher diffusion coefficient in  $\text{Li}_4\text{Ti}_5\text{O}_{12}$ /graphene hybrid than the bare  $\text{Li}_4\text{Ti}_5\text{O}_{12}$  nanoparticles electrode was the main reason for the improved electrochemical performance, attributed to good electrical contact between the RGO and  $\text{Li}_4\text{Ti}_5\text{O}_{12}$  nanoparticles.<sup>390-391</sup>

## 7. Metal-oxide/graphene hybrid as cathode materials

Although carbon materials cannot directly provide storage capacity for  $\text{Li}^+$  in the cathode, they can assist in improving the performance significantly. They are expected to improve the electrical conductivity and stability, and inhibit the agglomeration of the cathode materials.<sup>130</sup> In this context, graphene is advantageous compared to other carbonaceous materials.<sup>392</sup> The exceptional properties of the graphene also provide a high specific surface area, higher electrical conductivity, and chemical and mechanical stability to cathode materials. In general, lithium-manganese oxide and vanadium oxides have been widely used with graphene to fabricate hybrid materials for cathodes in LIBs.

### 7.1 Lithium manganate/graphene hybrid

Although  $\text{LiCoO}_2$  has been widely used as a cathode material for LIBs, several drawbacks such as high cost and toxicity hinder its applicability. Alternatively, due to the high energy density, better operating safety, low toxicity, and low cost, spinel-type lithium manganate ( $\text{LiMn}_2\text{O}_4$ ) has proven to be a promising cathode material.<sup>393</sup> Nevertheless, low electrical conductivity and poor cycling performance are the main issues with this material.<sup>394</sup> Xu et al.<sup>395</sup> studied the Li storage property of  $\text{LiMn}_2\text{O}_4$ /graphene hybrid. In order to synthesize  $\text{LiMn}_2\text{O}_4$ /graphene hybrid,  $\text{LiMn}_2\text{O}_4$  nanoparticles were prepared using the sol-gel method and then mixed with GNS by ultrasonic agitation. This hybrid was composed of  $\text{LiMn}_2\text{O}_4$  nanoparticles ( $\sim 100 \text{ nm}$ ), dispersed on the surface of GNS. The  $\text{LiMn}_2\text{O}_4$ /graphene hybrid (with 5 wt% graphene) electrode delivered a reversible capacity of  $107 \text{ mAhg}^{-1}$  at a 50 C charge/discharge rate, which was better than that of pristine  $\text{LiMn}_2\text{O}_4$  ( $80 \text{ mAhg}^{-1}$ ). Furthermore, after cycling at various current rates from 5C to 100 C when reduced to 5 C, the reversible capacity could be completely achieved ( $\sim 115 \text{ mAhg}^{-1}$ ) after 60 cycles and the corresponding Coulombic efficiency was observed to be  $\sim 99\%$ .<sup>395</sup> Zhao et al.<sup>397</sup> fabricated  $\text{LiMn}_2\text{O}_4$ /GNS hybrids via a self-assembly process, combined with solid-state lithiation. This synthesis process involves mixing of  $\text{LiOH}$ ,  $\text{H}_2\text{O}$ , dimethylformamide, and a suspension of  $\text{Mn}_3\text{O}_4$  with hexane. Subsequent heat treatment of this mixture led to the growth of  $\text{LiMn}_2\text{O}_4$  nanoparticles on GNS. The TEM investigation showed that in the  $\text{LiMn}_2\text{O}_4$ /GNS hybrid,  $\text{LiMn}_2\text{O}_4$  nanoparticles ( $\sim 7 \text{ nm}$ ) were evenly deposited as a layer on the surface of GNS. The  $\text{LiMn}_2\text{O}_4$ /graphene (6 wt% graphene) electrode could deliver a capacity of  $\sim 110 \text{ mAhg}^{-1}$  at a constant rate of 0.2 C after 80 cycles; however, bare  $\text{LiMn}_2\text{O}_4$  exhibited only  $\sim 110 \text{ mAhg}^{-1}$  under the same conditions. Also, this hybrid exhibited a significantly higher capacity retention of  $\sim 91\%$  than that of  $\text{LiMn}_2\text{O}_4$  nanoparticles (only  $\sim 77\%$ ).<sup>396</sup> It has been reported that the flexible nature of GNS is capable of buffering the volume stain of the  $\text{LiMn}_2\text{O}_4$  grains associated with Jahn-Teller distortion, which reduces the manganese dissolution into the electrolyte. Therefore,  $\text{LiMn}_2\text{O}_4$ /RGO hybrids exhibited improved storage capacity, cycle

performance, and rate capability compared to the bare  $\text{LiMn}_2\text{O}_4$  nanoparticle and RGO electrode for LIBs.<sup>398</sup>

Bak et al.<sup>399</sup> synthesized a  $\text{LiMn}_2\text{O}_4$ /RGO hybrid using the microwave-assisted hydrothermal method. The morphological studies suggest that the surface of RGO nanosheets was well covered with thin layers of  $\text{MnO}_2$  nanoparticles with a size of 10–40 nm without agglomeration. Thus, this offered an inherent high electroactive surface area of individual  $\text{LiMn}_2\text{O}_4$  nanoparticles in the hybrid state. Such unique structural/morphological features of  $\text{LiMn}_2\text{O}_4$  on the highly conductive RGO sheets enabled a high specific capacity, high rate capability and good cycling stability. This hybrid could deliver a specific capacity of  $137 \text{ mAhg}^{-1}$  at 1 C, and a discharge capacity of  $117 \text{ mAhg}^{-1}$  at 50 C rate. Furthermore, the  $\text{LiMn}_2\text{O}_4$ /RGO hybrid exhibited the capacity retention of  $\sim 90\%$  at 1 C rate and  $\sim 96\%$  at 10 C rate over 100 cycles.<sup>399</sup> The  $\text{LiMn}_2\text{O}_4$  nanoparticles were *in-situ* coated with a graphene-like membrane (GLM) using the liquid-polyacrylonitrile (LPAN) as the carbon source.<sup>400</sup> The electrochemical performances suggest that coating of GLM can significantly improve the cycling stability and discharge capacity of  $\text{LiMn}_2\text{O}_4$  nanoparticle. Additionally,  $\text{LiMn}_2\text{O}_4$  nanoparticles coated with a calcined 20 wt% LPAN-GLM could deliver the discharge capacity of  $\sim 131.1 \text{ mAhg}^{-1}$  at 0.1 C and retain a 96% capacity after 50 cycles [Fig. 23]. The improved electrochemical performance was ascribed to the reduced dissolution of manganese in the electrolyte and smaller charge transfer resistance generated by GLM. In order to improve the electrochemical performance of the  $\text{LiMn}_2\text{O}_4$ /graphene hybrid, a layer of ZnO was further coated through ALD.<sup>401</sup> ZnO-modified  $\text{LiMn}_2\text{O}_4$ /graphene electrode exhibited improved electrochemical performances over the  $\text{LiMn}_2\text{O}_4$ /graphene hybrid and bare  $\text{LiMn}_2\text{O}_4$  nanoparticle. The ZnO modified  $\text{LiMn}_2\text{O}_4$ /graphene hybrid electrode retained a capacity of  $\sim 122.9 \text{ mAhg}^{-1}$  after 100 cycles at 1C, which was higher than  $\sim 115 \text{ mAhg}^{-1}$  from the  $\text{LiMn}_2\text{O}_4$ /graphene hybrid and  $109 \text{ mAhg}^{-1}$  from the bare  $\text{LiMn}_2\text{O}_4$  electrode. Additionally, the modification of  $\text{LiMn}_2\text{O}_4$ /graphene by ZnO improved the rate capability compared to the  $\text{LiMn}_2\text{O}_4$ /graphene electrode. After cycling (50 cycles) at different current rates from 0.1 C to 2C when the current rate was reduced to 0.1 C, a capacity of  $\sim 180 \text{ mAhg}^{-1}$  could be achieved, which was nearly the same as that measured after 10 cycles. Similarly, the graphene/ $\text{Y}_2\text{O}_3$ / $\text{LiMn}_2\text{O}_4$  hybrid electrode exhibited electrochemical performance superior to graphene/ $\text{LiMn}_2\text{O}_4$ ,  $\text{Y}_2\text{O}_3$ / $\text{LiMn}_2\text{O}_4$ , and pristine  $\text{LiMn}_2\text{O}_4$  electrode as shown in Table 2.<sup>402</sup>

### 7.2 Vanadium oxide/graphene hybrid

$\text{V}_2\text{O}_5$  is a promising electrode material which exhibits theoretical capacities of  $1471 \text{ mAhg}^{-1}$  and  $290 \text{ mAhg}^{-1}$  as an anode and cathode materials, respectively. However, it suffers from problems related to volume expansion, structural collapse, and the formation of an unstable intermediate during the charge and discharge process, which leads to significant decay of the capacity.<sup>403-404</sup> Blending vanadium oxide nanostructured with graphene to form hybrid electrode materials can improve their electrochemical performance.<sup>405-408</sup> Rui et al.<sup>409</sup> synthesized RGO-supported polycrystalline  $\text{V}_2\text{O}_5$  spheres via a solvothermal method assisted by post annealing treatment. Using this method, reduced vanadium oxide (rVO) nanoparticles (size 10–50 nm) were grown on RGO sheets through heterogeneous nucleation during the solvothermal process. Subsequently, rVO nanoparticles were oxidized in  $\text{V}_2\text{O}_5$  by annealing in air at  $350^\circ\text{C}$ . The morphological studies using FE-SEM/TEM revealed that  $\text{V}_2\text{O}_5$  nanoparticle assembled into porous spheres having sizes of 200–800 nm and grown on RGO. This  $\text{V}_2\text{O}_5$ /RGO hybrid exhibited improved cycling stability/rate capability due to conductive network, structural

integrity, and inhibited particle agglomeration. The  $V_2O_5$ /RGO (~46% RGO) hybrid electrode delivered a discharge capacity of ~202  $\text{mAhg}^{-1}$  at a current density of 90  $\text{mA g}^{-1}$  during the 50<sup>th</sup> cycle, corresponding to 85% of the initial capacity. Furthermore, the Coulombic efficiency was maintained at ~100% for the first 50 cycles, while at a high current density of 5700  $\text{mA g}^{-1}$ , a discharge capacity of ~93  $\text{mAhg}^{-1}$  during the 200<sup>th</sup> cycle was achieved.<sup>409</sup>

Ho et al.<sup>410</sup> synthesized  $V_2O_5$ /RGO ball hybrid using the spray-pyrolysis method assisted by thermal treatment. In this synthesis approach, graphene/ $VO_2$  hybrid was prepared by spray pyrolysis using a colloidal solution of GO and ammonium vanadate and then calcined at 300 °C in an air atmosphere. The morphological investigation suggests that this hybrid composed of  $VO_2$  nanoparticles was decorated on crumbled-graphene balls, which resembled a hierarchical structure.<sup>410</sup> When used as the cathode, at a current density of 1  $\text{A g}^{-1}$ , the initial charge and discharge capacities were observed to be 280 and 282  $\text{mAhg}^{-1}$ , respectively, with a Coulombic efficiency of ~100%. In contrast, the macroporous  $V_2O_5$  delivered the initial charge and discharge capacities of 221 and 205  $\text{mAhg}^{-1}$ , respectively, and the corresponding Coulombic efficiency was observed to be only ~93%. Furthermore, the  $V_2O_5$  ball/RGO ball hybrid electrode exhibited good cyclability, rate capability, and columbic efficiency. At a current density of 600  $\text{mA g}^{-1}$  and 1000  $\text{mA g}^{-1}$ ,  $V_2O_5$  ball/RGO ball hybrid electrode delivered a reversible capacity of ~250  $\text{mAhg}^{-1}$  up to 100 cycles with 100% columbic efficiency. Similarly, the improved electrochemical performance of the  $V_2O_5$  nanowire/graphene hybrid electrode was ascribed to the combined effect of using graphene with excellent conductivity and nanowires of  $V_2O_5$ , which provide a short diffusion pathway for  $\text{Li}^+$ .<sup>411</sup> Cong et al.<sup>412</sup> synthesized  $V_2O_5$  nanowires/RGO hybrid material using the electrospinning method. This hybrid consists of  $V_2O_5$  nanowires which have diameters of about 100–200 nm and are several micrometers in length. It was observed that this hybrid with 1 wt% of RGO could deliver discharge capacities up to 225  $\text{mAhg}^{-1}$  and 125  $\text{mAhg}^{-1}$  (after 60 cycles with a rate of 0.2 C) when cycled between 2.0 and 4.0 V, respectively. Recently, Yang et al.<sup>413</sup> synthesized a  $V_2O_5$ /GNRs (graphene nanoribbons) hybrid. In this hybrid,  $V_2O_5$  nanoparticles were entrapped by GNRs and formed a 3-D conductive network [Fig. 24]. This hybrid electrode could deliver a capacity of ~278  $\text{mAhg}^{-1}$  and 165  $\text{mAhg}^{-1}$  at the current rate of 0.1 C and 2 C, respectively [Fig. 25]. However, it retained only 78% of its initial capacity (at 0.1 C) when measured after 100 cycles.

Among the metastable oxides of vanadium,  $VO_2$  can show superior performance compared to the well-known  $V_2O_5$ . Shi et al.<sup>414</sup> synthesized a  $VO_2$ -nanoribbon/graphene-woven hybrid via the hydrothermal method. This hybrid electrode exhibited a discharge capacity of 380  $\text{mAhg}^{-1}$  at a current density of 0.1  $\text{mA g}^{-1}$ , and 99% of the capacity was retained after 50 cycles. Similarly, an improved capacity (~450  $\text{mAhg}^{-1}$ ) of the  $VO_2$  nanotube/graphene hybrid compared to bare  $VO_2$  was ascribed to the interaction between the  $VO_2$  nanotubes and graphene. In the hybrid form, the graphene matrix inhibited the aggregation of the  $VO_2$  nanotubes while enhancing the charge-transfer process, which improves the cycling stability.<sup>415</sup> Therefore, at current densities of 40  $\text{mA g}^{-1}$  and 100  $\text{mA g}^{-1}$ , this hybrid electrode delivered capacities of ~320  $\text{mAhg}^{-1}$  and 160  $\text{mAhg}^{-1}$  (after 20 cycles), respectively, measured in the potential range of 4.0–1.5 V.<sup>415</sup> Recently,  $V_2O_5$  quantum-dot (QD)/graphene hybrid was synthesized by Han et al.<sup>416</sup>, using a controlled hydrothermal method. It was observed that uniformly dispersed  $V_2O_5$  QD (~2 nm) on the RGO can provide more electroactive sites and significantly reduces the diffusion length for  $\text{Li}^+$ . Therefore, after 300 cycles at a current density of 100  $\text{mA g}^{-1}$ , a reversible capacity of 245  $\text{mAhg}^{-1}$  with a retention value of 89%

was observed. In addition, it showed superior rate capability compared to the bare  $V_2O_5$  nanowire electrode, when cycled at different current densities (~100% capacity retention measured after 10<sup>th</sup> and 50<sup>th</sup> cycles at current density of 50  $\text{mA g}^{-1}$ ).

Sun et al.<sup>417</sup> synthesized free-standing hybrid film of  $V_2O_5 \cdot 0.86H_2O$  nanoribbons and RGO using the hydrothermal method. The SEM images revealed that the thickness of the film was ~20  $\mu\text{m}$  and this hybrid structure was formed by intertwining ribbons. Such a hybrid network can be helpful to achieve good contact between RGO and the  $V_2O_5 \cdot 0.86H_2O$  ribbon, essentially providing an easy electron pathway and a  $\text{Li}^+$  host. This hybrid film exhibited a reversible specific capacity 160  $\text{mAhg}^{-1}$  at a current density of 70  $\text{mA g}^{-1}$  and retained 133  $\text{mAhg}^{-1}$  after 200 cycles, whereas it delivered ~60  $\text{mAhg}^{-1}$  (by 30 cycles) and ~110  $\text{mAhg}^{-1}$  (10 cycles) at high current densities of 1120  $\text{mA g}^{-1}$  and 320  $\text{mA g}^{-1}$ , respectively. Recently, Nethravathi et al.<sup>418</sup> synthesized N-doped graphene- $VO_2$  nanotube hybrid material. This hybrid consists of a 3D flower-like structure, exhibiting high capacity (300  $\text{mAhg}^{-1}$  at 50  $\text{mA g}^{-1}$  after 20 cycles), good cycling stability (251  $\text{mAhg}^{-1}$  50  $\text{mA g}^{-1}$  after 50 cycles), and columbic efficiency (only 0.79 % fading) compared to bare  $VO_2$  electrode. This was attributed to the increased electronic conductivity and short diffusion length facilitated by ultrathin nanosheets of graphene. Reddy et al.<sup>419</sup> synthesized GO coated  $VO_2$  hybrid using vanadyl (IV) sulfate ( $\text{VOSO}_4$ ) using the hydrothermal method under Ar atmosphere. The electrochemical studies revealed that, compared to carbon coated  $VO_2$  (~110  $\text{mAhg}^{-1}$  at 100  $\text{mA g}^{-1}$  by 20 cycles), GO coated  $VO_2$  electrode could deliver higher discharge capacity (~160  $\text{mAhg}^{-1}$  at 100  $\text{mA g}^{-1}$  by 20 cycles). These observations suggest that graphene can be advantageous over the other carbon nanostructures for improving the performances of anode materials.

In addition, Table 2 summarizes the different types of metal-oxide/graphene hybrids electrode materials and their performances for LIBs.<sup>420-445</sup>

## 8. Graphene/metal oxide hybrids for flexible LIBs

The demand for flexible LIBs to design a variety of flexible portable electronic devices is rapidly increasing. Flexible LIBs possess several unique features such as good flexibility, easy portability and are lightweight. However, compared to the conventional LIBs, the fabrication of flexible LIBs is very challenging. This is mainly because of the lack of reliable materials that combine a high mechanical stability with electrical conductivity; meanwhile, they should also possess high stability during the electrochemical reactions. Therefore, several smart approaches including the growth of conductive nanomaterials onto textiles and paper have recently been reported.<sup>446-447</sup> Due to good mechanical flexibility and electrical conductivity, graphene has also shown its potential in the design of flexible LIBs.<sup>448-449</sup> Gwon et al.<sup>450</sup> reported a novel approach to design the flexible LIB using the free-standing graphene paper as the electrode and  $V_2O_5$ /graphene hybrid paper as the cathode. In this approach, graphene paper was prepared through a vacuum filtration process assisted by thermal treatment at 550 °C for 2h under an Ar atmosphere. The  $V_2O_5$ /graphene hybrid paper was synthesized using the pulsed laser deposition (PLD) technique. The target of  $V_2O_5$  was prepared by cold pressing from  $V_2O_5$  powder, which was further deposited onto the graphene paper. The complete LIB was assembled with the lithiated graphene paper as the anode and the  $V_2O_5$ /graphene hybrid paper as the cathode, separated by a separator dipped in an electrolyte (1 M  $\text{LiPF}_6$  in ethyl carbonate/dimethyl carbonate). The cyclic performance of the assembled battery was measured between 1.7 and 3.8 V at a constant current density of 10  $\text{mA cm}^{-2}$ , showing the typical charge/discharge characteristic of the amorphous  $V_2O_5$  cathode. The first

charge/discharge capacities were observed to be  $\sim 15 \text{ mAh cm}^{-2}$  with a negligible initial irreversible capacity. Moreover, reversible charging/discharging was maintained during the prolonged cycling with a small decay in capacity. This flexible battery was also able to operate when rolled up or twisted and exhibited good charge/discharge capability under the full mechanical flexibility [Fig. 26].

Recently, another flexible LIB was designed by Li et al.<sup>451</sup> This battery was assembled of 3D graphene foam (GF) loaded with  $\text{LiFePO}_4$  and  $\text{Li}_4\text{Ti}_5\text{O}_{12}$ , which were further used as the cathode and anode, respectively. In order to prepare the anode,  $\text{Li}_4\text{Ti}_5\text{O}_{12}$  was synthesized using a hydrothermal reaction among  $\text{Ti}-(\text{OC}_3\text{H}_7)_4$ ,  $\text{LiOH}$ , and  $\text{H}_2\text{O}_2$  in the presence of graphene foam and the synthesized sample was heated at  $550^\circ\text{C}$  in Ar atmosphere. On the other hand, the cathode was prepared by hydrothermal reactions among ammonium dihydrogen phosphate ( $\text{NH}_4\text{H}_2\text{PO}_4$ ), iron(III) nitrate hydrate ( $\text{Fe}(\text{NO}_3)_3 \cdot 0.9\text{H}_2\text{O}$ ) and lithium acetate hydrate ( $\text{CH}_3\text{COOLi} \cdot 2\text{H}_2\text{O}$ ) in the presence of graphene foam. The as prepared sample was further heated at  $720^\circ\text{C}$  under a mixture of hydrogen and argon gas. The complete battery was comprised of free-standing  $\text{LiFePO}_4/\text{GF}$  and  $\text{Li}_4\text{Ti}_5\text{O}_{12}/\text{GF}$  electrodes with a thickness of  $\sim 100 \mu\text{m}$ , which were laminated on both sides of a polypropylene separator and subsequently sealed with poly(dimethyl siloxane) with a thickness of  $\sim 250\text{-}\mu\text{m}$ . The  $\text{LiPF}_6$  in ethylene carbonate/dimethyl carbonate was used as the electrolyte. This flexible LIB exhibited an initial discharge capacity of  $\sim 143 \text{ mAh g}^{-1}$  at 0.2 C rate with a Coulombic efficiency of 98%. In addition,  $\sim 97\%$  capacity was retained after the first 15 cycles under the flat state, whereas  $\sim 95\%$  capacity was retained after another 15 cycles under the bent state (radius of bent was 5 mm). Furthermore, when the battery was operated at 10 C rate, it delivered a capacity of  $\sim 117 \text{ mAh g}^{-1}$  and could be cycled over 100 cycles while fading the capacity to only 4%.

Wang et al.<sup>452</sup> synthesized a flexible and free-standing hybrid film of  $\text{Fe}_3\text{O}_4/\text{graphene}$ , through vacuum filtration and thermal reduction processes. This hybrid film comprised a 3D-graphene network in which hollow and porous  $\text{Fe}_3\text{O}_4$  spindles were uniformly sandwiched between graphene layers. This hybrid film was further used as a binder-free and free-standing anode for LIB. The  $\text{Fe}_3\text{O}_4/\text{graphene}$  hybrid film with an optimized concentration of graphene (39.6 wt%) exhibited a specific capacity of  $\sim 1555 \text{ mAh g}^{-1}$  at  $100 \text{ mA g}^{-1}$ . Moreover, at current densities of 200 and  $500 \text{ mA g}^{-1}$ , it also showed capacities of 940 and  $660 \text{ mAh g}^{-1}$ , respectively, after 50 cycles with a Coulombic efficiency of  $\sim 100\%$ .

Recently, nanoporous  $\text{NiO}/\text{graphene}$ ,  $\text{Co}_3\text{O}_4/\text{graphene}$ , and  $\text{Fe}_3\text{O}_4/\text{graphene}$  hybrid have been investigated as flexible electrodes in LIBs.<sup>453</sup> In these studies a controlled nanoporous graphene paper was synthesized using carbon nanofiber as the graphene precursor and spherical silica as hard templates with different diameters. The nanoporous graphene paper was further immersed in the chemical solutions containing metal salts of nickel, cobalt, and iron; subsequently, thermal treatment led to the formation of 3D flexible electrode. These hybrids could be directly used as the anode in LIB. The  $\text{Fe}_3\text{O}_4/\text{graphene}$  hybrid electrode exhibited a specific capacity of  $\sim 1427.5 \text{ mAh g}^{-1}$  at a high current density of  $1 \text{ Ag}^{-1}$  and showed good cycling ability. Moreover, it showed good rate capabilities of  $3 \text{ Ag}^{-1}$  and  $5 \text{ Ag}^{-1}$  at the steady reversible capacities of 840.0 and  $592.5 \text{ mAh g}^{-1}$ , respectively. On the other hand,  $\text{NiO}/\text{graphene}$  hybrid delivered a specific discharge capacity of  $\sim 739.3 \text{ mAh g}^{-1}$  after 70 cycles at a current density of  $100 \text{ mA g}^{-1}$ , whereas  $\text{Co}_3\text{O}_4/\text{graphene}$  exhibited a specific discharge capacity of  $\sim 684.0 \text{ mAh g}^{-1}$ . These strategies could provide new opportunities for the development of flexible LIBs with high capacity to power flexible electronic devices in a broad range of unique applications.

## 9. Conclusions and future study

Graphene has shown potential for the fabrication of electrode materials in LIBs owing to unique properties such as 2D structure, excellent electrical/thermal conductivity, chemical and mechanical stability, and very high specific surface area. Recent advances in the synthesis of graphene and its hybrid with various types of metal-oxides nanoparticles have been discussed, along with their applications as electrode materials for LIBs. In contrast to other carbon materials such as graphite,  $\text{C}_{60}$ , and CNTs, graphene not only serves as a 2D matrix for various types of inorganic nanostructures, it also acts as a building block and establishes inimitable superstructures with interconnected networks; this can be more helpful for the fast transportation of  $\text{Li}^+$ , and can therefore dramatically improve the performance of electrode materials. An LIB electrode should satisfy basic requirements such as high capacity, high energy, and high power density with a long cycling stability. The current research has shown that graphene in a hybrid form can accomplish synergetic effects and can therefore fulfill these requirements. Graphene and its derivatives such as RGO and functionalized GO can be introduced into a variety of metal-oxide nanoparticles to form graphene-based metal-oxide hybrids electrode materials. The incorporation of graphene into these nanoparticles can significantly improve their properties, and possibly lead to novel properties. Furthermore, in the hybrid form, graphene can serve as a 2D substrate or template to provide a platform for the controlled growth of the nanoparticles. The presence of graphene can prevent the agglomeration of nanoparticles and volume change, whereas the existence of nanoparticles between the layers of graphene can effectively suppress the re-stacking of graphene sheets during the cycling process. The presence of graphene with nanoparticles can also form 3D interconnected porous structures. These features are helpful for providing a large surface area, high electrical conductivity, fast charge transport, and excellent wettability towards the electrolyte, and therefore significantly improve the performance of the electrode materials for LIBs.

Research on metal-oxide/graphene hybrid nanostructure electrode materials is still in the early stage, and more studies for modifications and development of these hybrids are required to achieve desired electrochemical properties. Several challenges still need to be overcome. First, as an important component of the metal-oxide/graphene hybrids, the synthesis of graphene itself is not mature in terms of the control of characteristics such as the morphology, defects, and functionalities. Therefore, new approaches for the synthesis of graphene with high quality at large scale and low cost need to be developed. Second, the functionalization of graphene and controlling the interface between the nanoparticles and graphene are crucial. The functionalization involves a charge transfer process that affects the performance of the hybrid materials. Thus, a good understanding of the surface chemistry between graphene and metal-oxide nanoparticles is needed. Third, the mechanism of improved performance is partially unclear, and the relationship between the number of graphene layers, defects, disordered features, and the lithium storage mechanism is also critical. Moreover, attention should be given to the synthesis approaches of the hybrid with controlled structures regarding morphology, phase composition, and reproducible features. The synthesis and modification of these hybrid nanostructures should not be the only focus, and hybrid materials with high capacity and cycling stability must also be designed. Graphene based metal oxide hybrids are expected to be developed as robust electrode materials for LIBs. It is believed that metal-oxide/graphene hybrid electrode materials will find practical applications in LIBs in the future.

**Acknowledgements**

This study was supported by the Converging Research Center Program (2014M3C1A8048834) and the Basic Research Laboratory Program (2014R1A4A1008140) through the National Research Foundation (NRF) funded by the Ministry of Science, ICT & Future Planning. Author M.S. acknowledges the Department of Science & Technology, Govt of India for awarding the DST-INSPIRE Fellowship [IFA-13 MS-02] 2014. J.S. acknowledges the Department of Science & Technology, Govt of India for awarding the DST-INSPIRE Fellowship [IFA-13 CH-105] 2013.

**Abbreviations**

|   |   |
|---|---|
| 2D  | two dimensional   |
| 3D PG-Mn  | MnO <sub>2</sub> /3D porous graphene                                    |
| 3D  | three-dimensional   |
| ACNTs   | amorphous carbon nanotubes  |
| AFM   | atomic force microscopy   |
| Al  | aluminum  |
| ALD   | atomic layer deposition   |
| Ar  | argon   |
| BET   | Brunauer-Emmet-Teller   |
| C <sub>60</sub>   | fullerene   |
| C-Li <sub>4</sub> Ti <sub>5</sub> O <sub>12</sub> /graphene | carbon coated Li <sub>4</sub> Ti <sub>5</sub> O <sub>12</sub> /graphene |
| cm <sup>2</sup> V <sup>-1</sup> s <sup>-1</sup>             | centimeter <sup>2</sup> volt <sup>-1</sup> sec <sup>-1</sup>            |
| CNT   | carbon nanotubes  |
| Co <sub>3</sub> O <sub>4</sub>                              | cobalt (II, III) oxide  |
| Cu <sub>2</sub> O   | cuprous oxide   |
| CuO   | cupric oxide  |
| CVD   | chemical vapor deposition   |
| DFT   | density functional theory   |
| EIS   | electrochemical impedance spectroscopy                                  |
| Fe(NO <sub>3</sub> ) <sub>3</sub> ·9H <sub>2</sub> O        | ferric nitrate nonahydrate  |
| Fe <sub>3</sub> O <sub>4</sub>                              | magnetite   |
| FE-SEM  | field emission scanning microscope                                      |
| FT-IR   | Fourier transform infrared  |
| GAs   | graphene aerogels   |
| GF  | graphene foam   |
| GLM   | graphene-like membrane  |
| GNRs  | graphene nanoribbons  |
| GNS   | graphene nano-sheet   |
| GO  | graphene oxide  |
| GP  | graphene papers   |
| HNO <sub>3</sub>  | nitric acid   |
| IL  | ionic liquid  |
| In <sub>2</sub> O <sub>3</sub>                              | indium oxide  |
| KBH <sub>4</sub>  | potassium borohydride   |
| kWkg <sup>-1</sup>  | kilowatt kilogram <sup>-1</sup>   |
| Li <sup>+</sup>   | lithium ion   |
| Li <sub>4</sub> Ti <sub>5</sub> O <sub>12</sub>             | lithium-titanate  |
| LIBs  | lithium-ion batteries   |
| LICMC   | lithium carboxymethyl cellulose   |
| LiCoO <sub>2</sub>  | lithium cobalt oxide  |
| LiFePO <sub>4</sub>   | lithium iron phosphate  |
| LiMn <sub>2</sub> O <sub>4</sub>                            | lithium manganate   |
| LiPF <sub>6</sub>   | lithium hexafluorophosphate   |
| Li-RGO  | Li <sup>+</sup> intercalated RGO  |
| LPAN  | liquid-polyacrylonitrile  |
| m <sup>2</sup> g <sup>-1</sup>                              | meter <sup>2</sup> gram <sup>-1</sup>                                   |

|   |  |
|---|--|
| mAg <sup>-1</sup>   | milli-ampere gram <sup>-1</sup>                    |
| mAhg <sup>-1</sup>  | milli-ampere hour gram <sup>-1</sup>               |
| MIO   | mesoporous iron oxide                              |
| MMG   | microspheres composed of multilayer graphene       |
| Mn <sub>3</sub> O <sub>4</sub>                            | manganese (II, III) oxide                          |
| MnO <sub>2</sub>  | manganese (IV) dioxide                             |
| MoO <sub>2</sub>  | molybdenum dioxide                                 |
| MoO <sub>3</sub>  | molybdenum trioxide                                |
| MWNTs   | multi-walled carbon nanotubes                      |
| N <sub>2</sub> H <sub>4</sub>                             | hydrazine  |
| Nio   | nickel oxide                                       |
| NS  | nanosheets   |
| nt-TiO <sub>2</sub>                                       | titania nanotubes                                  |
| PEI   | poly (ethylene imine)                              |
| PVDF  | polyvinylidene difluoride                          |
| QDs   | quantum dots                                       |
| RGO   | reduced graphene oxide                             |
| rVO   | reduced vanadium oxide                             |
| SEI   | solid electrolyte interphase                       |
| SEM   | scanning electron microscope                       |
| S-GNS   | sulfur doped graphene                              |
| SnO <sub>2</sub>  | tin oxide  |
| SRFG  | solvothermally reduced and functionalized graphene |
| TEM   | transmission electron microscope                   |
| TiO <sub>2</sub> (B)                                      | monoclinic titanium dioxide                        |
| TiO <sub>2</sub>  | titanium dioxide                                   |
| TiO <sub>2</sub> @TiO <sub>x</sub> N <sub>y</sub> /TiN-GS | surface nitrated TiO <sub>2</sub> /graphene        |
| V <sub>2</sub> O <sub>5</sub>                             | vanadium penta-oxide                               |
| VO <sub>2</sub>   | vanadium dioxide                                   |
| Wm <sup>-1</sup> K <sup>-1</sup>                          | watt per meter kelvin                              |
| XPS   | x-ray photoelectron                                |
| α-Fe <sub>2</sub> O <sub>3</sub>                          | hematite   |
| γ-Fe <sub>2</sub> O <sub>3</sub>                          | maghemite  |

**Notes and references**

<sup>1</sup>Advanced Materials Institute of BIN Technology (BK21 plus Global), Dept. of BIN Fusion Tech., Chonbuk National University, Jeonju, Jeonbuk, 561-756, Republic of Korea.

<sup>2</sup>Department of Physics and Astrophysics, University of Delhi, Delhi-110007, India.

<sup>3</sup>Department of Applied Chemistry, Delhi Technological University, Shahbad Daultapur, Main Bawana Road, Delhi 110042, India.

<sup>4</sup>Surface Engineering & Tribology Division, CSIR- Central Mechanical Engineering Research Institute, Durgapur, 713209, India.

<sup>5</sup>Carbon Composite Research Center & Department of Polymer & Nano Science and Technology, Chonbuk National University Jeonju, Jeonbuk 561-756, Republic of Korea

\*Corresponding author: Prof Joong Hee Lee (e-mail: jhl@chonbuk.ac.kr, Tel.: 82-63-270-2342; Fax: 82-63-270-2341)

- 1 A. Vu, Y. Qian, A. Stein, *Adv. Energy Mater.*, 2012, 2, 1056–1085.
- 2 M. Hu, X. Pang, Z. Zhou, *J. Power Sources*, 2013, 237, 229-242.
- 3 W. Lu, R. Hartman, *J. Phys. Chem. Lett.*, 2011, 2, 655–660.

- 4 E. Yildirim, S. Sarac, A. Aslan, *Renew Sust Energ Rev.*, 2012, 16, 6770–6774.
- 5 B. Batidzirai, E.M.W. Smeets, A.P.C. Faaij, *Renew Sust Energ Rev.*, 2012, 16, 6598–6630.
- 6 M. Beaudin, H. Zareipour, A. Schellenberglobe, W. Rosehart, *Energy Sust Develop.*, 2010, 14, 302–314.
- 7 M. Wrightn, A. Uddin, *Sol Energ Mat Sol C*, 2012, 107, 87–111.
- 8 B. P. Tripathi, V. K. Shahi, *Prog Polym Sci.*, 2011, 36, 945–979.
- 9 L. X. Yuan, Z. H. Wang, W. X. Zhang, X. L. Hu, J. T. Chen, Y. H. Huang, J. B. Goodenough, *Energy Environ. Sci.*, 2011, 4, 269–284.
- 10 K. Sheng, Y. Sun, C. Li, W. Yuan, G. Shi, *Sci Rep.*, 2012, 2, 247–251.
- 11 R. Liu, J. Duay, S. B. Lee, *Chem. Commun.*, 2011, 47, 1384–1404.
- 12 A. Manthiram, A. Vadivel Murugan, A. Sarkar, T. Muraliganth, *Energy Environ. Sci.*, 2008, 1, 621–638.
- 13 A. S. Arico, P. Bruce, B. Scrosati, J. M. Tarascon, W. V. Schalkwijk, *Nat Mater.*, 2005, 4, 366–377.
- 14 P. G. Bruce, B. Scrosati, J. M. Tarascon, *Angew. Chem. Int. Ed.*, 2008, 47, 2930–2946.
- 15 M. G. Kim, J. Cho, *Adv. Funct. Mater.*, 2009, 19, 1497–1514.
- 16 Y. Hu, X. Sun, *J. Mater. Chem. A*, 2014, 2, 10712–10783.
- 17 B.Y.G. Guo, J. S. Hu, L. J. Wan, *Adv. Mater.*, 2008, 20, 2878–2887.
- 18 Y. Zhang, H. Feng, X. Wu, L. Wang, A. Zhang, T. Xia, H. Dong, X. Li, L. Zhang, *Int J Hydrogen Energy*, 2009, 34, 4889–4899.
- 19 W. Lu, A. Goering, L. Qu, L. Dai, *Phys Chem Chem Phys.*, 2012, 14, 12099–104.
- 20 B. J. Landi, M. J. Ganter, C. D. Cress, R. A. DiLeo, R. P. Raffaele, *Energy Environ. Sci.*, 2009, 2, 638–654.
- 21 C. M. Schauerman, M. J. Ganter, G. Gaustad, C. W. Babbitt, R. P. Raffaele, B. J. Landi, *J. Mater. Chem.*, 2012, 22, 12008–12015.
- 22 T. Zhao, Y. Liu, T. Li, X. Zhao, *J Nanosci Nanotechnol.*, 2010, 10, 3873–3877.
- 23 B. J. Landi, R. A. DiLeo, C. M. Schauerman, C. D. Cress, M. J. Ganter, R. P. Raffaele, *J Nanosci Nanotechnol.*, 2009, 9, 3406–3410.
- 24 B. Guo, X. Wang, P. F. Fulvio, M. Chi, S. M. Mahurin, X. G. Sun, S. Dai, *Adv. Mater.*, 2011, 23, 4661–4666.
- 25 J. Chen, J. Z. Wang, A. I. Minett, Y. Liu, C. Lynam, H. Liu, G. G. Wallace, *Energy Environ. Sci.*, 2009, 2, 393–396.
- 26 K. Wang, Z. Li, Y. Wang, H. Liu, J. Chen, J. Holmes, H. Zhou, *J. Mater. Chem.*, 2010, 20, 9748–9753.
- 27 S. Chen, P. Chen, Y. Wang, *Nanoscale*, 2011, 3, 4323–4329.
- 28 H. Lee, J. K. Yoo, J. H. Park, J. H. Kim, K. Kang, Y. S. Jung, *Adv. Energy Mater.*, 2012, 2, 976–982.
- 29 A. K. Geim, K. S. Novoselov, *Nat. Mater.*, 2007, 6, 183–91.
- 30 Y. Kim, C. Jo, J. Lee, C. W. Lee, S. Yoon, *J. Mater. Chem.*, 2012, 22, 1453–1458.
- 31 J. Yang, J. Choi, H. Kim, M. Morita, S. Park, *J Ind Eng Chem*, 2013, 19, 1648–1652.
- 32 Y. Zhu, X. Xiang, E. Liu, Y. Wu, H. Xie, Z. Wu, Y. Tian, *Mater Res Bull*, 2012, 47, 2045–2050.
- 33 E. Liu, H. Shen, X. Xiang, Z. Huang, Y. Tian, Y. Wu, Z. Wu, H. Xie, *Mater Lett.*, 2012, 67, 390–393.
- 34 J. Jin, Z. Shi, C. Wang, *Electrochim Acta.*, 2014, 141, 302–310.
- 35 X. Li, X. B. Zhu, Y. Zhu, Z. Yuan, L. L. Si, Y. Qian, *Carbon*, 2014, 69, 515–524.
- 36 L. Zou, R. Lv, F. Kang, L. Gan, W. Shen, *J Power Sources*, 2008, 184, 566–569.
- 37 B. Tien, M. Xu, J. Liu, *Mater Lett.*, 2010, 64, 1465–1467.
- 38 S. Y. Chew, S. H. Ng, J. Wang, P. Novák, F. Krumeich, S. L. Chou, J. Chen, H. K. Liu, *Carbon*, 2009, 47, 2976–2983.
- 39 D. T. Welna, L. Qu, B. E. Taylor, L. Dai, M. F. Durstock, *J Power Sources*, 2011, 196, 1455–1460.
- 40 L. Z. Bai, D. L. Zhao, T. M. Zhang, W. G. Xie, J. M. Zhang, Z. M. Shen, *Electrochim Acta.*, 2013, 107, 555–561.
- 41 L. Qie, W. M. Chen, Z. H. Wang, Q. G. Shao, X. Li, L. X. Yuan, X. L. Hu, W. X. Zhang, Y. H. Huang, *Adv. Mater.*, 2012, 24, 2047–2050.
- 42 W. H. Shin, H. M. Jeong, B. G. Kim, J. K. Kang, J. W. Choi, *Nano Lett.*, 2012, 12, 2283–2288.
- 43 B. Zhang, Y. Liu, Z. Huang, S. Oh, Y. Yu, Y. W. Mai, J. K. Kim, *J. Mater. Chem.*, 2012, 22, 12133–12140.
- 44 G.N. Zhu, H. J. Liu, J. H. Zhuang, C. X. Wang, Y. G. Wang, Y. Y. Xia, *Energy Environ. Sci.*, 2011, 4, 4016–4022.
- 45 E. Kang, Y. S. Jung, G. H. Kim, J. Chun, U. Wiesner, A. C. Dillon, J. K. Kim, J. Lee, *Adv. Funct. Mater.*, 2011, 21, 4349–4357.
- 46 L. Shen, X. Zhang, E. Uchaker, C. Yuan, G. Cao, *Adv. Energy Mater.*, 2012, 2, 691–698.
- 47 J. Guo, Q. Liu, C. Wang, M. R. Zachariah, *Adv. Funct. Mater.*, 2011, 22, 803–811.
- 48 Z. Li, N. Liu, X. Wang, C. Wang, Y. Qi, L. Yin, *J. Mater. Chem.*, 2012, 22, 16640–16648.
- 49 S. Lee, Y. Cho, H. K. Song, K. T. Lee, J. Cho, *Angew. Chem. Int. Ed.*, 2012, 51, 8748–8752.
- 50 C. M. Julien, K. Zaghib, A. Mauger, H. Groult, *Adv. Chem. Eng. Sci.*, 2012, 2, 321–329.
- 51 L. Dimesso1, C. Spanheimer1, W. Jaegermann, Y. Zhang, and A. L. Yarin, *J. Appl. Phys.*, 2012, 111, 064307–064311.
- 52 A. Pan, J. Liu, J. G. Zhang, W. Xu, G. Cao, Z. Nie, B. W. Arey, S. Liang, *Electrochem Commun.*, 2010, 12, 1674–1677.
- 53 S. Luo, K. Wang, J. Wang, K. Jiang, Q. Li, S. Fan, *Adv. Mater.*, 2012, 24, 2294–2298.
- 54 Y. Wang, H. J. Zhang, A. S. Admar, J. Luo, C. C. Wong, A. Borgna, J. Lin, *RSC Adv.*, 2012, 2, 5748–5753.
- 55 X. F. Zhang, K. X. Wang, X. Wei, J. S. Chen, *Chem. Mater.*, 2011, 23, 5290–5292.
- 56 C. A. Bonino, L. Ji, Z. Lin, Ozan, Toprakci, X. Zhang, S. A. Khan, *ACS Appl. Mater. Interfaces*, 2011, 3, 2534–2542.
- 57 Z. Yang, G. Du, Z. Guo, X. Yu, Z. Chen, T. Guo, H. Liu, J. Mater. Chem., 2011, 21, 8591–8596.
- 58 Z. Wang, M. A. Fierke, A. Stein, *J. Electrochem Soc.*, 2008, 155, A658–A663.
- 59 Y. Luo, J. Luo, J. Jiang, W. Zhou, H. Yang, X. Qi, H. Zhang, H. J. Fan, D. Y. W. Yu, C. M. Li, T. Yu, *Energy Environ. Sci.*, 2012, 5, 6559–6566.
- 60 Y. Zhao, J. Li, Y. Ding, L. Guan, *RSC Adv.*, 2011, 1, 852–856.
- 61 J. Kong, Z. Liu, Z. Yang, H. R. Tan, S. Xiong, S. Y. Wong, X. Li, X. Lu, *Nanoscale*, 2012, 4, 525–530.
- 62 F. D. Lupo, C. Gerbaldi, G. Meligrana, S. Bodoardo, N. Penazzi, *Int. J. Electrochem. Sci.*, 2011, 6, 3580–3593.
- 63 L. B. Chen, X. M. Yin, L. Mei, C. C. Li, D. N. Lei, M. Zhang, Q. H. Li, Z. Xu, C. M. Xu, T. H. Wang, *Nanotechnology*, 2012, 23, 035402.
- 64 X. Li, A. Dhanabalan, L. Gu, C. Wang, *Adv. Energy Mater.*, 2012, 2, 238–244.
- 65 K.S. Novoselov, A.K. Geim, S.V. Morozov, D. Jiang, Y. Zhang, S.V. Dubonos, I.V. Grigorieva, A.A. Firsov, *Science*, 2004, 306, 666–669.
- 66 T. Kuila, S. Bose, A. K. Mishra, P. Khanra, N. H. Kim, J. H. Lee, *Prog. Mater. Sci.*, 2012, 57, 1061–1105.
- 67 J. C. Meyer, A. K. Geim, M. I. Katsnelson, K. S. Novoselov, T. J. Booth, S. Roth, *Nature*, 2007, 446, 60–63.

- 68 D. S. Yu, T. Kuila, N. H. Kim, P. Khanra, J. H. Lee, *Carbon*, 2013, 54, 310-322.
- 69 R. R. Nair, P. Blake, A. N. Grigorenko, K. S. Novoselov, T. J. Booth, T. Stauber, N. M. R. Peres, A. K. Geim, *Science*, 2008, 320, 1308.
- 70 Y. Yan, T. Kuila, N. H. Kim, B. C. Ku, J. H. Lee, *J. Mater. Chem. A*, 2013, 1, 5892-5901.
- 71 A. Dato, Z. Lee, K.J. Jeon, R. Erni, V. Radmilovic, T.J. Richardson, M. Frenklach, *Chem. Commun.*, 2009, 6095-6097.
- 72 S. Vadahanambi, J. H. Jung, I. K. Oh, *Carbon*, 2011, 49, 4449-4457.
- 73 Y. H. Zhang, L. J. Yue, L. F. Han, J. L. Chen, D. Z. Jia, F. Li, *Comput Mater Sci.*, 2012, 56, 95-99.
- 74 M. A. Rafiee, J. Rafiee, I. Srivastava, Z. Wang, H. Song, Z. Z. Yu, N. Koratkar, *Small* 2010, 6, 179-183.
- 75 T. Kuilla, S. Bhadra, D. Yao, N. H. Kim, S. Bose, J. H. Lee, *Prog Polym Sci.*, 2010, 35, 1350-1375.
- 76 J. Wanga, Z. Lia, G. Fana, H. Pana, Z. Chen, D. Zhang, *Scripta Mater.*, 2012, 66, 594-597.
- 77 V. Goyal, A. A. Balandin, *Appl. Phys. Lett.* 2012, 100, 073113-073116.
- 78 T. Kuila, A. K. Mishra, P. Khanra, N. H. Kim, Md. E. Uddin, J. H. Lee, *Langmuir* 2012, 28, 9825-9833.
- 79 C. M. Santos, J. Mangadlao, F. Ahmed, A. Leon, R. C. Advincula, D. F. Rodrigues, *Nanotechnology*, 2012, 23, 395101-395110.
- 80 D. Balamurugan, M. Rajkumar, S. M. Chen, R. Saraswathi, *Int J Electrochem Sci.*, 2012, 7, 3339-3349.
- 81 F. Xiao, Y. Li, X. Zan, K. Liao, R. Xu, H. Duan, *Adv. Funct. Mater.*, 2012, 22, 2487-2494.
- 82 T. Kuila, S. Bose, P. Khanra, A. K. Mishra, N. H. Kim, J. H. Lee, *Biosens Bioelectron.*, 2011, 26, 4637-4648.
- 83 J. Zhu, S. Wei, H. Gu, S. B. Rapole, Q. Wang, Z. Luo, N. Haldolaarachchige, D. P. Young, Z. Guo, *Environ. Sci. Technol.*, 2012, 46, 977-985.
- 84 W. Wang, X. Ma, Q. Wu, C. Wang, X. Zang, Z. Wang, *J. Sep. Sci.*, 2012, 35, 2266-2272.
- 85 M. Jahan, Q. Bao, K. P. Loh, *J. Am. Chem. Soc.*, 2012, 134, 6707-6713.
- 86 M. Srivastava, A. K. Das, P. Khanra, Md. E. Uddin, N. H. Kim and J. H. Lee, *J. Mater. Chem. A*, 2013, 1, 9792-9801.
- 87 S. Ameen, H. K. Seo, M. S. Akhtar, H. S. Shin, *Chem. Eng. J.*, 2012, 210, 220-228.
- 88 Q. P. Luo, X. Y. Yu, B. X. Lei, H. Y. Chen, D. B. Kuang, C. Y. Su, *J. Phys. Chem. C*, 2012, 116, 8111-8117.
- 89 P. Madhusudan, J. Yu, W. Wang, B. Cheng, G. Liu, *Dalton Trans.*, 2012, 41, 14345-14353.
- 90 A. Iwan, A. Chuchmała, *Prog Polym Sci.*, 2012, 37, 1805-1828.
- 91 W. Wua, Z. Liu, L. A. Jauregui, Q. Yu, R. Pillai, H. Caoc, J. Bao, Y. P. Chen, S. S. Pei, *Sensor Actuat B-chem*, 2010, 150, 296-300.
- 92 B. Feng, J. Xie, G. S. Cao, T. J. Zhu, X. B. Zhao, *Int. J. Electrochem. Sci.*, 2012, 7, 5195 - 5203.
- 93 D. Wang, R. Kou, D. Choi, Z. Yang, Z. Nie, J. Li, L. V. Saraf, D. Hu, J. Zhang, G. L. Graff, J. Liu, M. A. Pope, I. A. Aksay, *ACS Nano*, 2010, 4, 1587-1595.
- 94 J. M. Lee, I. Y. Kim, S. Y. Han, T. W. Kim, S. J. Hwang, *Chem. Eur. J.*, 2012, 18, 13800-13809.
- 95 Y. Zheng, J. Xie, S. Liu, W. Song, G. Cao, T. Zhu, X. Zhao, *J. Power Sources*, 2012, 202, 276-283.
- 96 Z. S. Wu, G. Zhou, L. C. Yin, W. Ren, F. Li, H. M. Cheng, *Nano Energy*, 2012, 1, 107-131.
- 97 J. Xu, K. Jang, J. Choi, J. Jin, J. H. Park, H. J. Kim, D. H. Oh, J. R. Ahn, S. U. Son, *Chem. Commun.*, 2012, 48, 6244-6246.
- 98 S. Bose, T. Kuila, A. K. Mishra, R. Rajasekar, N. H. Kim, J. H. Lee, *J. Mater. Chem.*, 2012, 22, 767-784.
- 99 L. Wang, D. Wang, X. Hu, J. Zhu, X. Liang, *Electrochim. Acta*, 2012, 76, 282-287.
- 100 T. Kuila, A. K. Mishra, P. Khanra, N. H. Kim, J. H. Lee, *Nanoscale*, 2013, 5, 52-71.
- 101 H. Huang, H. Chen, D. Sun, X. Wang, *J. Power Sources*, 2012, 204, 46-52.
- 102 S. S. J. Aravind, R. I. Jafri, N. Rajalakshmi, S. Ramaprabhu, *J. Mater. Chem.*, 2011, 21, 18199-18204.
- 103 W. I. Park, J. M. Yoon, M. Park, J. Lee, S. K. Kim, J. W. Jeong, K. Kim, H. Y. Jeong, S. Jeon, K. S. No, J. Y. Lee, Y. Sik Jung, *Nano Lett.*, 2012, 12, 1235-1240.
- 104 Y. Sun, Q. Wu, G. Shi, *Energy Environ. Sci.*, 2011, 4, 1113-1132.
- 105 S. Han, D. Wu, S. Li, F. Zhang, X. Feng, *Small*, 2013, 9, 1173-1187.
- 106 J. Hou, Y. Shao, M. W. Ellis, R. B. Moore, B. Yie, *Phys. Chem. Chem. Phys.*, 2011, 13, 15384-15402.
- 107 X. Huang, X. Qi, F. Boeya, H. Zhang, *Chem. Soc. Rev.* 2012, 41, 666-686.
- 108 B. Z. Jang, C. Liu, D. Neff, Z. Yu, M. C. Wang, W. Xiong, A. Zhamu, *Nano Lett.* 2011, 11, 3785-3791.
- 109 M. Parka, X. Zhanga, M. Chunga, G. B. Lessa, A. M. Sastry, *J. Power Sources*, 2010, 195, 7904-7929.
- 110 J. W. Fergus, *J. Power Sources*, 2010, 195, 939-954.
- 111 F. Liu, S. Song, D. Xue, H. Zhang, *Nanoscale Res Lett.*, 2012, 7, 149-165.
- 112 S. W. Kim, D. H. Seo, X. Ma, G. Ceder, K. Kang, *Adv. Energy Mater.*, 2012, 2, 710-721.
- 113 G. Pistoia, *Elsevier, Amsterdam*, 1994, vol. 5.
- 114 M. Wakihara and O. Yamamoto, *Wiley-VCH, Weinheim*, 1998.
- 115 W. Van Schalkwijk and B. Scrosati, *Kluwer Academic/Plenum, New York*, 2002.
- 116 G. A. Nazri and G. Pistoia, *Kluwer Academic Publishers, Boston, MA*, 2003.
- 117 V. Agubra, J. Fergus, *Materials*, 2013, 6, 1310-1325.
- 118 Hong Ying Mao, Yun Hao Lu, Jia Dan Lin, Shu Zhong, Andrew Thyse Shen Wee, Wei Chen, *Prog. Surf. Sci.*, 2013, 88, 132-159.
- 119 S. Pang, Y. Hernandez, X. Feng, K. Müllen, *Adv. Mater.*, 2011, 23, 2779-2795.
- 120 M. Pumera, *Chem. Rec.*, 2009, 9, 211-223.
- 121 G. Wang, X. Shen, J. Yao, J. Park, *Carbon*, 2009, 47, 2049-2053.
- 122 L. Wan, Z. Ren, H. Wang, G. Wang, X. Tong, S. Gao, J. Bai, *Diamond Relat. Mater.*, 2011, 20, 756-761.
- 123 X. Tong, H. Wang, G. Wang, L. Wan, Z. Ren, J. Bai, *J. Solid Stat Chem.*, 2011, 184, 982-989.
- 124 O. A. Vargas C., Á. Caballero, J. Morales, *Nanoscale*, 2012, 4, 2083-2092.
- 125 H. F. Xiang, Z. D. Li, K. Xie, J. Z. Jiang, J. J. Chen, P. C. Lian, J. S. Wu, Y. Yu, H. H. Wang, *RSC Adv.*, 2012, 2, 6792-6799.
- 126 W. Ahn, H. S. Song, S. H. Park, K. B. Kim, K. H. Shin, S. N. Lim, S. H. Yeon, *Electrochim. Acta.*, 2014, 132, 172-179.
- 127 P. Lian, X. Zhu, S. Liang, Z. Li, W. Yang, H. Wang, *Electrochim. Acta.*, 2010, 55, 3909-3914.
- 128 Y. Fang, Y. Lv, R. Che, H. Wu, X. Zhang, D. Gu, G. Zheng, D. Zhao, *J. Am. Chem. Soc.*, 2013, 135, 1524-1530.
- 129 X. Xiao, P. Liu, J. S. Wang, M.W. Verbrugge, M. P. Balogh, *Electrochem Commun.*, 2011, 13, 209-212.
- 130 B. Sun, B. Wang, D. Su, L. Xiao, H. Ahn, G. Wang, *Carbon*, 2012, 50, 727-733.
- 131 T. L. Lei, Z. Q. Chao, L. Jia, S. Y. Li, C. J. Peng, L. Feng, S. S. Gang, *Chinese Sci. Bull.*, 2011, 56, 3204-3212.
- 132 T. Wei, F. Wang, J. Yan, J. Cheng, Z. Fan, H. Song, *J. Electroanal. Chem.*, 2011, 653, 45-49.
- 133 E. Pollak, B. Geng, K. J. Jeon, I. T. Lucas, T. J. Richardson, F. Wang, R. Kostecki, *Nano Lett.*, 2010, 10, 3386-3388.

- 134 J. J. Zhou, W. W. Zhou, C. M. Guan, J. Q. Shen, C. Y. Ouyang, M. Lei, S. Q. Shi, W. H. Tang, *Sci China Phys Mech Astronom*, 2012, 55, 1376-1382.
- 135 N. Kheirabadi, A. Shafiekhani, *J. Appl. Phys.* 2012, 112, 124323-124327.
- 136 H. Tachikawa, Y. Nagoya, T. Fukuzumi, *J. Power Sources*, 2010, 195, 6148-6152.
- 137 Y. Chan, J. M. Hill, *Nanoscale Res. Lett.* 2011, 6, 203-208.
- 138 H. Kim, H. D. Lim, S. W. Kim, J. Hong, D. H. Seo, D. Kim, S. Jeon, S. Park, K. Kang, *Sci Rep.*, 2013, 3, 1506-1513.
- 139 R. Mukherjee, A. V. Thomas, A. Krishnamurthy, N. Koratkar, *ACS Nano*, 2012, 6, 7867-7878.
- 140 X. Zhou, Z. Liu, *IOP Conf. Series: Mater. Sci. Eng.*, 2011, 18, 062006.
- 141 D. Cai, S. Wang, L. Ding, P. Lian, S. Zhang, F. Peng, H. Wang, *J. Power Sources*, 2014 254, 198-203.
- 142 Y. Hu, X. Li, D. Geng, M. Cai, R. Li, X. Sun., *Electrochim. Acta*, 2013, 91, 227-233.
- 143 T. D. Dao, J. E. Hong, K. S. Ryu, H. M. Jeong, *Chem. Eng. J.*, 2014, 250, 257-266.
- 144 S. L. Kuo, W. R. Liu, H. C. Wu, *J. Chin. Chem. Soc.*, 2012, 59, 1220-1225.
- 145 D. W. Wang, C. Sun, G. Zhou, F. Li, L. Wen, B. C. Donose, G. Q. (Max) Lu, H. M. Cheng, I. R. Gentle, *J. Mater. Chem. A*, 2013, 1, 3607-3612.
- 146 D. Pan, S. Wang, B. Zhao, M. Wu, H. Zhang, Y. Wang, Z. Jiao, *Chem. Mater.*, 2009, 21, 3136-3142.
- 147 E. J. Yoo, J. Kim, E. Hosono, H. S. Zhou, T. Kudo, I. Honma, *Nano Lett.*, 2008, 8, 2277-2282.
- 148 A. Kumar, A. L. M. Reddy, A. Mukherjee, M. Dubey, X. Zhan, N. Singh, L. Ci, W. E. Billups, J. Nagurny, G. Mital, P. M. Ajayan, *Acs Nano*, 2011, 6, 4345-4349.
- 149 S. L. Kuo, W. R. Liu, C. P. Kuo, N. L. Wu, H. C. Wu., *J. Power Sources*, 2013, 244, 552-556
- 150 Y. Shen, H. B. Zhang, H. Zhang, W. Ren, A. Dasari, G.S. Tang, Z. Z. Yu, *Carbon*, 2013, 56, 132-138.
- 151 A. L. M. Reddy, A. Srivastava, S. R. Gowda, H. Gullapalli, M. Dubey, P. M. Ajayan, *ACS Nano*, 2010, 4, 6337-6342.
- 152 T. Hu, X. Sun, H. Sun, G. Xin, D. Shao, C. Liu, J. Lian, *Phys. Chem. Chem. Phys.*, 2014, 16, 1060-1066
- 153 H. Wang, C. Zhang, Z. Liu, L. Wang, P. Han, H. Xu, K. Zhang, S. Dong, J. Yao, G. Cui, *J. Mater. Chem.*, 2011, 21, 5430-5434.
- 154 D. Cai, S. Wang, P. Lian, X. Zhu, D. Li, W. Yang, H. Wang, *Electrochim. Acta*, 2013, 90, 492-497.
- 155 C. Ma, X. Shao, D. Cao, *J. Mater. Chem.*, 2012, 22, 8911-8915.
- 156 X. Wang, Z. Zeng, H. Ahn, G. Wang, *Appl. Phys. Lett.*, 2009, 95, 183103-183105.
- 157 Y. Yan, Y. X. Yin, S. Xin, Y. G. Guo, L. J. Wan, *Chem. Commun.*, 2012, 48, 10663-10665
- 158 Y. S. Yun, V. D. Le, H. Kim, S. J. Chang, S. J. Baek, S. Park, B. H. Kim, Y. H. Kim, K. Kang, H. J. Jin, *J. Power Sources*, 2014, 262, 79-85.
- 159 Y. Hu, X. Li, J. Wang, R. Li, X. Sun, *J. Power Sources*, 2013, 237, 41-46.
- 160 D. W. Jung, S. W. Han, J. H. Jeong, E. S. Oh., *J Electroanal. Chem*, 2013, 695, 30-37.
- 161 W. Wang, I. Ruiz, S. Guo, Z. Favors, H. H. Bay, M. Ozkan, C. S. Ozkan, *Nano Energy*, 2014, 3, 113-118.
- 162 S. C. Wang, J. Yang, X. Y. Zhou, J. Xie, L. L. Ma, B. Huang, *J Electroanal. Chem*, 2014, 722-723, 141-147.
- 163 B. P. Vinayan, R. Nagar, V. Raman, N. Rajalakshmi, K. S. Dhathathreyan, S. Ramaprabhu, *J. Mater. Chem.*, 2012, 22, 9949-9956.
- 164 T. Chen, L. Pan, K. Yu, Z. Sun, *Solid State Ionics*, 2012, 229, 9-13.
- 165 C. Kang, R. Baskaran, J. Hwang, B. C. Ku, W. Choi, *Carbon*, 2014, 68, 493-500.
- 166 S. J. R. Prabakar, Y. H. Hwang, E. G. Bae, D. K. Lee, M. Pyo., *Carbon*, 2013, 52, 128-136.
- 167 X. Su, Q. L. Wu, X. Zhan, J. Wu, S. Wei, Z. Guo, *J Mater Sci.*, 2012, 47, 2519-2534.
- 168 D. Wang, D. Choi, J. Li, Z. Yang, Z. Nie, R. Kou, D. Hu, C. Wang, L. V. Saraf, J. Zhang, I. A. Aksay, J. Liu, *Acs Nano*, 2009, 3, 907-914.
- 169 J. Wang, Y. Zhou, B. Xiong, Y. Zhao, X. Huang, Z. Shao, *Electrochim. Acta*, 2013, 88, 847-857.
- 170 H. C. Tao, L. Z. Fan, X. Yan, X. Qu, *Electrochim. Acta*, 2012, 69, 328-333.
- 171 H. Cao, B. Li, J. Zhang, F. Lian, X. Kong, Meizhen Qu, *J. Mater. Chem.*, 2012, 22, 9759-9766.
- 172 X. Zhang, P. S. Kumar, V. Aravindan, H. H. Liu, J. Sundaramurthy, S. G. Mhaisalkar, H. M. Duong, S. Ramakrishna, S. Madhavi, *J. Phys. Chem. C*, 2012, 116 14780-14788.
- 173 L. Dong, M. Li, L. Dong, M. Zhao, J. Feng, Y. Han, J. Deng, X. Li, D. Li, X. Sun, *Int. J. Hydrogen Energy*, DOI: 10.1016/j.ijhydene.2014.01.029
- 174 X. Xin, X. Zhou, J. Wu, X. Yao, Z. Liu, *Acs Nano*, 2012, 6, 11035-11043.
- 175 Y. Qiu, K. Yan, S. Yang, L. Jin, H. Deng, W. Li, *ACS Nano*, 2010, 4, 6515-6526.
- 176 T. Hu, X. Sun, H. Sun, M. Yu, F. Lu, C. Liu, J. Lian, *Carbon*, 2013, 51, 322-326.
- 177 N. Li, G. Zhou, R. Fang, F. Li, H. M. Chenga, *Nanoscale*, 2013, 5, 7780-7784.
- 178 J. Qiu, P. Zhang, M. Ling, S. Li, P. Liu, H. Zhao, S. Zhang, *ACS Appl. Mater. Interfaces*, 2012, 4, 3636-3642.
- 179 Z. Zhang, Q. Chu, H. Li, J. Hao, W. Yang, B. Lu, X. Ke, J. Li, J. Tang, *J. Colloid Interface Sci.*, 2013, 409, 38-42.
- 180 H. M. Ren, Y. H. Ding, F. H. Chang, X. He, J.Q. Feng, C.F. Wang, Y. Jiang, P. Zhang, *Appl. Surf. Sci.*, 2012, 263, 54-57.
- 181 X. Li, Y. Zhang, T. Li, Q. Zhong, H. Li, J. Huang, *J. Power Sources*, 2014, 268, 372-378.
- 182 J. Hou, R. Wu, P. Zhao, A. Chang, G. Ji, B. Gao, Q. Zhao, *Mater Lett.*, 2013, 100, 173-176.
- 183 B. Qiu, M. Xing, J. Zhang, *J. Am. Chem. Soc.*, 2014, 136, 5852-5855.
- 184 D. Li, D. Shi, Z. Liu, H. Liu, Z. Guo, *J. Nanopart. Res.*, 2013, 15, 1674.
- 185 J. Wang, L. Shen, H. Li, X. Wang, P. Nie, B. Ding, G. Xu, H. Dou, X. Zhang, *Electrochim. Acta*, 2014, 133, 209-216.
- 186 D. Cai, D. Li, S. Wang, X. Zhu, W. Yang, S. Zhang, H. Wang, *J. Alloys Compd.*, 2013, 561, 54-58.
- 187 C. Ban, M. Xie, X. Sun, J. J. Travis, G. Wang, H. Sun, A. C. Dillon, J. Lian, S. M. George, C. Ban. *Nanotechnology*, 2013, 24, 424002.
- 188 R. Menéndez, P. Alvarez, C. Botas, F. Nacimiento, R. Alcántara, J. L. Tirado, G. F. Ortiz, *J. Power Sources*, 2014, 248, 886-893.
- 189 W. Xiao, Z. Wang, H. Guo, X. Li, J. Wang, S. Huang, L. Gan, *Appl. Surf. Sci.*, 2013, 266, 148-154.
- 190 A. Hu, X. Chen, Y. Tang, L. Yang, H. Xiao, B. Fan, *Mater Lett.*, 2013, 91, 315-318.
- 191 H. Zhang, L. Zhou, C. Yu, *RSC Adv.*, 2014, 4, 495-499.
- 192 B. Zhao, R. Liu, X. Cai, Z. Jiao, M. Wu, X. Ling, B. Lu, Y. Jiang, *J. Appl. Electrochem*, 2014, 44, 53-60.
- 193 J. Ye, J. Zhang, F. Wang, Q. Su, G. Du, *Electrochim. Acta*, 2013, 113, 212-217.

- 194 L. Li, G. Zhou, Z. Weng, X. Y. Shan, F. Li, H. M. Cheng, *Carbon*, 2014, 67, 500-507.
- 195 D. Wei, J. Liang, Y. Zhu, J. Zhang, X. Li, K. Zhang, Z. Yuan, Y. Qian, *Electrochim. Acta*, 2013, 114, 779-784
- 196 G. Zhou, D. W. Wang, F. Li, L. Zhang, N. Li, Z. S. Wu, L. Wen, G. Q. (Max) Lu, H. M. Cheng, *Chem. Mater.* 2010, 22, 5306-5313.
- 197 D. J. Z. Wang, C. Zhong, D. Wexler, N. H. Idris, Z. X. Wang, L. Q. Chen, H. K. Liu, *Chem. Eur. J.*, 2011, 17, 661-667.
- 198 S. K. Behera, *J. Power Sources*, 2011, 196, 8669-8674
- 199 M. Zhang, M. Jia, *J. Alloy Compd.*, 2013, 551, 53-60.
- 200 P. Lian, X. Zhu, H. Xiang, Z. Li, W. Yang, H. Wang, *Electrochim. Acta*, 2010, 56, 834-840
- 201 X. Zhu, W. Wu, Z. Liu, L. Li, J. Hu, H. Dai, L. Ding, K. Zhou, C. Wang, X. Song, *Electrochim. Acta*, 2013, 95, 24-28.
- 202 Y. C. Dong, R. G. Ma, M. J. Hu, H. Cheng, C. K. Tsang, Q. D. Yang, Y. Y. Li, J. A. Zapien, *J. Solid Stat Chem.*, 2013, 201, 330-337.
- 203 T. Yoon, J. Kim, J. Kim, J. K. Lee, *Energies*, 2013, 6, 4830-4840.
- 204 C. Fu, G. Zhao, H. Zhang, S. Li, *Int. J. Electrochem. Sci.*, 2014, 9, 46 - 60.
- 205 S. Bhuvaneshwari, P. M. Pratheeksha, S. Anandan, D. Rangappa, R. Gopalan, T. N. Rao, *Phys. Chem. Chem. Phys.*, 2014, 16, 5284-5294.
- 206 T. Wang, X. L. Wang, Y. Lu, Q. Xiong, X. Zhao, J. Cai, S. Huang, C. Gu, J. Tu, *RSC Adv.*, 2014, 4, 322-330.
- 207 Y. Li, S. Zhu, Z. Yu, Q. Meng, T. Zhang, Q. Liu, J. Gu, W. Zhang, Z. Tao, G. Chengling, M. Zaiping, Z. Jun, D. Zhang, *Science. Adv. Mater.*, 2014, 6, 283-289.
- 208 D. Ma, S. Yuan, Z. Ca, *Chin. Sci. Bull.*, 2014, 59, 2017-2023.
- 209 B. Jin, G. Chen, X. Zhong, Y. Liu, K. Zhou, P. Sun, P. Lu, W. Zhang, J. Liang, *Ceram. Int.*, 2014, 40, 10359-10365
- 210 Y. Chang, J. Li, B. Wang, H. Luo, L. Zhi, *J. Mater. Sci. Tech.*, DOI: 10.1016/j.jmst.2014.01.010.
- 211 S. Yang, Y. Sun, L. Chen, Y. Hernandez, X. Feng, K. Müllen, *Sci Rep.*, 2012, 2, 427-453.
- 212 C. T. Hsieh, J. Y. Lin, C. Y. Mo, *Electrochim. Acta*, 2011, 58, 119-124.
- 213 M. Sathish, T. Tomai, I. Honma, *J. Power Sources*, 2012, 217, 85-91.
- 214 M. Zheng, D. Qiu, B. Zhao, L. Ma, X. Wang, Z. Lin, L. Pan, Y. Zheng, Y. Shi, *RSC Adv.*, 2013, 3, 699-703.
- 215 B. Jin, A. H. Liu, G. Y. Liu, Z. Z. Yang, X. B. Zhong, X. Z. Ma, M. Yang, H. Y. Wang, *Electrochim. Acta*, 2013, 90, 426-432.
- 216 J. Luo, J. Liu, Z. Zeng, C. F. Ng, L. Ma, H. Zhang, J. Lin, Z. Shen, H. J. Fan, *Nano Lett.*, 2013, 13, 6136-6143.
- 217 J. Zhao, B. Yang, Z. Zheng, J. Yang, Z. Yang, P. Zhang, W. Ren, X. Yan, *ACS Appl. Mater. Interfaces*, Article ASAP, DOI: 10.1021/am502574j
- 218 D. Chen, W. Wei, R. Wang, J. Zhu, L. Guo, *New J. Chem.*, 2012, 36, 1589-1595.
- 219 M. Zhang, B. Qu, D. Lei, Y. Chen, X. Yu, L. Chen, Q. Li, Y. Wang, T. Wang, *J. Mater. Chem.*, 2012, 22, 3868-3874.
- 220 Y. Yang, X. Fan, G. Casillas, Z. Peng, G. Ruan, G. Wang, M. J. Yacamán, J. M. Tour, *ACS Nano*, 2014, 8, 3939-3946.
- 221 R. Wang, C. Xu, M. Du, J. Sun, L. Gao, P. Zhang, H. Yao, C. Lin, *small*, 2014, 10, 2260-2269.
- 222 J. Kan, Y. Wang, *Sci. Rep.* 2013, 3, 3502-3511.
- 223 C. Wu, H. Zhang, Y. X. Wu, Q. C. Zhuang, L. L. Tian, X. X. Zhang, *Electrochim. Acta*, 2014, 134, 18-27
- 224 X. Wang, W. Tian, D. Liu, C. Zhi, Y. Bando, D. Golberg, *Nano Energ.*, 2013, 2, 257-267
- 225 M. Du, C. Xu, J. Sun, L. Gao, *Electrochim. Acta*, 2012, 80, 302-307.
- 226 T. Hu, M. Xie, J. Zhong, H. T. Sun, X. Sun, S. Scott, S. M. George, C. S. Liu, J. Lian, *Carbon*, 2014, 76, 141-147
- 227 S. H. Yu, D. E. Conte, S. Baek, D. C. Lee, S. K. Park, K. J. Lee, Y. Piao, Y. E. Sung, N. Pinna, *Adv. Funct. Mater.*, 2013, 23, 4293-4305.
- 228 I. T. Kim, A. Magasinski, K. Jacob, G. Yushin, R. Tannenbaum, *Carbon*, 2013, 52, 56-64.
- 229 W. Xiao, Z. Wang, H. Guo, Y. Zhang, Q. Zhang, L. Gan, W. Xiao, Z. Wang, H. Guo, Y. Zhang, Q. Zhang, L. Gan, *J. Alloy Compd.*, 2013, 560, 208-214.
- 230 S. Chen, P. Bao, G. Wang, *Nano Energ.*, 2013, 2, 425-43.
- 231 X. Y. Xue, C. H. Ma, C. X. Cui, L. L. Xing, *Solid State Sci.*, 2011, 13, 1526-1530.
- 232 G. Wang, T. Liu, Y. Luo, Y. Zhao, Z. Ren, J. Bai, H. Wang, *J. Alloy Compd.*, 2011, 509, L216-L220.
- 233 X. Zhu, Y. Zhu, S. Murali, M. D. Stoller, R. S. Ruoff, *Acs Nano*, 2011, 5, 3333-3338.
- 234 S. H. Lee, V. Sridhar, J. H. Jung, K. Karthikeyan, Y. S. Lee, R. Mukherjee, N. Koratkar, I. K. Oh, *ACS Nano*, 2013, 7, 4242-4251.
- 235 G. Wang, H. Wang, S. Cai, J. Bai, Z. Ren, J. Bai, *J. Power Sources*, 2013, 239, 37-44.
- 236 J. Yao, X. Shen, B. Wang, H. Liu, G. Wang, *Electrochem. Commun.*, 2009, 11, 1849-1852.
- 237 M. Zhang, D. Lei, Z. Du, X. Yin, L. Chen, Q. Li, Y. Wang, T. Wang, *J. Mater. Chem.*, 2011, 21, 1673-1676.
- 238 H. T. Wang, D. W. He, Y. S. Wang, H. P. Wu, J. G. Wang, *Adv. Mater. Res.*, 2012, 465, 108-111.
- 239 J. Liu, J. Huang, L. Hao, H. Liu, X. Li, *Ceram. Int.*, 2013, 39, 8623-8627.
- 240 S. M. Paek, E. J. Yoo, I. Honma, *Nano letters*, 2009, 9, 72-75.
- 241 A. Dhanabalan, X. Li, R. Agrawal, C. Chen, C. Wang, *Nanomaterials*, 2013, 3, 606-614.
- 242 Q. H. Wu, C. Wang, J. G. Ren, *Ionics*, 2013, 19, 1875-1882.
- 243 H. Zhang, P. Xu, Y. Ni, H. Geng, G. Zheng, B. Dong, Z. Jiaoa, *J. Mater. Res.*, 2014, 29, 617-624.
- 244 T. Gao, K. Huang, X. Qi, H. Li, L. Yang, J. Zhong, *Ceram. Int.*, 2014, 40, 6891-6897.
- 245 Q. Guo, S. Chen, X. Qin, *Mater. Lett.*, 2014, 119, 4-7.
- 246 H. Yang, Z. Hou, N. Zhou, B. He, J. Cao, Y. Kuang, *Ceram. Int.*, DOI: 10.1016/j.ceramint.2014.05.109, 2014
- 247 H. Kim, S. W. Kim, Y. U. Park, H. Gwon, D. H. Seo, Y. Kim, K. Kang, *Nano Res.*, 2010, 3, 813-821.
- 248 J. Xie, S. Y. Liu, X. F. Chen, Y. X. Zheng, W. T. Song, G. S. Cao, T. J. Zhu, X. B. Zhao, *Int. J. Electrochem. Sci.*, 2011, 6, 5539 - 5549.
- 249 B. Chen, H. Qian, J. Xu, L. Qin, Q. H. Wu, M. Zheng, Q. Dong, *J. Mater. Chem. A*, 2014, 2, 9345-9352.
- 250 Y. Li, X. Lv, J. Lu, J. Li, *J. Phys. Chem. C*, 2010, 114, 21770-21774.
- 251 M. Sathish, S. Mitani, T. Tomai, A. Unemoto, I. Honma, *J. Solid State Electrochem*, 2012 16, 1767-1774.
- 252 S. Chen, Y. Wang, H. Ahn, G. Wang, *J. Power Sources*, 2012, 216, 22-27.
- 253 X. Wang, X. Zhou, K. Yao, J. Zhang, Z. Liu, *Carbon*, 2011, 49, 133-139.
- 254 H. Liu, J. Huang, X. Li, J. Liu, Y. Zhang, K. Du, *Appl. Surf. Sci.*, 2012, 258, 4917-4921.
- 255 W. Yue, S. Yang, Y. Ren, X. Yang, *Electrochim. Acta*, 2013, 92, 412-420.
- 256 Q. Guo, Z. Zheng, H. Gao, J. Ma, X. Qin, *J. Power Sources*, 2013, 240, 149-154.
- 257 Q. Guo, X. Qin, *ECS Solid State Lett.* 2013, 2, M41-M43.

- 258 J. Zhu, G. Zhang, X. Yu, Q. Li, B. Lu, Z. Xu, *Nano Energ.*, 2014, 3, 80-87.
- 259 A. Birrozzi, R. Raccichini, F. Nobili, M. Marinaro, R. Tossici, R. Marassi, *Electrochim. Acta*, 2014, 137, 228-234.
- 260 H. Lu, N. Li, M. Zheng, L. Qiu, S. Zhang, J. Zheng, G. Ji, J. Cao, *Mater. Lett.*, 2014, 115, 125-128.
- 261 J. Guo, B. Jiang, X. Zhang, H. Liu, *J. Power Sources*, 2014, 262, 15-22.
- 262 M. Shahid, N. Yesibolati, M. C. Reuter, F. M. Ross, H. N. Alshareef, *J. Power Sources*, 2014, 263, 239-245.
- 263 N. Li, H. Song, H. Cui, C. Wang, *Electrochim. Acta*, 2014, 130, 670-678.
- 264 R. Thomas, G. M. Rao, *Electrochim. Acta*, 2014, 125, 380-385.
- 265 M. Ara, K. Wadumesthrige, T. Meng, S. O. Salleya, K. Y. Simon Ng, *RSC Adv.*, 2014, 4, 20540-20547.
- 266 X. Li, X. Meng, J. Liu, D. Geng, Y. Zhang, M. N. Banis, Y. Li, J. Yang, R. Li, X. Sun, M. Cai, M. W. Verbrugge, *Adv. Funct. Mater.* 2012, 22, 1647-1654.
- 267 B. Wang, D. Su, J. Park, H. Ahn, G. Wang, *Nanoscale Res. Lett.*, 2012, 7, 215.
- 268 Y. Jiang, Y. Xu, T. Yuan, M. Yan, *Mater. Lett.*, 2013, 91, 16-19.
- 269 B. Zhao, G. Zhang, J. Song, Y. Jiang, H. Zhuang, P. Liu, T. Fang, *Electrochim. Acta*, 2011, 56, 7340-7346.
- 270 J. Lin, Z. Peng, C. Xiang, G. Ruan, Z. Yan, D. Natelson, J. M. Tour, *ACS Nano*, 2013, 7, 6001-6006.
- 271 R. Ravikumar, S. Gopukumar, *Phys. Chem. Chem. Phys.*, 2013, 15, 3712-3717.
- 272 F. Ye, B. Zhao, R. Ran, Z. Shao, *Chem. Eur. J.*, 2014, 20, 4055-4063.
- 273 C. Xu, J. Sun, L. Gao, *Nanoscale*, 2012, 4, 5425-5430.
- 274 X. Zhu, Y. Zhu, S. Murali, M. D. Stoller, R. S. Ruoff, *J. Power Sources*, 2011, 196, 6473-6477.
- 275 X. Zhou, L. J. Wan, Y. G. Guo, *Adv. Mater.*, 2013, 25, 2152-2157.
- 276 B. P. Vinayan, S. Ramaprabhu, *J. Mater. Chem. A*, 2013, 1, 3865-3871.
- 277 C. Zhang, X. Peng, Z. Guo, C. Cai, Z. Chen, D. Wexler, S. Li, H. Liu, *Carbon*, 2012, 50, 1897-1903.
- 278 Y. Wen, F. Lei, *Adv. Mater. Res.*, 2011, 396 - 398, 2330-2333.
- 279 P. Lian, J. Wang, D. Cai, L. Ding, Q. Jia, H. Wang, *Electrochim. Acta*, 2014, 116, 103-110.
- 280 B. Zhang, Q. B. Zheng, Z. D. Huang, S. W. Oh, J. K. Kim, *Carbon*, 2011, 49, 4524-4534.
- 281 J. Cheng, H. Xin, H. Zheng, B. Wang, *J. Power Sources*, 2013, 232, 152-158.
- 282 J. Zhu, D. Wang, L. Wang, X. Lang, W. You, *Electrochim. Acta*, 2013, 91, 323-329.
- 283 P. Lian, S. Liang, X. Zhu, W. Yang, H. Wang, *Electrochim. Acta*, 2011, 58, 81-88.
- 284 S. Liu, R. Wang, M. Liu, J. Luo, X. Jin, J. Sun, L. Gao, *J. Mater. Chem. A*, 2014, 2, 4598-4604.
- 285 G. Xia, N. Li, D. Li, R. Liu, C. Wang, Q. Li, X. Lü, J. S. Spendelov, J. Zhang, G. Wu, *ACS Appl. Mater. Interfaces*, 2013, 5, 8607-8614.
- 286 H. Yang, T. Song, S. Lee, H. Han, F. Xia, A. Devadoss, W. Sigmund, U. Paik, *Electrochim. Acta*, 2013, 91, 275-281.
- 287 Q. Guo, S. Chen, X. Qin, *Mater. Lett.*, 2014, 128, 50-53.
- 288 S. Sladkevich, J. Gun, P. V. Prikhodchenko, V. Gutkin, A. A. Mikhaylov, V. M. Novotortsev, J. X. Zhu, D. Yang, H. H. Hng, Y. Y. Tay, Z. Tsakadze, O. Lev, *Nanotechnology*, 2012, 23, 485601.
- 289 G. Wang, J. Liu, S. Tang, H. Li, D. Cao, *J. Solid State Electrochem.*, 2011, 15, 2587-2592.
- 290 Baojun, H. Cao, J. Shao, G. Li, M. Qu, G. Yin, *Inorg. Chem.* 2011, 50, 1628-1632.
- 291 J. Zhu, Y. K. Sharma, Z. Zeng, X. Zhang, M. Srinivasan, S. Mhaisalkar, H. Zhang, H. H. Hng, Q. Yan, *J. Phys. Chem. C*, 2011, 115, 8400-8406.
- 292 L. Li, G. Zhou, X. Y. Shan, S. Pei, F. Li, H. M. Cheng, *J. Power Sources*, 2014, 255, 52-58
- 293 H. Sun, Y. Liu, Y. Yu, M. Ahmad, D. Nan, J. Zhu, *Electrochim. Acta*, 2014, 118, 1-9.
- 294 D. Qiu, G. Bu, B. Zhao, Z. Lin, L. Pu, L. Pan, Y. Shi, *Mater Lett.*, 2014, 119, 12-15.
- 295 F. Sun, K. Huang, X. Qi, T. Gao, Y. Liu, X. Zou, J. Zhong, *Ceram. Int.*, 2014, 40, 2523-2528.
- 296 Q. Wang, C. Y. Zhang, X. B. Xia, L. L. Xing, X. Y. Xue, *Mater Lett.*, 2013, 112, 162-164.
- 297 X. Chi, L. Chang, D. Xie, J. Zhang, G. Du, *Mater Lett.*, 2013, 106, 178-181.
- 298 P. Xue, L. Zhang, L. Zhang, X. Feng, Y. Zhang, W. Hao, H. Wang, H. Zheng, *Electrochim. Acta*, DOI: 10.1016/j.electacta.2014.05.116
- 299 B. Wang, Y. Wang, J. Park, H. Ahn, G. Wang, *J Alloy Compd.* 2011, 509, 7778-7783.
- 300 H. Kim, D. H. Seo, S. W. Kim, J. Kim, K. Kang, *Carbon*, 2011, 49, 326-332.
- 301 K. H. Kim, D. W. Jung, V. H. Pham, J. S. Chung, B. S. Kong, J. K. Lee, K. Kim, E. S. Oh, *Electrochim. Acta*, 2012, 69, 358-363.
- 302 L. Tao, J. Zai, K. Wang, H. Zhang, M. Xu, J. Shen, Y. Su, X. Qian, *J. Power Sources*, 2012, 202, 230-235.
- 303 M. Zhang, M. Jia, Y. Jin, X. Shi, *Appl. Surf. Sci.*, 2012, 263, 573-578.
- 304 C. Peng, B. Chen, Y. Qin, S. Yang, C. Li, Y. Zuo, S. Liu, J. Yang, *ACS Nano*, 2012, 6, 1074-1081.
- 305 C. Bingdi, P. Chengxin, C. Zheng, *Trans. Nonferrous Met. Soc. China*, 2012, 22, 2517-2522.
- 306 L. Pan, H. Zhao, W. Shen, X. Donga, J. Xu, *J. Mater. Chem. A*, 2013, 1, 7159-7166.
- 307 T. Hu, G. Xin, H. Sun, X. Sun, M. Yu, C. Liu, J. Lian, *RSC Adv.*, 2014, 4, 1521-1525.
- 308 R. Wang, C. Xu, J. Sun, Y. Liu, L. Gao, C. Lin, *Nanoscale*, 2013, 5, 6960-6967.
- 309 G. P. Kim, I. Nam, N. D. Kim, J. Park, S. Park, J. Yi, *Electrochem. Commun.*, 2012, 22, 93-96.
- 310 X. L. Huang, R. Wang, D. Xu, Z. Wang, H. Wang, J. Xu, Z. Wu, Q. Liu, Y. Zhang, X. Zhang, *Adv Funct Mater*, 2013, 23, 4345-53. DOI: 10.1002/adfm.201203777
- 311 A. K. Rai, J. Gim, L. T. Anh, J. Kim, *Electrochim. Acta*, 2013, 100, 63-71.
- 312 D. Li, D. Shi, Z. Chen, H. Liu, D. Jia, Z. Guo, *RSC Adv.*, 2013, 3, 5003-5008.
- 313 M. Zhang, Y. Wang, M. Jia, *Electrochim. Acta*, 2014, 129, 425-432.
- 314 Y. Qi, H. Zhang, N. Dua, D. Yanga, *J. Mater. Chem. A*, 2013, 1, 2337-2342.
- 315 F. Liu, J. Liu, Xue, Dongfeng, *Mater. Focus*, 2012, 1, 160-163.
- 316 M. Zhang, F. Yan, X. Tang, Q. Li, T. Wang, G. Cao, *J. Mater. Chem. A*, 2014, 2, 5890-5897.
- 317 L. Xing, C. Cui, C. Ma, X. Xue, *Mater Lett.*, 2011, 65, 2104-2106.
- 318 Y. Zhang, H. Liu, Z. Zhu, K. Wong, R. Mi, J. Mei, W. Lau, *Electrochim. Acta*, 2013, 108, 465-471.
- 319 L. Li, A. R. O. Raji, J. M. Tour, *Adv. Mater.*, 2013, 25, 6298-6302.
- 320 X. Li, H. Song, H. Wang, Y. Zhang, K. Du, H. Li, J. Huang, *J Appl Electrochem*, 2012, 42, 1065-1070.
- 321 A. Yu, H. W. Park, A. Davies, D. C Higgins, Z. Chen, X. Xiao, *J. Phys. Chem. Lett.*, 2011, 2, 1855-1860.
- 322 J. G. Radich, P. V. Kamat, *ACS Catal.*, 2012, 2, 807-816.

- 323 C. X. Guo, M. Wang, T. Chen, X. W. Lou, C. M. Li, *Adv. Energy Mater.*, 2011, 1, 736–741.
- 324 Y. Li, Q. Zhang, J. Zhu, X. L. Wei, P. K. Shen, *J. Mater. Chem. A*, 2014, 2, 3163–3168.
- 325 H. Wang, L. F. Cui, Y. Yang, H. S. Casalongue, J. T. Robinson, Y. Liang, Y. Cui, H. Dai, *J. Am. Chem. Soc.*, 2010, 132, 13978–13980.
- 326 S. Cheekati, Y. Xing, Y. Zhuang, H. Huang, *ECS Trans.*, 2011, 33, 23–32.
- 327 N. Lavoie, P. R. L. Malenfant, F. M. Courtel, Y. A. Lebdeh, I. J. Davidson, *J. Power Sources*, 2012, 213, 249–254.
- 328 S. K. Park, A. Jin, S. H. Yu, J. Ha, B. Jang, S. Bong, S. Woo, Y. E. Sung, Yuanzhe, *Electrochim. Acta*, 2014, 120, 452–459.
- 329 L. Li, Z. Guo, A. Du, H. Liu, *J. Mater. Chem.*, 2012, 22, 3600–3605.
- 330 C. Chen, H. Jian, X. Fu, Z. Ren, M. Yan, G. Qian, Z. Wang, *RSC Adv.*, 2014, 4, 5367–5370.
- 331 I. Nam, N. D. Kim, G. P. Kim, J. Park, J. Yi, *J. Power Sources*, 2013, 244, 56–62.
- 332 Y. J. Mai, D. Zhang, Y. Q. Qiao, C. D. Gu, X. L. Wang, J. P. Tu, *J. Power Sources*, 2012, 216, 201–207.
- 333 Y. Sun, X. Hu, W. Luo, F. Xia, Y. Huang, *Adv. Funct. Mater.*, 2013, 23, 2436–2444.
- 334 D. Qiu, L. Ma, M. Zheng, Z. Lin, B. Zhao, Z. Wen, Z. Hu, L. Pu, Y. Shi, *Mat. Lett.*, 2012, 84, 9–12.
- 335 S. Y. Liu, J. Xie, Y. X. Zheng, G. S. Cao, T. J. Zhu, X. B. Zhao, *Electrochim. Acta*, 2012, 66, 271–278.
- 336 S. L. Cheekati, Z. Yao, H. Huang, *J. Nano Mat.*, 2012, 2012, 1–10.
- 337 K. Zhang, P. Han, L. Gu, L. Zhang, Z. Liu, Q. Kong, C. Zhang, S. Dong, Z. Zhang, J. Yao, H. Xu, G. Cui, L. Chen, *ACS Appl. Mater. Interfaces*, 2012, 4, 658–664.
- 338 T. Wu, F. Tu, S. Liu, S. Zhuang, G. Jin, C. Pan, *J. Mater. Sci.*, 2014, 49, 1861–1867.
- 339 J. Zang, H. Qian, Z. Wei, Y. Cao, M. Zheng, Q. Dong, *Electrochim. Acta*, 2014, 118, 112–117.
- 340 C. T. Hsieh, C. Y. Lin, J. Y. Lin, *Electrochim. Acta*, 2011, 56, 8861–8867.
- 341 S. M. Lee, S. H. Choi, J. K. Lee, Y. C. Kang, *Electrochim. Acta*, 2014, 132, 441–447.
- 342 I. R. M. Kottegoda, N. H. Idris, L. Lu, J. Z. Wang, H. K. Liu, *Electrochim. Acta*, 2011, 56, 5815–5822.
- 343 G. Zhou, D. W. Wang, L. C. Yin, N. Li, F. Li, H. M. Cheng, *Acs Nano*, 2012, 6, 3214–3223.
- 344 S. G. Hwang, G. O. Kim, S. R. Yun, K. S. Ryu, *Electrochim. Acta*, 2012, 78, 406–411.
- 345 X. J. Zhu, J. Hu, H. L. Dai, L. Ding, L. Jiang, *Electrochim. Acta*, 2012, 64, 23–28.
- 346 Y. J. Mai, S. J. Shi, D. Zhang, Y. Lu, C. D. Gu, J. P. Tu, *J. Power Sources*, 2012, 204, 155–161.
- 347 X. Zhu, Y. Zhong, H. Zhai, Z. Yan, D. Li, *Electrochim. Acta*, 2014, 132, 364–369.
- 348 B. Li, H. Cao, J. Shao, H. Zheng, Y. Lu, J. Yin, M. Qu, *Chem. Commun.*, 2011, 47, 3159–3161.
- 349 Q. Wang, J. Zhao, W. Shan, X. Xia, L. Xing, X. Xue, *J. Alloys Compd.*, 2014, 590, 424–427.
- 350 D. Qiu, B. Zhao, Z. Lin, L. Pu, L. Pan, Y. Shi, *Mater Lett.*, 2013, 105, 242–245.
- 351 A. K. Rai, L. T. Anh, J. Gim, V. Mathew, J. Kang, B. J. Paul, N. K. Singh, J. Song, J. Kim, *J. Power Sources*, 2013, 244, 435–41.
- 352 J. Zhou, L. Ma, H. Song, B. Wu, X. Chen, *Electrochim. Commun.*, 2011, 13, 1357–1360.
- 353 X. Zhou, J. Zhang, Q. Su, J. Shi, Y. Liu, G. Du, *Electrochim. Acta*, 2014, 125, 615–621.
- 354 H. Chen, F. Feng, Z. Hu, F. Liu, W. Gong, K. Xiang, *T Nonferr Metal Soc.*, 2012, 22, 2523–2528.
- 355 S. D. Seo, D. H. Lee, J. C. Kim, G. H. Lee, D. W. Kim, *Ceram Int.*, 2013, 39, 1749–1755.
- 356 L. Q. Lu, Y. Wang, *Electrochim. Commun.*, 2012, 14, 82–85.
- 357 Y. J. Mai, X. L. Wang, J. Y. Xiang, Y. Q. Qiao, D. Zhang, C. D. Gu, J. P. Tu, *Electrochim. Acta*, 2011, 56, 2306–2311.
- 358 C. Xu, X. Wang, L. Yang, Y. Wu, *J. Solid Stat Chem.*, 2009, 182, 2486–2490.
- 359 B. Wang, X. L. Wu, C. Y. Shu, Y. G. Guo, C. R. Wang, *J. Mater. Chem.*, 2010, 20, 10661–10664.
- 360 Y. Liu, W. Wang, L. Gu, Y. Wang, Y. Ying, Y. Mao, L. Sun, X. Peng, *ACS Appl. Mater. Interfaces*, 2013, 5, 9850–9855.
- 361 N. Li, Y. Xiao, C. Hu, M. Cao, *Chem. Asian J.*, 2013, 8, 1960–1965.
- 362 Y. Zhang, X. Wang, L. Zeng, S. Song, D. Liu, *Dalton Trans.*, 2012, 41, 4316–4319.
- 363 C. Kunfeng, L. Jun, Xue, Dongfeng, *Energy Environ. Focus*, 2012, 1, 50–56.
- 364 G. Yan, X. Li, Z. Wang, H. Guo, Q. Zhang, W. Peng, *Trans. Nonferrous Met. Soc. China*, 2013, 23, 3691–3696.
- 365 Y. Sun, X. Hu, W. Luo, Y. Huang, *Acs Nano*, 2011, 5, 7100–7107.
- 366 Q. Tang, Z. Shan, L. Wang, X. Qin, *Electrochim. Acta*, 2012, 79, 148–153.
- 367 A. Bhaskar, M. Deepa, T. N. Rao, U. V. Varadaraju, *J. Power Sources*, 2012, 216, 169–178.
- 368 F. Xia, X. Hu, Y. Sun, W. Luo, Y. Huang, *Nanoscale*, 2012, 4, 4707–4711.
- 369 Q. Tang, L. Wang, K. Zhu, Z. Shan, X. Qin, *Mater Lett.*, 2013, 100, 127–129.
- 370 Y. Xu, R. Yi, B. Yuan, X. Wu, M. Dunwell, Q. Lin, L. Fei, S. Deng, P. Andersen, D. Wang, H. Luo, *J. Phys. Chem. Lett.*, 2012, 3, 309–314.
- 371 Q. Yang, Q. Liang, J. Liu, S. Liang, S. Tang, P. Lu, Y. Lu, *Mater Lett.*, 2014, 127, 32–35.
- 372 L. Noerochim, J. Z. Wang, D. Wexler, Z. Chao, H. K. Liu, *J. Power Sources*, 2013, 228, 198–205.
- 373 S. H. Choi, Y. C. Kang, *Chem Sus Chem*, 2014, 7, 523–528.
- 374 P. Lu, J. Liu, M. Lei, *Cryst Eng Comm*, 2014, DOI: 10.1039/C4CE00252K
- 375 C. L. Liu, Y. Wang, C. Zhang, X. S. Li, W. S. Dong, *Mater. Chem. Phys.*, 2014, 143, 1111–1118.
- 376 Z. X. Huang, Y. Wang, Y. Zhu, Y. Shi, J. Wong, H. Yang, *Nanoscale*, 2014, DOI: 10.1039/C4NR01744G,
- 377 A. K. Rai, J. Gim, S. W. Kang, V. Mathew, L. T. Anh, J. Kang, J. Song, B. J. Paul, J. Kim, *Mater. Chem. Phys.*, 2012, 136, 1044–1051.
- 378 H. K. Kim, S. M. Bak, K. B. Kim, *Electrochim. Commun.*, 2010, 12, 1768–1771.
- 379 Y. Shi, L. Wen, F. Li, H. M. Cheng, *J. Power Sources*, 2011, 196, 8610–8617.
- 380 H. Xiang, B. Tian, P. Lian, Z. Li, H. Wang, *J Alloy Compd.*, 2011, 509, 7205–7209.
- 381 N. Zhu, W. Liu, M. Xue, Z. Xie, D. Zhao, M. Zhang, J. Chen, T. Cao, *Electrochim. Acta*, 2010, 55, 5813–5818.
- 382 Y. Tang, F. Huang, W. Zhao, Z. Liu, D. Wan, *J. Mater. Chem.*, 2012, 22, 11257–11260.
- 383 R. Balasubramanian, E. S. Oh, J. S. Chung, *J. Power Sources*, doi:10.1016/j.jpowsour.2014.11.069.
- 384 S. Pang, Y. Zhao, C. Zhang, Q. Zhang, L. Gu, X. Zhou, G. Li, G. Cui, *Scripta Mater*, 2013, 69, 171–174.
- 385 X. Guo, H. F. Xiang, T. P. Zhou, W. H. Li, X. W. Wang, J. X. Zhou, Y. Yu, *Electrochim. Acta*, 2013, 109, 33–38.

- 386 Y. Ding, G. R. Li, C. W. Xiao, X. P. Gao, *Electrochim. Acta*, 2013, 102, 282-289.
- 387 Y. Oh, S. Nam, S. Wi, J. Kang, T. Hwang, S. Lee, H. H. Park, J. Cabana, C. Kim, B. Park, *J. Mater. Chem. A*, 2014, 2, 2023-2027.
- 388 L. Shen, C. Yuan, H. Luo, X. Zhang, S. Yang, X. Lu, *Nanoscale*, 2011, 3, 572-574.
- 389 S. G. Ri, L. Zhan, Y. Wang, L. Zhou, J. Hu, H. Liu, *Electrochim. Acta*, 2013, 109, 389-394.
- 390 H. Ni, W. L. Song, L. Z. Fan, *Electrochem. Commun.* 2014, 40, 1-4.
- 391 Q. Zhang, W. Peng, Z. Wang, X. Li, X. Xiong, H. Guo, Z. Wang, F. Wu, *Solid State Ionics*, 2013, 236, 30-36.
- 392 G. Kucinskis, G. Bajars, J. Kleperis, *J. Power Sources*, 2013, 240, 66-79.
- 393 H. Xia, Z. Luo, J. Xie, *Prog Nat Sci: Mater International*, 2012, 22, 572-584.
- 394 W. Zhang, Y. Zeng, C. Xu, N. Xiao, Y. Gao, L. J. Li, X. Chen, H. Hng, Q. Yan, *Beilstein J. Nanotechnol.*, 2012, 3, 513-523.
- 395 H. Xu, B. Cheng, Y. Wang, L. Zheng, X. Duan, L. Wang, J. Yang, Y. Qian, *Int. J. Electrochem. Sci.*, 2012, 7, 10627-10632.
- 396 X. Zhao, C. M. Hayner, H. H. Kung, *J. Mater. Chem.*, 2011, 21, 17297-17303.
- 397 K. Y. Jo, S. Y. Han, J. M. Lee, I. Y. Kim, S. Nahm, J. W. Choi, S. J. Hwang, *Electrochim. Acta*, 2013, 92, 188-196.
- 398 B. Lin, Q. Yin, H. Hu, F. Lu, H. Xia, *J. Solid State Chem.*, 2014, 209, 23-28.
- 399 S. M. Bak, K. W. Nam, C. W. Lee, K. H. Kim, H. C. Jung, X. Q. Yang, K. B. Kim, *J. Mater. Chem.*, 2011, 21, 17309-17315.
- 400 H. Zhuo, S. Wan, C. He, Q. Zhang, C. Li, D. Gui, C. Zhu, H. Niu, J. Liu, *J Power Sources*, 2014, 247, 721-728.
- 401 S. Aziz, J. Zhao, C. Cain, Y. Wang, *J Mater Sci Tech*, 2014, 30, 427-433.
- 402 B. Ju, X. Wang, C. Wu, X. Yang, H. Shu, Y. Bai, W. Wen, X. Yi, *J. Alloys Compd.*, 2014, 584, 454-460.
- 403 H. Zhao, L. Pan, S. Xing, J. Luo, J. Xu, *J. Power Sources*, 2013, 222, 21-31.
- 404 J. W. Lee, S. Y. Lim, H. M. Jeong, T. H. Hwang, J. K. Kang, J. W. Choi, *Energy Environ. Sci.*, 2012, 5, 9889-9894.
- 405 J. Cheng, B. Wang, H. L. Xin, G. Yang, H. Cai, F. Nie, H. Huang, *J. Mater. Chem. A*, 2013, 1, 10814-10820.
- 406 D. Chen, R. Yi, S. Chen, T. Xu, M. L. Gordin, D. Lv, D. Wang, *Mater. Sci. Eng B*, 2014, 185, 7-12.
- 407 D. Chen, H. Quan, S. Luo, X. Luo, F. Deng, H. Jiang, *Physica E Low Dimens Syst Nanostruct.*, 2014, 56, 231-237.
- 408 G. Du, K. H. Seng, Z. Guo, J. Liu, W. Li, D. Jia, C. Cook, Z. Liue, H. Liua, *RSC Adv.*, 2011, 1, 690-697.
- 409 X. Rui, J. Zhu, D. Sim, C. Xu, Y. Zeng, H. H. Hng, T. M. Lim, Q. Yan, *Nanoscale*, 2011, 3, 4752-4758.
- 410 S. H. Choi, Y. C. Kang, *Chem. Eur. J*, 2014, 20, 6294-6299.
- 411 H. Liu, W. Yang, *Energy Environ. Sci.*, 2011, 4, 4000-4008.
- 412 D. P. Cong, K. Ahn, S. W. Hong, S. Y. Jeong, J. H. Choi, C. H. Doh, J. S. Jin, E. D. Jeong, C. R. Cho, *Curr. Appl Phys.*, 2014, 14, 215-221.
- 413 Y. Yang, L. Li, H. Fei, Z. Peng, G. Ruan, J. M. Tour, *ACS Appl. Mater. Interfaces*, DOI: 10.1021/am501969m
- 414 Y. Shi, S. L. Chou, J. Z. Wang, H. J. Li, H. K. Liu, Y. P. Wu, *J. Power Sources*, 2013, 244, 684-9.
- 415 C. Nethravathi, B. Viswanath, J. Michael, M. Rajamath, *Carbon*, 2012, 50, 4839-4846.
- 416 C. Han, M. Yan, L. Mai, X. Tian, L. Xu, X. Xu, Q. An, Y. Zhao, X. Ma, J. Xie, *Nano Energy*, 2013, 2, 916-922.
- 417 Y. Sun, S. B. Yang, L. P. Lv, I. Lieberwirth, L. C. Zhang, C. X. Ding, C. H. Chen, *J Power Sources*, 2013, 241, 168-172.
- 418 C. Nethravathi, C. R. Rajamathi, M. Rajamathi, U. K. Gautam, X. Wang, D. Golberg, Y. Bando, *ACS Appl. Mater. Interfaces*, 2013, 5, 2708-2714.
- 419 V. S. R. Channu, D. Ravichandran, B. Rambabu, R. Holze, *Applied Surface Science*, 2014, 305, 596-602.
- 420 Y. Fu, Y. Wan, H. Xia, X. Wang, *J. Power Sources*, 2012, 213, 338-342.
- 421 M. Zhang, M. Jia, Y. Jin, Q. Wen, C. Chen, *J Alloy Compd.*, 2013, 566, 131-136.
- 422 H. Xia, D. Zhu, Y. Fu, X. Wang, *Electrochim. Acta*, 2012, 83, 166-174.
- 423 H. Xia, Y. Qian, Y. Fu, X. Wang, *Solid State Sci.*, 2013, 17, 67-71.
- 424 F. Zou, X. Hu, Y. Sun, W. Luo, Fangfang, Xia, L. Qie, Y. Jiang, Y. Huang, *Chem. Eur. J.* 2013, 19, 6027-6033.
- 425 W. T. Song, J. Xie, S. Y. Liu, Y. X. Zheng, G. S. Cao, Tie-Jun Zhu, Xin-Bing Zhao, *Int. J. Electrochem. Sci.*, 2012, 7, 2164-2174.
- 426 C. T. Hsieh, C. Y. Lin, Y. F. Chen, J. S. Lin, *Electrochim. Acta*, 2013, 111, 359-365.
- 427 G. Wang, J. Bai, Y. Wang, Z. Ren, J. Bai, *Scripta Mater.*, 2011, 65, 339-342.
- 428 P. Lian, D. Cai, K. Luo, Y. Jia, Y. Sun, H. Wang, *Electrochim. Acta*, 2013, 104, 267-273.
- 429 Y. Sun, X. Hu, W. Luo, Y. Huang, *J. Mater. Chem.*, 2011, 21, 17229-17235.
- 430 W. Song, J. Xie, W. Hu, S. Liu, G. Cao, T. Zhu, X. Zhao, *J. Power Sources*, 2013, 229, 6-11.
- 431 Y. Sun, X. Hu, W. Luo, J. Shu, Y. Huang, *J. Mater. Chem. A*, 2013, 1, 4468-4474.
- 432 Y. Zhao, Y. Huang, Q. Wang, X. Wang, M. Zong, *Ceram Int.*, 2013, 39, 1741-1747.
- 433 Y. Zhao, C. Wu, J. Li, L. Guan, *J. Mater. Chem. A*, 2013, 1, 3856-3859.
- 434 Y. Zhao, Y. Huang, Q. Wang, *Ceram Int.*, 2013, 39, 6861-6866.
- 435 C. V. Rao, A. L. M. Reddy, Y. Ishikawa, P. M. Ajayan, *ACS Appl. Mater. Interfaces*, 2011, 3, 2966-2972.
- 436 S. Yoon, K. N. Jung, S. H. Yeon, C. S. Jin, K. H. Shin, *J Electroanal. Chem.*, 2012, 683, 88-93.
- 437 M. L. Sanchez, P. Atienzar, G. Abellan, M. Puche, V. Fornes, A. Ribera, H. Garcia, *Carbon*, 2012, 50, 518-525.
- 438 Z. Yan, S. Cai, L. Miao, X. Zhou, Y. Zhao, *J Alloy Compd.*, 2012, 511, 101-106.
- 439 L. Zhang, Z. Wang, L. Wang, Y. Xing, Y. Zhang, *Mater Lett.*, 2013, 108, 9-12.
- 440 C. Guo, D. Wang, Q. Wang, B. Wang, T. Liu, *Int. J. Electrochem. Sci.*, 2012, 7, 8745-8752.
- 441 W. Yue, S. Tao, J. Fu, Z. Gao, Y. Ren, *Carbon*, 2013, 65, 97-104.
- 442 Y. Chen, J. Zhu, B. Qu, B. Lu, Z. Xu, *Nano Energ.*, 2014, 3, 88-94.
- 443 A. K. Rai, T. V. Thi, J. Gim, J. Kim, *Mater. Charact.*, 2014, 95, 259-265.
- 444 Z. Chen, Y. Yan, S. Xin, W. Li, J. Qu, Y. G. Guo, W. G. Song, *J. Mater. Chem. A*, 2013, 1, 11404-11409.
- 445 S. Jin, C. Wang, *Nano Energ.* 2014, 7, 63-71.
- 446 B. Liu, J. Zhang, X. F. Wang, G. Chen, D. Chen, C. W. Zhou and G. Z. Shen, *Nano Lett.*, 2012, 12, 3005.
- 447 J. S. Kim, Y. H. Lee, I. Lee, T. S. Kim, M. H. Ryou, J. W. Choi, *J. Mater. Chem. A*, 2014, 2, 10862-10868.
- 448 Y. Meng, H. Wu, Y. Zhang, Z. Wei, *J. Mater. Chem. A*, 2014, 2, 10842-10846.
- 449 K. M. Oh, S. W. Cho, G. O. Kim, K. S. Ryu, H. M. Jeong, *Electrochimica Acta* 135 (2014) 478-486.

- 450 H. Gwon, H. S. Kim, K. U. Lee, D. H. Seo, Y. C. Park, Y. S. Lee, B. T. Ahn, K. Kang, *Energy Environ. Sci.*, 2011, **4**, 1277-1283.
- 451 N. Li, Z. Chen, W. Ren, F. Li, H. M. Cheng, *PNAS*, 2012, 109, 17360-17365.
- 452 R. Wang, C. Xu, J. Sun, L. Gao, C. Lin, *J. Mater. Chem. A*, 2013, **1**, 1794-1800.
- 453 X. Huang, B. Sun, S. Chen, G. Wang, *Chem. Asian J.* 2014, 9, 206-211.

**Table 1** Different types of carbon nanostructures based anode materials and their performances in LIBs.

| System   | Synthesis Process  | Structural morphology   | Performance  | Ref. |
|--|--|---|--|------|
| Amorphous carbon nanotubes (ACNTs)               | Arc discharge method   | Uniform & flexible type nanotubes having length $\sim\mu\text{m}$   | ACNTs oxidized at 300 C exhibit reversible capacity $\sim 530 \text{ mAhg}^{-1}$ at $20 \text{ mAg}^{-1}$ which retain 93% after 5 cycle, whereas; ACNTs oxidized at 350 C exhibits capacity $\sim 440 \text{ mAhg}^{-1}$ after 20 cycles  | 22   |
| MWCNTs paper                                     | CVD technique  | Nearly uniformly grown nanotubes with several $\sim\mu\text{m}$ in length                                       | Reversible capacity of $\sim 330 \text{ mAhg}^{-1}$ was measured up to 10 cycles at a current density of $74 \text{ mAg}^{-1}$ whereas; at $372 \text{ mAg}^{-1}$ it delivered a reversible capacity over $225 \text{ mAhg}^{-1}$ after 10 cycles and nearly 100 % Coulombic efficiency  | 23   |
| Mesoporous Carbon/MWNTs hybrid                   | Soft template approach at low carbonization temperatures                           | Mesoporous morphology   | The specific capacity $\sim 380 \text{ mAhg}^{-1}$ at 2C after 20 cycles and $94 \text{ mAhg}^{-1}$ at 30 C after 50 cycles. However, the Coulombic efficiency of the electrode was $\sim 80\%$ only, measured up to 20 cycles. Therefore, impedes its practical applications  | 24   |
| Carbon nanotube/ carbon fibre hybrid             | CVD technique  | Carbon nanotube networks onto carbon fibre paper as the support   | Initial capacity was observed to be $643 \text{ mAhg}^{-1}$ under the constant current discharge rate $0.05 \text{ mAc m}^{-2}$ , whereas a reversible capacity of $546 \text{ mAhg}^{-1}$ and $338 \text{ mAhg}^{-1}$ was delivered at current density $0.05 \text{ mAc m}^{-2}$ and $0.05 \text{ mAc m}^{-2}$ , respectively after 50 cycles | 25   |
| MWCNTs-coated mesophase carbon microbeads hybrid | Chemical functionalization   | MWNTs having diameter of 10–20 nm covered the surface of mesophase carbon microbead, exhibited porous structure | Capacity $\sim 300 \text{ mAhg}^{-1}$ at 2.1 C rate up to 30 cycles and $\sim 160 \text{ mAhg}^{-1}$ at 7.0 C rate up to 40 cycles   | 31   |
| Activated microporous carbon                     | Carbonization phenol-melamine-formaldehyde resin, and activated by $\text{ZnCl}_2$ | Microspheres consisting of shallow concave pores  | Reversible capacity $\sim 300 \text{ mAhg}^{-1}$ at $100 \text{ mAg}^{-1}$ up to 20 cycles, $\sim 200 \text{ mAhg}^{-1}$ at $200 \text{ mAg}^{-1}$ up to 40 cycles, whereas, $\sim 100 \text{ mAhg}^{-1}$ at $300 \text{ mAg}^{-1}$ up to 60 cycles  | 32   |
| Activated nitrogen-containing carbon             | Carbonization and activation process   | Spherical particles $\sim 100 \text{ nm}$   | At a current density $100 \text{ mAg}^{-1}$ the first cycle discharged and charged capacity up to $917 \text{ mAhg}^{-1}$ and $377 \text{ mAhg}^{-1}$ , respectively. However, a reversible capacity only $\sim 251 \text{ mAhg}^{-1}$ after 20 cycles was delivered at the same current density with a Coulombic efficiency $\sim 90\%$       | 33   |
| Carbon nanofibers                                | Electrospun assisted by carbonization  | Carbon fibers, forming 3-D structures   | Specific capacity $\sim 380 \text{ mAhg}^{-1}$ at $100 \text{ mAg}^{-1}$ up to 100 cycles (with Coulombic efficiency 99 %), whereas $\sim 200 \text{ mAhg}^{-1}$ at $1 \text{ Ag}^{-1}$ up to 35 cycles. Besides, when re-cycled at $20 \text{ mAg}^{-1}$ after 40   | 34   |

| Journal Name  |  |  |   | ARTICLE |
|---|--|--|---|---------|
|   |  |  | cycles, delivered a capacity $\sim 500 \text{ mAhg}^{-1}$ compared $550 \text{ mAhg}^{-1}$ after 5 cycle  |         |
| Porous nitrogen-doped carbon vegetable-sponges          | Chemical treatment of the Cu@C precursors using $\text{HNO}_3$                         | Porous micro-vegetable-sponges like along with 3D interconnected framework   | At current density $0.5 \text{ Ag}^{-1}$ capacity was observed $\sim 870 \text{ mAhg}^{-1}$ after 300 cycles and exhibited a reversible capacity $\sim 910 \text{ mAhg}^{-1}$ at $0.2 \text{ Ag}^{-1}$ after cycled at different rate   | 35      |
| CNTs with bamboo-like structure                         | CVD technique  | Bend graphite-like sheets, form many separated cavities and resemble bamboo like structure                         | First cycle charged capacity of $710 \text{ mAhg}^{-1}$ , however very low reversible capacity of $\sim 131 \text{ mAhg}^{-1}$ during 30 cycle, suggest that electrode is not suitable for anode in LIB   | 36      |
| Carbon spheres  | via thermal decomposition of resorcinol-formaldehyde precursor                         | Carbon spheres $\sim 500 \text{ nm}$   | At current density of $0.2 \text{ mAcm}^{-2}$ initial discharge capacity $\sim 950 \text{ mAhg}^{-1}$ was observed. However, a rapid fading of capacity occurred in the second cycle, and delivered a stable capacity $\sim 350 \text{ mAhg}^{-1}$ after 135 cycles   | 37      |
| CNT film  | Vacuum filtration technique  | Thickness of film $\sim 61 \mu\text{m}$ and exhibited porous CNT network   | At a current density $100 \text{ mAg}^{-1}$ a reversible capacity was observed to be $\sim 200 \text{ mAhg}^{-1}$ up to 40 cycles and it was nearly $\sim 200 \text{ mAhg}^{-1}$ when cycled at $600 \text{ mAg}^{-1}$ up to 100 cycles   | 38      |
| Vertically aligned MWCNTs                               | Pyrolysis technique  | Vertically aligned MWCNTs consisting of $8.6 \pm 0.3 \mu\text{m}$ in length and diameter of $77 \pm 23 \text{ nm}$ | At a low currents density $57 \text{ mAg}^{-1}$ the specific capacity was observed to be $782 \text{ mAhg}^{-1}$ by 36 cycles but at high current density of $26 \text{ Ag}^{-1}$ exhibited $166 \text{ mAhg}^{-1}$   | 39      |
| Graphene sheets, expanded graphite and natural graphite | Graphene prepared by chemical method assisted by thermal and ultrasonication treatment | Graphene exhibited nearly transparent nanosheets with along with wrinkled structure                                | First cycle reversible capacities of graphene electrode were observed to be 1130 and $636 \text{ mAhg}^{-1}$ at low current densities of $0.2$ and $1 \text{ mAcm}^{-2}$ , respectively, almost twice to that of expanded graphite electrode, whereas three times to that of natural graphite electrode. However, graphene sheet delivered a reversible capacity only $\sim 400 \text{ mAhg}^{-1}$ at $1 \text{ mAcm}^{-2}$ after 30 cycles | 40      |

**Table 2:** Different types of graphene/metal nanostructured oxide hybrid and their performance in LIBs.

| System  | Synthesis Process  | Shape/size of metal oxide nanostructure | Performance   | Ref. |
|---|--|---|---|------|
| SnO <sub>2</sub> -In <sub>2</sub> O <sub>3</sub> /graphene<br>(anode)   | Solvothermal   | Particles size ~ 6 nm                   | SnO <sub>2</sub> -In <sub>2</sub> O <sub>3</sub> /graphene hybrid exhibited a storage capacity ~ 962 mAhg <sup>-1</sup> at 60 mA g <sup>-1</sup> with Coulombic efficiency ~57.2%, cycling stability (after 50 cycles capacity retention ~60.8%), and rate capability (after 25 cycles at 600 mA g <sup>-1</sup> a capacity ~ 393.25 mAh g <sup>-1</sup> ). These electrochemical properties was observed to be better than SnO <sub>2</sub> /GNS and bare SnO <sub>2</sub> -In <sub>2</sub> O <sub>3</sub> electrode | 286  |
| ZnO-SnO <sub>2</sub> /graphene<br>(anode)                               | Hydrothermal   | -----                                   | Initial discharge capacity ~ 1287.6 mAhg <sup>-1</sup> with a reversible capacity ~ 1209.4 mAhg <sup>-1</sup> at current density 1Ag <sup>-1</sup> . The charge capacity could retain ~ 1075.3 mAhg <sup>-1</sup> after 10 cycles. And even after 50 cycles, the charge capacity was retained ~ 800.9 mAhg <sup>-1</sup>  | 287  |
| SnO <sub>2</sub> /Sn/RGO<br>(anode)                                     | Peroxide induced reduction followed by thermal treatment | Particles size ~ 2.5 nm                 | After 90 cycles at current density 158 mA g <sup>-1</sup> the discharge capacity ~ 700 mAhg <sup>-1</sup> was delivered   | 288  |
| Graphene/Y <sub>2</sub> O <sub>3</sub> /LiMnO <sub>4</sub><br>(cathode) | Ex-situ synthesis approach                               | Grain size ~ 200 nm                     | An initial discharge capacity ~129.3 mAhg <sup>-1</sup> and retained 89.3% even after 500 cycles at 1 C (at an elevated temperature 55 °C). Meanwhile, at high current density 30 C capacity ~ 90.0 mAhg <sup>-1</sup> was achieved   | 402  |
| NiFe <sub>2</sub> O <sub>4</sub> /graphene<br>(anode)                   | Hydrothermal   | Particles size ~6.5 nm                  | Composite with 20% of graphene exhibited reversible capacity of ~812 mAhg <sup>-1</sup> after 50 cycles at 100 mA g <sup>-1</sup> (85% retention of the first cycle) whereas; at 1000 mA g <sup>-1</sup> delivered a reversible capacity ~ 445 mAhg <sup>-1</sup> after 40 cycles   | 420  |
| CoFe <sub>2</sub> O <sub>4</sub> -Co/RGO<br>(anode)                     | hydrothermal   | particles size of 30 nm                 | after 515 cycles the specific capacity was maintained at ~907.3 mAhg <sup>-1</sup> at 100 mA g <sup>-1</sup> and even after 420 cycles at 9000 mA g <sup>-1</sup> , the capacity was still retained 907.3 mAhg <sup>-1</sup> when recycled at 100 mA g <sup>-1</sup>  | 421  |
| CoFe <sub>2</sub> O <sub>4</sub> /graphene<br>(anode)                   | hydrothermal   | particles size ~10 nm                   | With 20 wt% of graphene the composite electrode exhibited a reversible specific capacity of 910 mAhg <sup>-1</sup> at 100 mA g <sup>-1</sup> , and ~500 mAhg <sup>-1</sup> at 2000 mA g <sup>-1</sup> after 50 cycles, respectively   | 422  |
| ZnFe <sub>2</sub> O <sub>4</sub> /Graphene<br>(anode)                   | hydrothermal   | particles size of 20-30 nm              | At a current density of 100 mA g <sup>-1</sup> a reversible capacity ~1000 mAhg <sup>-1</sup> by 10 <sup>th</sup> cycle whereas; at 1000 mA g <sup>-1</sup> , hybrid electrode could deliver a reversible capacity of ~ 600 mAhg <sup>-1</sup> even after 40 cycles (much higher than that of pure  | 423  |

| Journal Name   |  |  | ARTICLE  |     |
|--|--|--|--|-----|
|  |  |  | ZnFe <sub>2</sub> O <sub>4</sub> electrode (~185 mAhg <sup>-1</sup> )  |     |
| Zn <sub>2</sub> GeO <sub>4</sub> /N-doped graphene ( <b>anode</b> )                              | Hydrothermal assisted by microwave                                   | Nanorods (~100 nm diameter and micrometer in length) | The capacity of 1463 mAhg <sup>-1</sup> and 531 mAhg <sup>-1</sup> at current density of 100 mA g <sup>-1</sup> and 3200 mA g <sup>-1</sup> , respectively, along with good cyclability and columbic efficiency ~ 100 %  | 424 |
| ZnO/graphene ( <b>anode</b> )  | Hydrothermal   | Quasi-spherical with particles size of 30-40 nm      | At 50 mA g <sup>-1</sup> , ZnO/graphene hybrid electrode delivered a capacity ~ 300 mAhg <sup>-1</sup> after 25 cycles (however; only ~ 75 % of first cycled capacity was retained)  | 425 |
| ZnO@Graphene ( <b>anode</b> )  | Microwave  | Particle size 80–100 nm                              | Reversible capacity 460 mAhg <sup>-1</sup> at 1 C after 50 cycles. Coulombic efficiency ~ 82.1% at 1st cycle, capacity retention ~ 60% at 5 C, and good cycling stability with capacity decay ~ 8% after 50 cycles   | 426 |
| CeO <sub>2</sub> -graphene ( <b>anode</b> )  | Hydrothermal   | Particles size ~ 100 nm                              | After 100 cycles, specific capacity ~ 605 mAhg <sup>-1</sup> at 50 mA g <sup>-1</sup> (~ 75 % of first cycled capacity) whereas; at current densities of 100, 200, 400 and 800 mA g <sup>-1</sup> , specific capacities was observed to be 414, 320, 222 and 146 mAhg <sup>-1</sup> , respectively   | 427 |
| (Fe <sub>2.5</sub> Ti <sub>0.5</sub> ) <sub>1.04</sub> O <sub>4</sub> /graphene ( <b>anode</b> ) | Gas/liquid interface   | Particles size ~20 nm                                | After 60 cycles, at current density of 300 mA g <sup>-1</sup> the reversible specific capacity of 1048 mAhg <sup>-1</sup> , whereas at 2000 mA g <sup>-1</sup> , the reversible specific capacity was observed to as high as 480 mAhg <sup>-1</sup> and exhibit good cyclic stability (at 300 mA g <sup>-1</sup> capacity ~ 1113 mAhg <sup>-1</sup> after 100 cycles). Initial Coulombic efficiency of the hybrid was 61% but after 3 <sup>rd</sup> cycles the Coulombic efficiency was increased above 94% in the subsequent cycles | 428 |
| Mn <sub>2</sub> Mo <sub>3</sub> O <sub>8</sub> /graphene ( <b>anodes</b> )                       | Chemical reduction using hydrazine assisted by annealing             | Microspheres of 3 – 5 μm                             | After 40 cycles at current density 200 mA g <sup>-1</sup> a reversible capacity ~950 mAhg <sup>-1</sup> with a Coulombic efficiency of ~ 98%. (much higher than that of bare Mn <sub>2</sub> Mo <sub>3</sub> O <sub>8</sub> ~ 494 mAhg <sup>-1</sup> ) whereas; at 1000 mA g <sup>-1</sup> a reversible capacity ~ 900 mAhg <sup>-1</sup>  | 429 |
| Zn <sub>2</sub> SnO <sub>4</sub> /graphene ( <b>anode</b> )                                      | Hydrothermal   | Quasi-sphere shape size of 10-20 nm                  | Charge capacity ~ 688 mAhg <sup>-1</sup> could retain after 50 cycles at 200 mA g <sup>-1</sup> , and after being cycled for 40 cycles at 800 mA g <sup>-1</sup> a charge capacity > 500 mAhg <sup>-1</sup> was observed. However, the capacity of Zn <sub>2</sub> SnO <sub>4</sub> /G hybrid exhibited fluctuation with cycling   | 430 |
| Fe <sub>2</sub> Mo <sub>3</sub> O <sub>8</sub> -RGO ( <b>anode</b> )                             | Chemical reduction using hydrazine and assisted by annealing process | Particles size of 10 – 15 nm                         | Up to 40 cycles a specific capacity of 835 mAhg <sup>-1</sup> at 200 mA g <sup>-1</sup> whereas; the specific capacity ~ 574.8 mAhg <sup>-1</sup> at 3000 mA g <sup>-1</sup> (bare Fe <sub>2</sub> Mo <sub>3</sub> O <sub>8</sub> exhibited poor capacity ~ 100 mAhg <sup>-1</sup> at 200 mA g <sup>-1</sup> after 20 cycles   | 431 |

| Journal Name   |   |                                    |              | ARTICLE  |     |
|--|---|------------------------------------|--------------|--|-----|
| Carbon-doped<br>Li <sub>2</sub> SnO <sub>3</sub> /graphene<br>( <b>anode</b> )                           | Hydrothermal                                | Particles size of                  | ~200 nm      | Up to 50 cycles, specific capacity of 622.7 mAhg <sup>-1</sup> , 569.7 mAhg <sup>-1</sup> and 518.4 mAhg <sup>-1</sup> at current density of 180 mA g <sup>-1</sup> (0.3 C), 300 mA g <sup>-1</sup> (0.5 C) and 600 mA g <sup>-1</sup> (1 C), respectively   | 432 |
| Li <sub>2</sub> MnSiO <sub>4</sub> /carbon/<br>graphene ( <b>cathode</b> )                               | Solid-state method                          | Particles with size of 20 to 60 nm |              | At 0.05 C, capacity of 290 mAhg <sup>-1</sup> but at 1 C (166 mA g <sup>-1</sup> ), capacity of 150 mAhg <sup>-1</sup> along with nearly stable cycling life up to 700 cycles.   | 433 |
| Poly-pyrrole(PPY)/<br>Li <sub>2</sub> SnO <sub>3</sub> /graphene<br>( <b>anode</b> )                     | De-oxidation approach                       | Particles 30-50 nm                 |              | At 60 mA g <sup>-1</sup> the reversible capacity of ~ 699.4 mAhg <sup>-1</sup> at the 30th cycle along with 95% Coulombic efficiency whereas; at 300 mA g <sup>-1</sup> and 600 mA g <sup>-1</sup> a reversible capacity ~ 493 mAhg <sup>-1</sup> and ~ 377.9 mAhg <sup>-1</sup>   | 434 |
| LiNi <sub>1/3</sub> Co <sub>1/3</sub> Mn <sub>1/3</sub> O <sub>2</sub> /<br>graphene ( <b>cathode</b> )  | Ball-milling                                | Particles size of                  | 220 - 280 nm | At 0.05 C charge/discharge, capacities of 188/185 mAhg <sup>-1</sup> , during 25 cycles. Moreover, hybrid exhibited significantly higher columbic efficiency (99.1 %) compare to bare LiNi <sub>1/3</sub> Co <sub>1/3</sub> Mn <sub>1/3</sub> O <sub>2</sub> (89.7 %)  | 435 |
| LiNi <sub>0.8</sub> Co <sub>0.15</sub> A <sub>0.05</sub> O <sub>2</sub> /<br>graphene ( <b>cathode</b> ) | Ball milling                                | Particles size                     | ~500 nm      | At 0.2 C (1 C = 278 mA g <sup>-1</sup> ) capacity of 180 mAhg <sup>-1</sup> (with 97% retention after 80 cycles) whereas; at 10 C and 20 C, capacity ~ 152 and 112 mAhg <sup>-1</sup> , respectively   | 436 |
| Ni <sub>6</sub> MnO <sub>8</sub> /graphene<br>( <b>anode</b> )   | Co-precipitation<br>assisted by calcination | Particles size                     | 20 nm        | First cycle discharge capacity of 1030 mAhg <sup>-1</sup> at current density 50 mA g <sup>-1</sup> , however, this hybrid delivered capacity ~ 400 mAhg <sup>-1</sup> only, at a rate of 50 mA g <sup>-1</sup> after 10 cycles. Moreover, this hybrid exhibited poor cyclic stability  | 437 |
| Li <sub>2</sub> FeSiO <sub>4</sub> /C<br>(resembled graphene)<br>( <b>cathode</b> )                      | Sol-gel                                     | Particles size                     | 50-150 nm    | Discharge capacity of 135.3mAhg <sup>-1</sup> at current C/16 after 40 cycles, whereas ~ 100 mAhg <sup>-1</sup> at current rate of C/1 up to 30 cycles   | 438 |
| ZnWO <sub>4</sub> /graphene<br>( <b>anode</b> )  | Sol-gel                                     | -----                              |              | At 50mA g <sup>-1</sup> after 20 cycle a reversible specific capacity of 585.7 mAhg <sup>-1</sup> whereas, at 200 mA g <sup>-1</sup> capacity ~ 480 mAhg <sup>-1</sup> was observed. However, hybrid did not exhibit proper cyclic stability and therefore, may restrict its practical application in LIBs                       | 439 |
| SiO <sub>2</sub> /graphene ( <b>anode</b> )  | Chemical reduction by hydrazine             | Particle size                      | 50-300 nm    | When current density back to the initial 100 mA h g <sup>-1</sup> after 50 cycles reversible specific capacity 910 mAhg <sup>-1</sup> was observed. In addition, at current density of 200, 400 and 800 mA g <sup>-1</sup> , this hybrid could deliver reversible capacity of 890, 701 and 441 mAhg <sup>-1</sup> , respectively | 440 |
| Carbon-  | Hydrothermal                                | particles size                     | 5–10 nm      | Carbon-coated graphene–Cr <sub>2</sub> O <sub>3</sub> hybrid   |     |

| Journal Name  |              |  | ARTICLE  |
|---|--------------|--|--|
| coated graphene–Cr <sub>2</sub> O <sub>3</sub><br>(anode) |              |  | exhibited a reversible capacity up to 630 at 0.1 C after 100 cycles and 315 mAhg <sup>-1</sup> could remain at 1 C by 25 cycles which was better than that of graphene–Cr <sub>2</sub> O <sub>3</sub> hybrid electrode 441   |
| NiCo <sub>2</sub> O <sub>4</sub> /graphene<br>(anode)     | Hydrothermal | NiCo <sub>2</sub> O <sub>4</sub> consist of nanosheet sheets | At a current density 300mA g <sup>-1</sup> , the discharge capacity maintained around 806mAhg <sup>-1</sup> up to 90 cycles (in contrast bare NiCo <sub>2</sub> O <sub>4</sub> delivered ~ 600 mAhg <sup>-1</sup> by 50 cycles) whereas, ~ 1000 mAhg <sup>-1</sup> when cycled at 150 mA g <sup>-1</sup> by 30 cycles 442  |
| MgFe <sub>2</sub> O <sub>4</sub> /graphene<br>(anode)     | Sol-gel      | Particle size ~50–100 nm                                     | At 0.34 C capacity ~ 600 mAhg <sup>-1</sup> by 15 cycles whereas, at 4.2C a reversible capacity ~ 219.9 mAhg <sup>-1</sup> after 40 cycles and columbic efficiency ~ 95 % when cycles at 0.04 C up to 60 cycles 443  |
| CuGeO <sub>3</sub> /grapheme<br>(anode)                   | Hydrothermal | Nanowires having length of several micrometer                | Reversible capacities of 1428, 1242, 1092, 958 and 879 mA hg <sup>-1</sup> at current densities of 100, 200, 400, 800, and 1000 mA g <sup>-1</sup> , respectively. Moreover, the specific capacity was increased to 1600 mAhg <sup>-1</sup> when the current densities decreased from 1000 to 100 mA g <sup>-1</sup> , even higher than the specific capacity observed in the in the initial 10 cycles 444 |
| Fe <sub>2</sub> GeO <sub>4</sub> /RGO<br>(anode)          | Hydrothermal | Particle size 10 – 20 nm                                     | At current density 0.4, 1.6, 3.2, and 4.8 Ag <sup>-1</sup> , the corresponding capacities were 980, 600, 450, and 340 mAhg <sup>-1</sup> with a Coulombic efficiency of ~ 98%. In addition, when current density was returned to 0.4Ag <sup>-1</sup> , a capacity of 990 mAhg <sup>-1</sup> was recorded, suggesting good rate capability 445  |

## Figure captions

- Fig. 1** Schematic representation of LIB.
- Fig. 2** Basis of all graphitic forms. Graphene is a 2D building material for carbon materials of all other dimensionalities. It can be wrapped up into 0D buckyballs, rolled into 1D nanotubes, or stacked into 3D graphite.<sup>29</sup>
- Fig. 3** Schematic of the formation process for the ordered mesoporous graphene nanosheets.<sup>133</sup>
- Fig. 4** SEM images and schematic (bottom inset) of the mesoporous graphene nanosheets before removal of the AAO template. The remaining regular channels of the membranes are observed. Mesopores grown on the surface of the macroporous channels are ordered on the large domain to form carbon layers several nanometers thick (top inset). **(b)** SEM images and schematic (inset) of the mesoporous graphene nanosheets after removal of the AAO template. The nanosheet-like morphology grows along the prime AAO channels. **(c)** SEM images and schematic (inset) of the mesoporous graphene nanosheets observed along the nanosheets. **(d)** SEM images observed perpendicular to the side walls of the nanosheets. The white arrows indicate that the ultrathin nanosheets are composed of single layers of ordered mesopores.<sup>133</sup>
- Fig. 5** First and second cycles of galvanostatic discharge/charge curves of the mesoporous graphene nanosheets. **(b)** Cycling performance (red curve, discharge; black curve, charge) and the Coulombic efficiency (blue curve) of the mesoporous graphene nanosheets at different current densities. Each current density is labeled over the corresponding cycles.<sup>133</sup>
- Fig. 6** **(a)** Schematic illustration of the pillared CNT and graphene nanostructure on copper foil. **(b)** Photograph of centimeter-scale PGN on copper foil. **(c)** Tilted-view SEM image showing both PGN regions and graphene regions at the same location. **(d)** Top-view SEM images of graphene and **(e)** pillared CNT regions. **(f)** High-magnification and **(g)** low-magnification cross-section SEM observation of the PGN. **(h)** High resolution TEM image of as-grown CNTs.<sup>161</sup>
- Fig. 7** Galvanostatic charge–discharge profiles of **(a)** PGN electrode at a low current density of 100 mA g<sup>-1</sup> and **(b)** PGN electrode under a range of current densities from 100 mA g<sup>-1</sup> to 900 mA g<sup>-1</sup>. **(c)** Cycling performance and Coulombic efficiency of the PGN electrode at a current density of 600 mA g<sup>-1</sup>. **(d)** High-rate cycling performance of the LIB with PGN anode.<sup>161</sup>
- Fig. 8** Characterization of A-TO/GSP. **(a)** Photograph of a bent flexible A-TO/GSP. **(b and c)** Cross-sectional SEM images of the A-TO/GSP. **(d)** High magnification SEM image of LTO nanosheets in A-TO/GSP. **(e)** TEM image of the A-TO/GSP. **(f)** HRTEM image of a TiO<sub>2</sub> nanosheet showing lattice fringes with a spacing of 0.19 nm. The lithium diffusion channels are clearly shown to be along [001] (perpendicular to the figure facet).<sup>177</sup>
- Fig. 9** **(a)** Galvanostatic discharge–charge voltage profiles of A-TO/GSP cycled at different rates. Comparison of the **(b)** specific capacity at different rates and **(c)** cycling performance at 10 C between the A-TO/GSP and I-TO/GSP electrodes.<sup>177</sup>
- Fig. 10** Schematic diagram of the sample structure. **(a)** Graphene foam backbone. **(b)** Graphene foam coated with ZnO using atomic layer deposition (GF@ZnO). **(c)** Graphene foam supported Fe<sub>3</sub>O<sub>4</sub> nanostructure electrodes (GF@Fe<sub>3</sub>O<sub>4</sub>).<sup>216</sup>
- Fig. 11** Electrochemical properties of the GF@Fe<sub>3</sub>O<sub>4</sub> LIB electrodes. **(a)** CV curves of the GF@Fe<sub>3</sub>O<sub>4</sub> electrode. **(b)** Discharge–charge voltage capacity profiles of the GF@Fe<sub>3</sub>O<sub>4</sub> electrode at 1C rate. **(c)** Cycling profiles of the GF and GF@Fe<sub>3</sub>O<sub>4</sub> electrodes at 1C rate.<sup>216</sup>
- Fig. 12** Cycle performance of the prepared electrodes: **(a)** the NGr-I, NGr-I-2ALD, and NGr-I-M-2ALD electrodes when performing full discharge-charge at 2 Ag<sup>-1</sup> for 200 cycles. **(b)** Capacity performance of the NGr-I-M-2ALD at an extremely high current rate of 20 Ag<sup>-1</sup> for 2000 cycles. (A color version of this figure can be viewed online).<sup>226</sup>
- Fig. 13** Electrochemical performance of the GNRs/SnO<sub>2</sub> electrodes. The specific capacities are calculated based on the total mass of the GNRs/SnO<sub>2</sub> in the anode electrodes. **(a)** CV curves of the first, second, and third cycles of the hybrid electrodes at a scan rate of 0.5 mV/s over the voltage range of 0.01–2.5 V. **(b)** The first, second and 30th charge/discharge curves of the hybrid electrode at a rate of 100 mA/g. **(c)** Comparison of capacity retention and Coulombic efficiency of GNRs and the GNRs/SnO<sub>2</sub> electrode at a rate of 100 mA/g. **(d)** Rate capability of the hybrid electrodes with various current densities.<sup>270</sup>
- Fig. 14** **(a)** Schematic diagram showing the wrapping up of the GO nanosheets on the Co<sub>3</sub>O<sub>4</sub> nanoparticles; and **(b)** the fabrication of the GO–Co<sub>3</sub>O<sub>4</sub> hybrid film by a direct ESD process on Cu foils. The optical image shows a uniform coating of the ESD deposited hybrid film.<sup>307</sup>
- Fig. 15** Electrochemical performance of the G–Co<sub>3</sub>O<sub>4</sub> hybrid electrode: **(a)** cyclic voltammograms of the G–Co<sub>3</sub>O<sub>4</sub> electrode at a scan rate of 0.5 mVs<sup>-1</sup> for three cycles between 0.01 and 3.0 V vs. Li+/Li; **(b)** charge and discharge curves after the first and 10th cycles at a current rate of 100 mA g<sup>-1</sup>; **(c)** cycling performance at different rates from 100 mA g<sup>-1</sup> to 5 Ag<sup>-1</sup>; and **(d)** capacity and Coulombic efficiency at 1 Ag<sup>-1</sup>.<sup>307</sup>
- Fig. 16** SEM micrographs with different magnifications **(A–C)** and TEM images **(D and E)** of the 3D PG–1Mn hybrid and HRTEM images **(F and its inset)** of the MnO<sub>2</sub> nanoflakes. **(H)** The walls of the 3D PG–1Mn hybrid and HRTEM images **(I and its inset)** of the MnO<sub>2</sub> nanoflakes. **(J and its inset)** HRTEM image of the interface between the MnO<sub>2</sub> and few-layer graphene-like materials of 3D PG.<sup>324</sup>
- Fig. 17** Electrochemical performances of various anode materials. **(A)** Typical CV curves of the 3D PG–1Mn hybrid anode at a scan rate of 0.1 mVs<sup>-1</sup>, **(B)** the galvanostatic discharge–charge profiles of the 3D PG–1Mn hybrid electrode

between 0.01 and 3 V at a current density of 100 mA $g^{-1}$ , (C) the cycling performance at a current density of 100 mA $g^{-1}$  and (D) the specific capacity versus current densities for the 3D PG-xMn composite electrodes.<sup>324</sup>

**Fig. 18** (a) Cyclic stability at a current density of 100 mA $g^{-1}$ , (b) rate capability and (c) EIS results of NiO and NiO-graphene hybrid electrodes.<sup>346</sup>

**Fig. 19** TEM images of Cu<sub>2</sub>O-GNS (a, b) and bare Cu<sub>2</sub>O spheres (c, d).<sup>361</sup>

**Fig. 20** Electrochemical characterizations of Cu<sub>2</sub>O-GNS and bare Cu<sub>2</sub>O NPs. Charge and discharge curves of (a) Cu<sub>2</sub>O-GNS, (b) bare Cu<sub>2</sub>O NPs, and (c) Cu<sub>2</sub>O NPs-GNS for the 1st (red line), 5th (blue line), 10th (green line) cycles at a current density of 100 mA $g^{-1}$ . (d) Capacity retentions of the as-obtained samples at various current densities (Cu<sub>2</sub>O-GNS: blue line; Cu<sub>2</sub>O NPs-GNS: red line; bare Cu<sub>2</sub>O sphere purple line).<sup>361</sup>

**Fig. 21** (a) Galvanostatic discharge/charge curves of the MoO<sub>2</sub>/Graphene hybrid electrode at a current density 540 mA $g^{-1}$  in the voltage range of 0.01-3.0 V, (b) the cycling performance of the MoO<sub>2</sub>/graphene at current density of 540 mA $g^{-1}$ ; (c) rate performance of the MoO<sub>2</sub>/graphene hybrid, and (d) the cycling performance of MoO<sub>2</sub>/graphene, neat MoO<sub>2</sub>, and neat graphene electrodes at different current densities.<sup>367</sup>

**Fig. 22** (a) Galvanostatic charge/discharge profiles of LTO/graphene-IL electrode during 1st, 2nd, 50<sup>th</sup>, and 100th cycles at 0.5 C. (b) cyclic performance of LTO, LTO/graphene, and LTO/graphene-IL electrodes at 0.5 C. (c) high-rate performance of LTO, LTO/graphene, and

LTO/graphene-IL electrodes. (d) high rate performance of LTO/graphene-IL electrode.<sup>389</sup>

**Fig. 23** Initial charge-discharge curves (a) and cycling stability curves (b) for the LIB cells made from the LiMn<sub>2</sub>O<sub>4</sub> *in-situ* coated with graphene-like membrane compared to the pristine membrane.<sup>400</sup>

**Fig. 24** Synthesis scheme and microscopic images of the fabricated GNR-V<sub>2</sub>O<sub>5</sub> NP hybrid. The composition of V<sub>2</sub>O<sub>5</sub> entrapped in or on the GNRs could be tailored from 25, 40, and 60 wt%, and these are designated as GNR25VO, GNR40VO, and GNR60VO, respectively. (a) schematic diagram of the fabrication process. (b) SEM and (c) TEM images of GNR25VO. (d) SEM and (e) TEM images of GNR40VO. (f) SEM and (g) TEM images of GNR60VO.<sup>413</sup>

**Fig. 25** Rate performance and cyclability of the hybrid electrode. (a) variation in the capacity of the hybrid with different applied current densities from 0.1 to 2 C. (b) discharge/charge profiles of the GNR40VO at different current densities from 0.1 to 2 C. (c) 100 discharge/charge cycle testing of the composites at 0.1 C. (d) EIS of the hybrid electrode.<sup>413</sup>

**Fig. 26** (a) Assembled flexible Li battery based on graphene paper. V<sub>2</sub>O<sub>5</sub>/graphene paper and electrochemically lithiated-graphene paper were used as cathode and anode, respectively, which were separated by a separator dipped in liquid electrolyte. (b) The battery is thin, lightweight, and flexible enough to be rolled up or twisted. (c) Schematic drawing of the flexible Li battery based on graphene paper.<sup>450</sup>

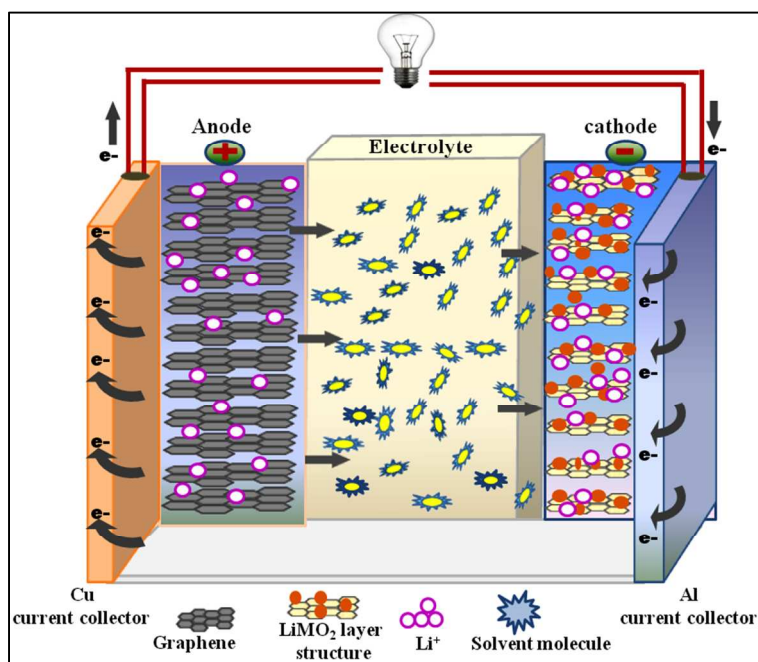


Fig. 1

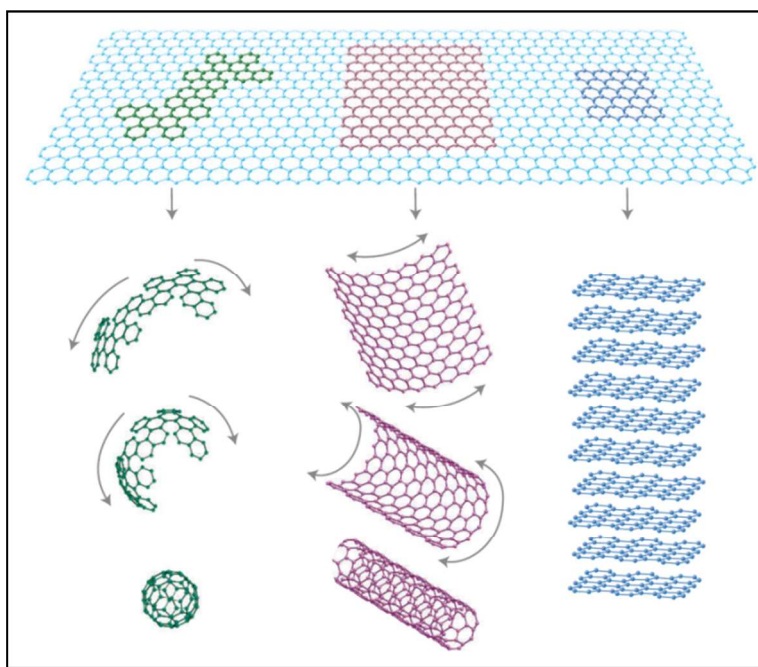


Fig. 2

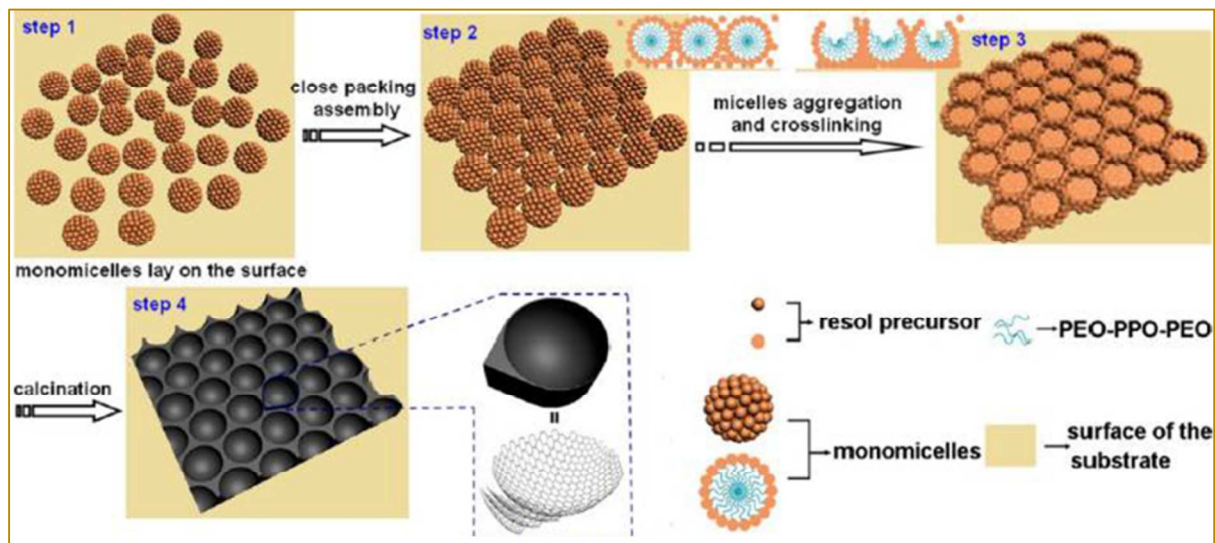


Fig. 3

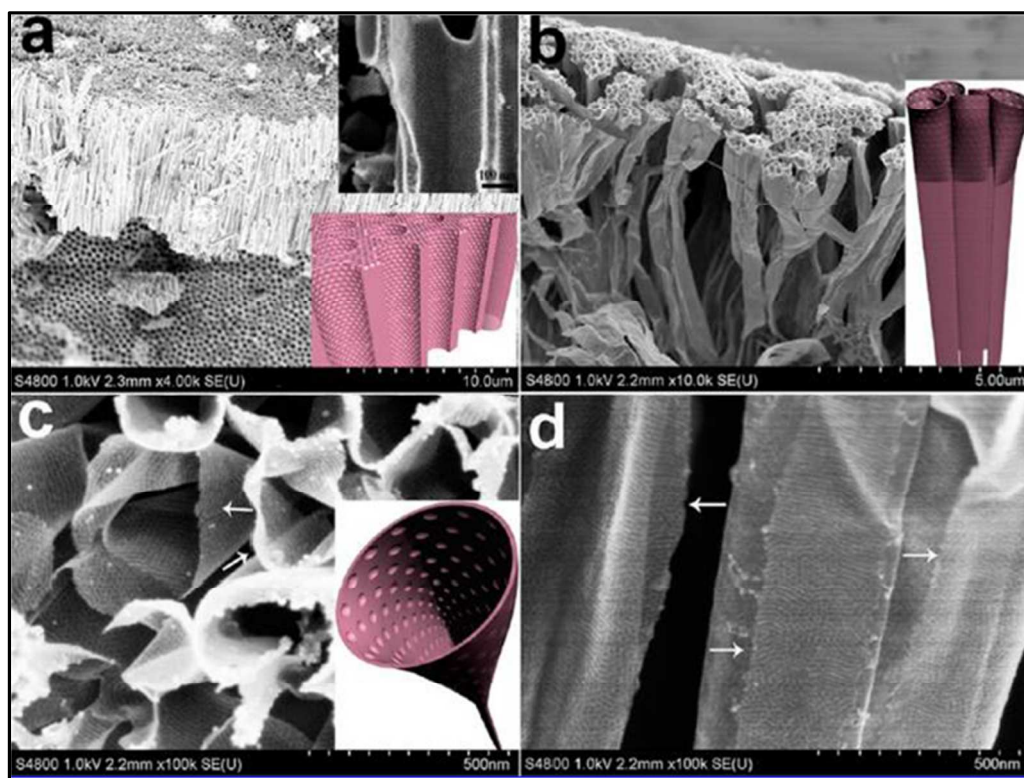


Fig. 4

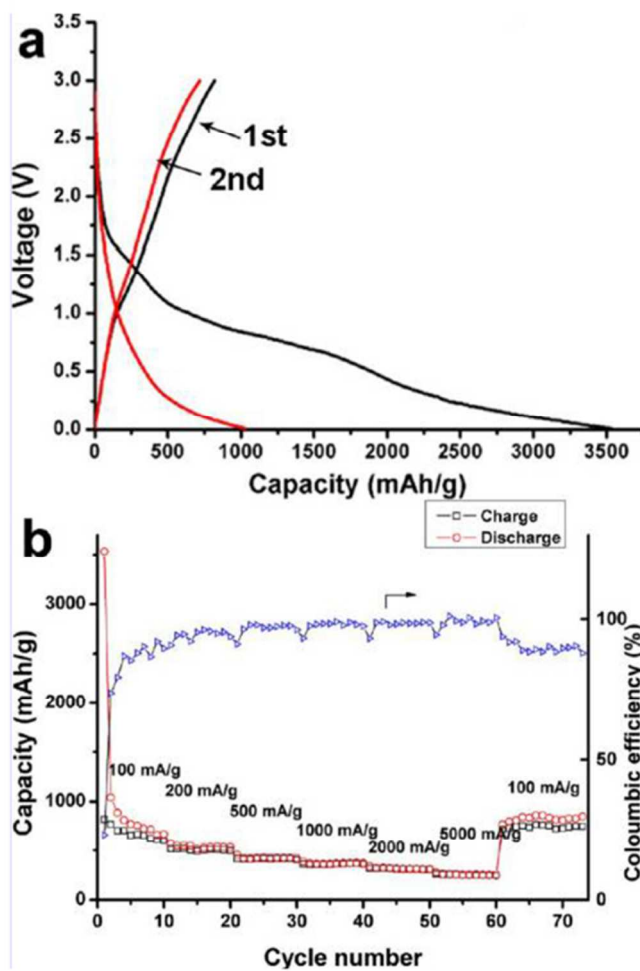


Fig. 5

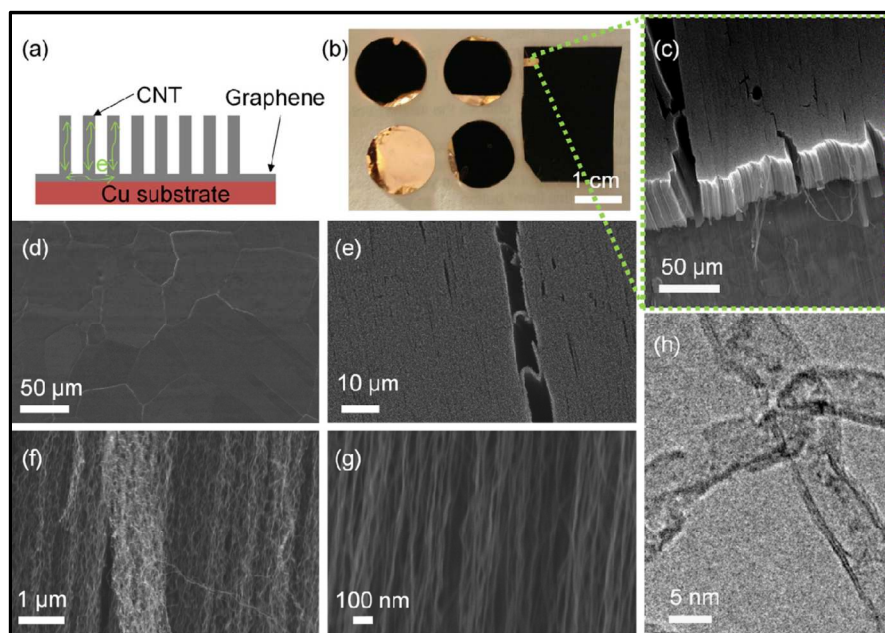


Fig. 6

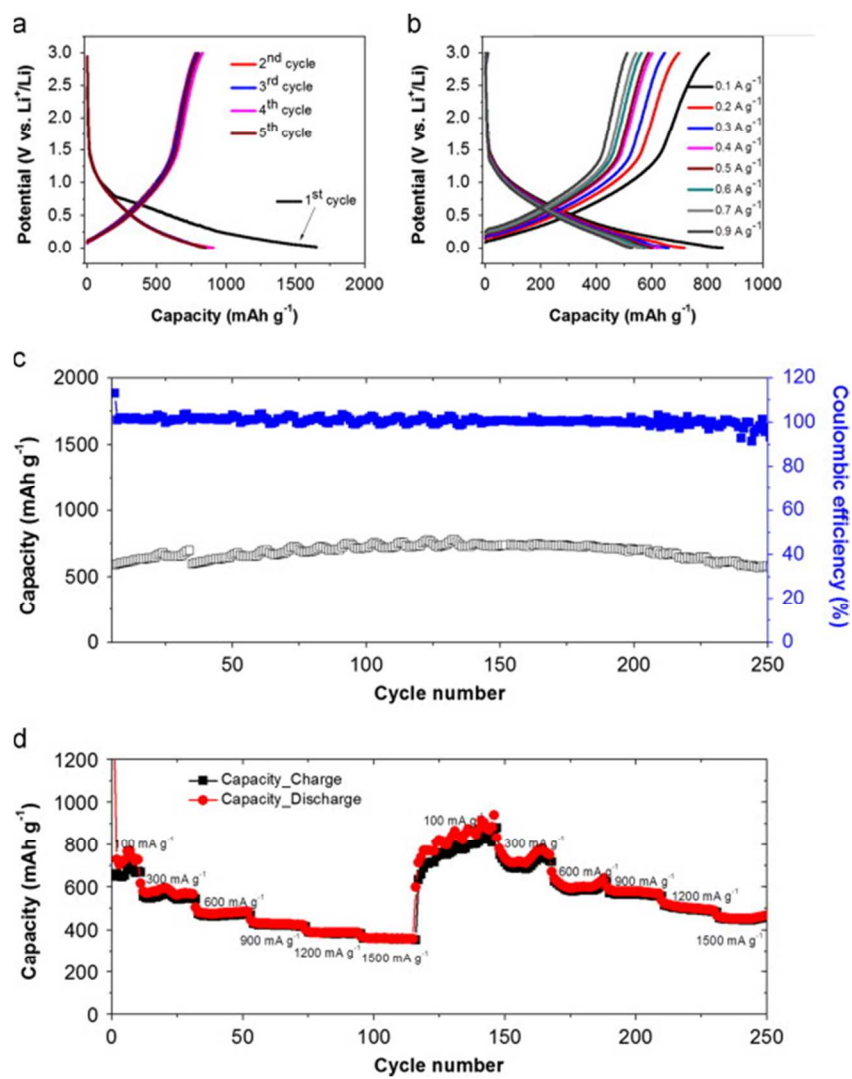


Fig. 7

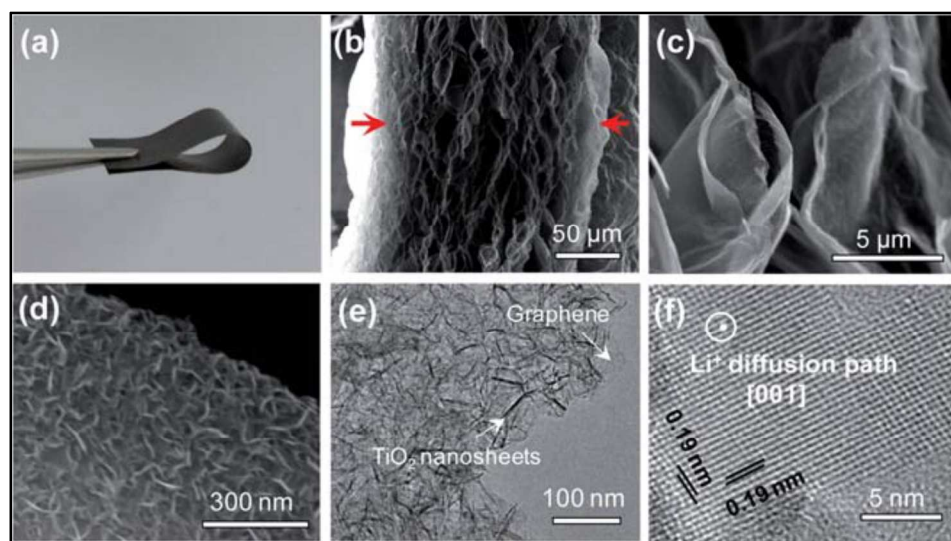


Fig. 8

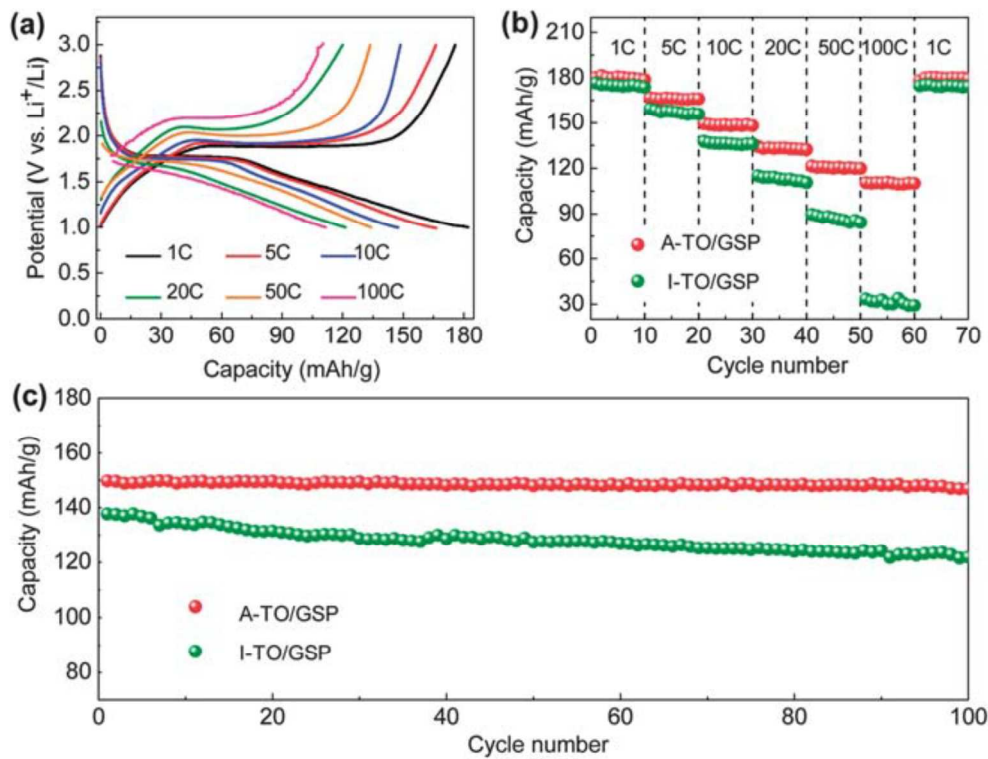


Fig. 9

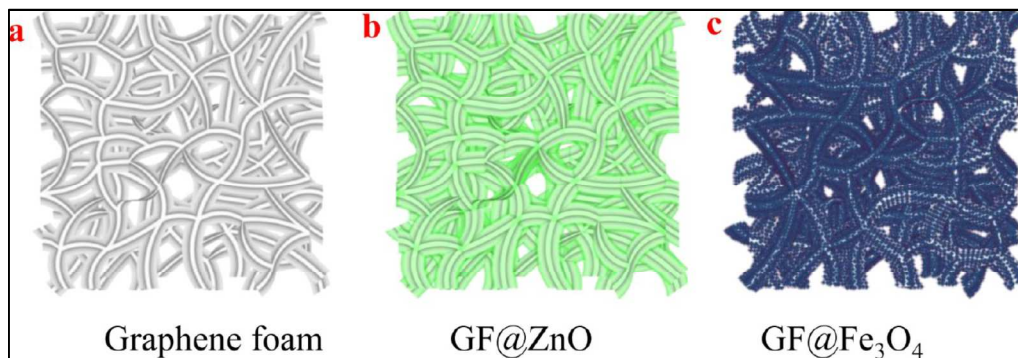


Fig. 10

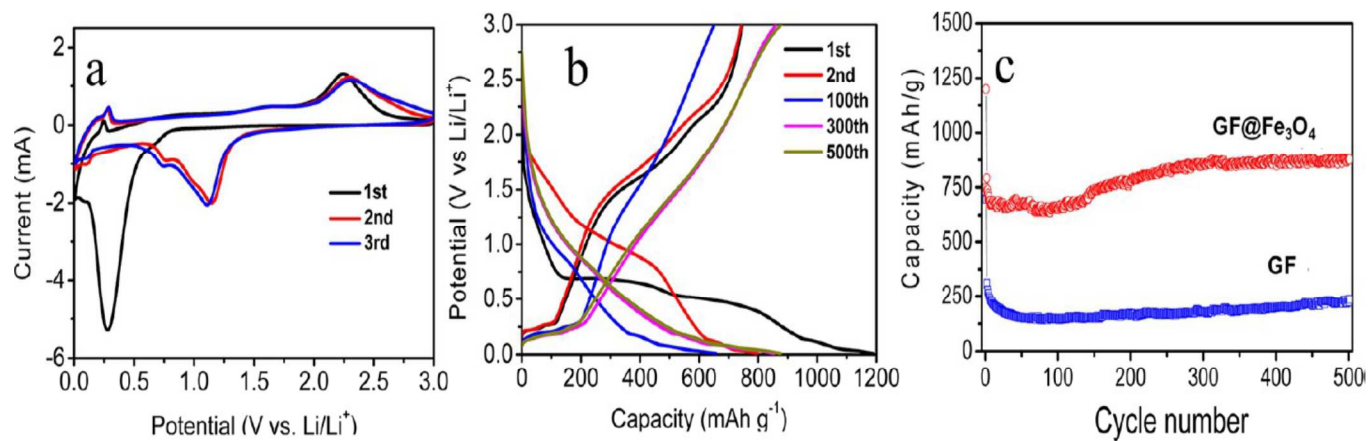


Fig. 11

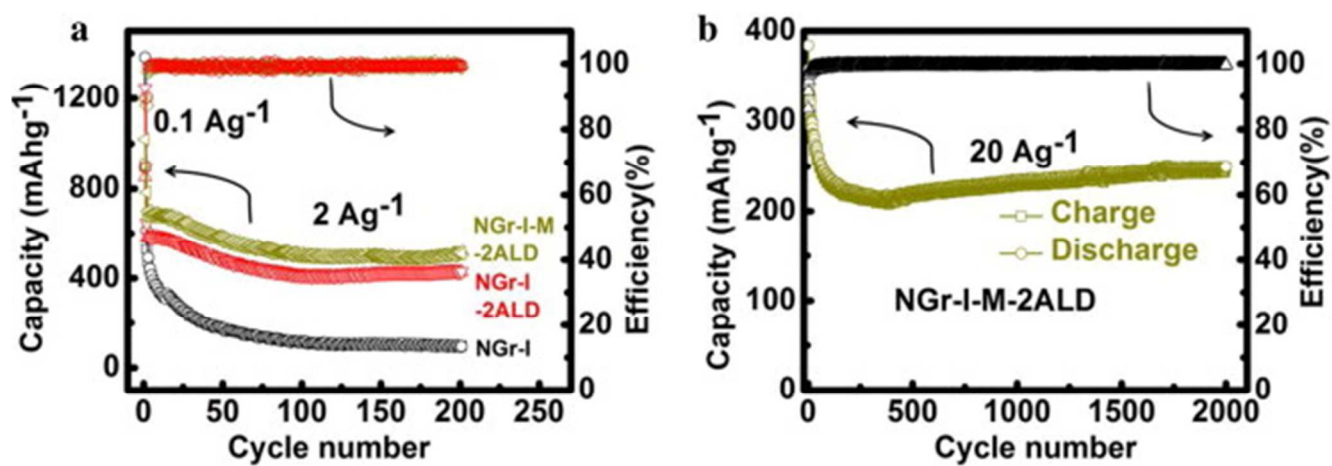


Fig. 12

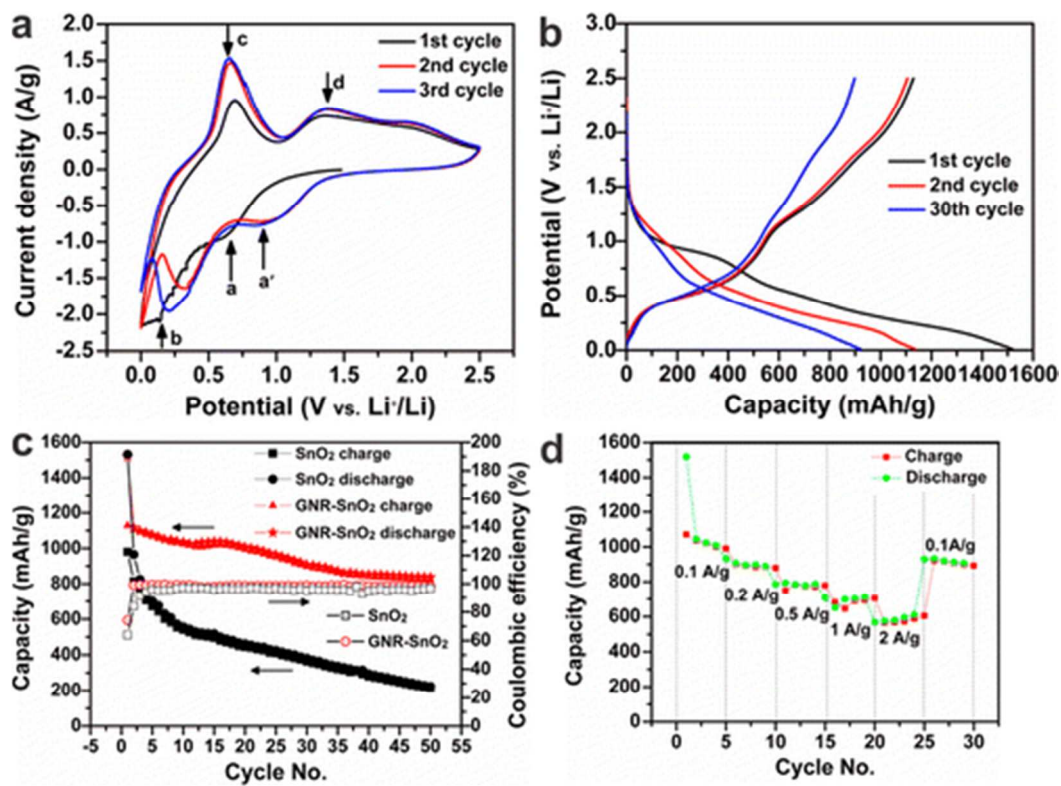


Fig. 13

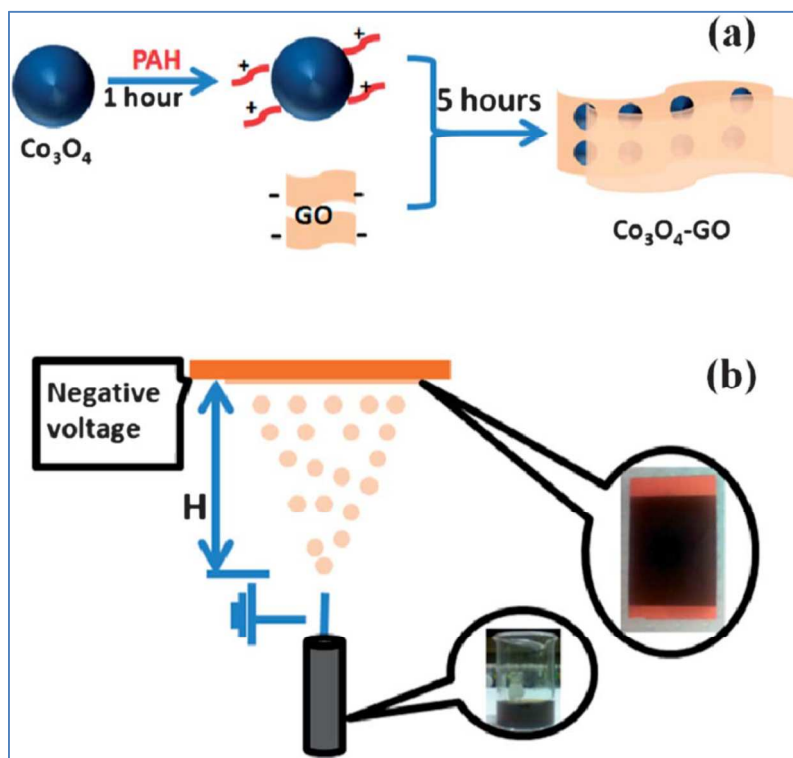


Fig. 14

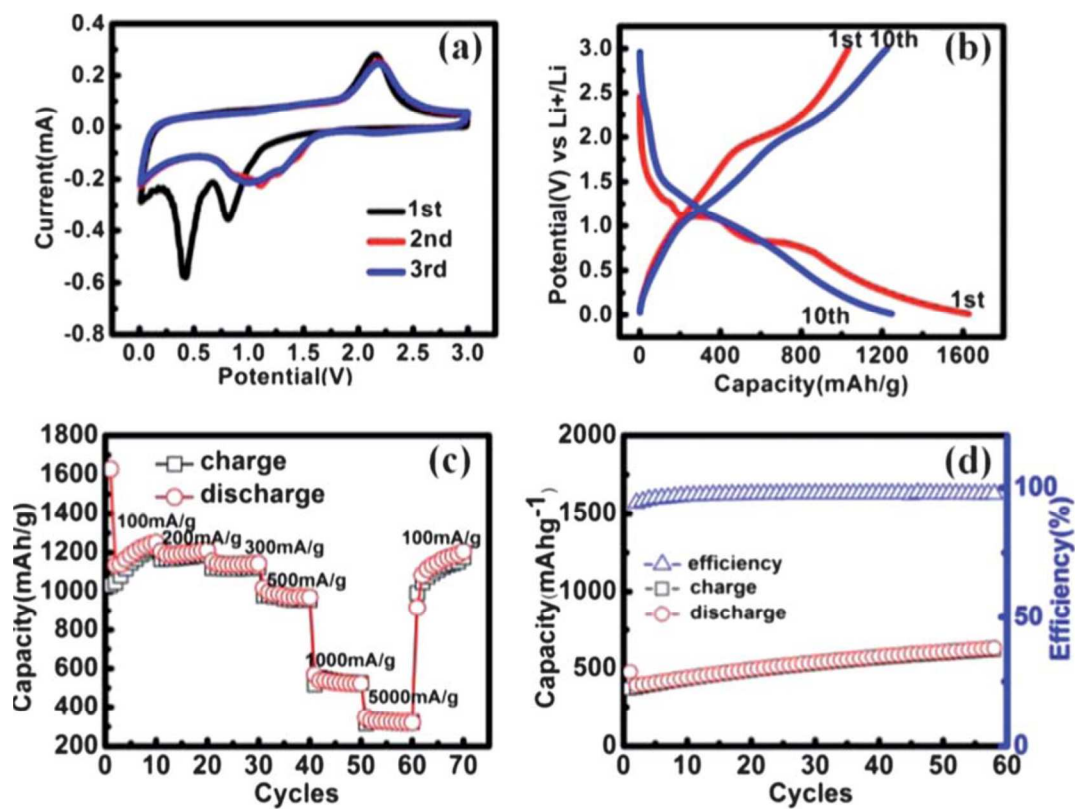


Fig. 15

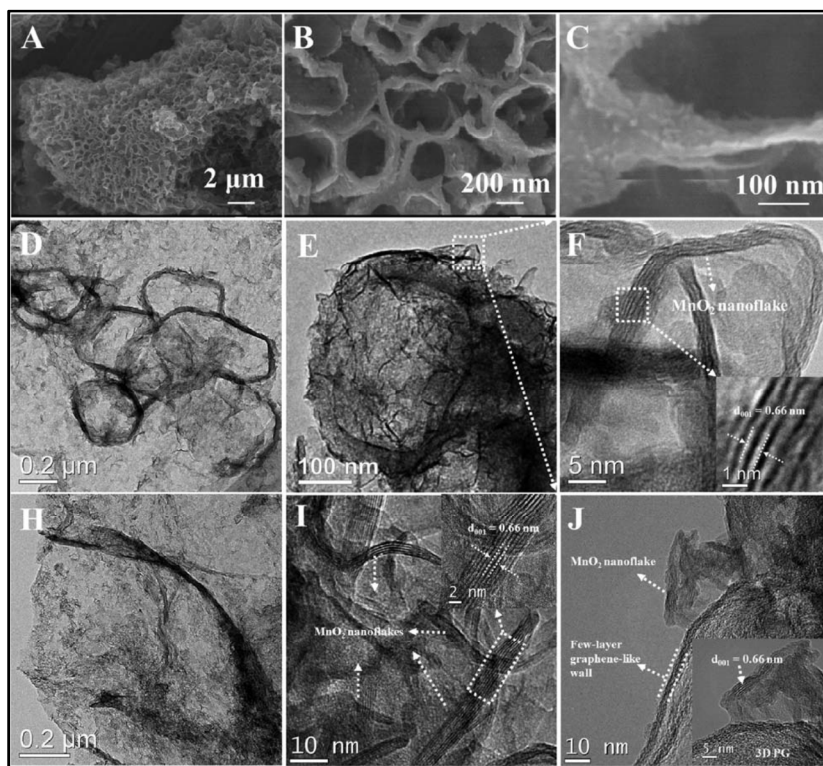


Fig. 16

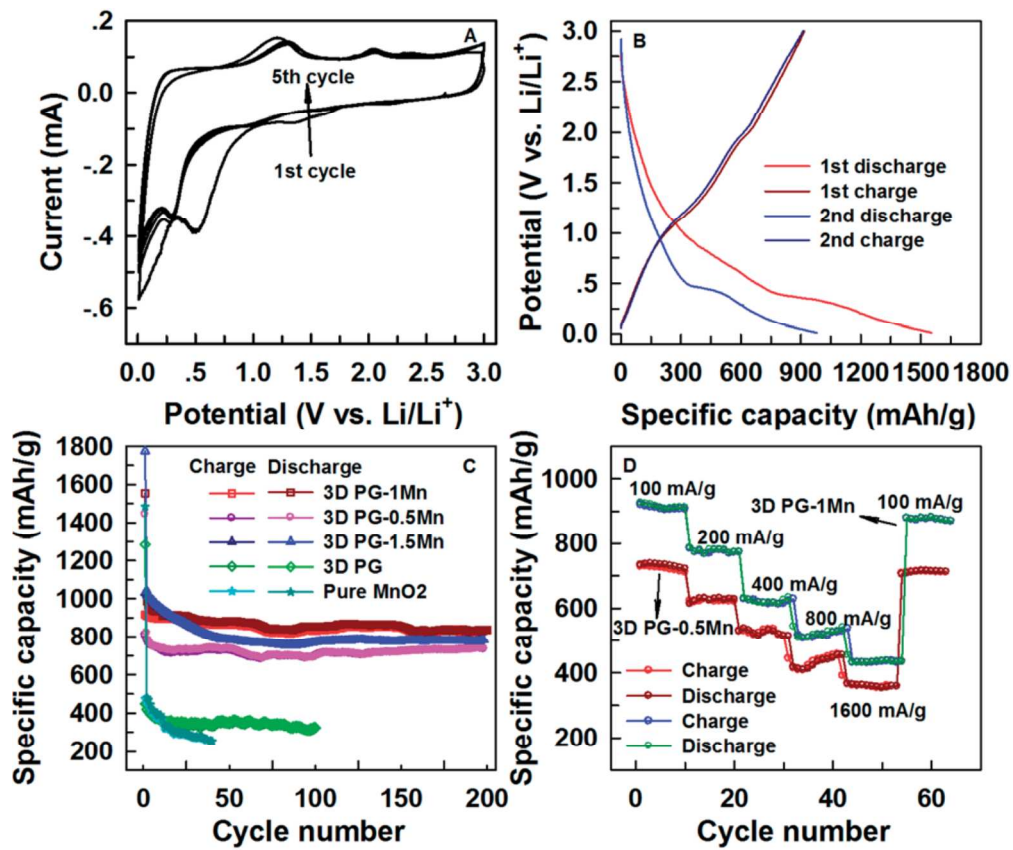


Fig. 17

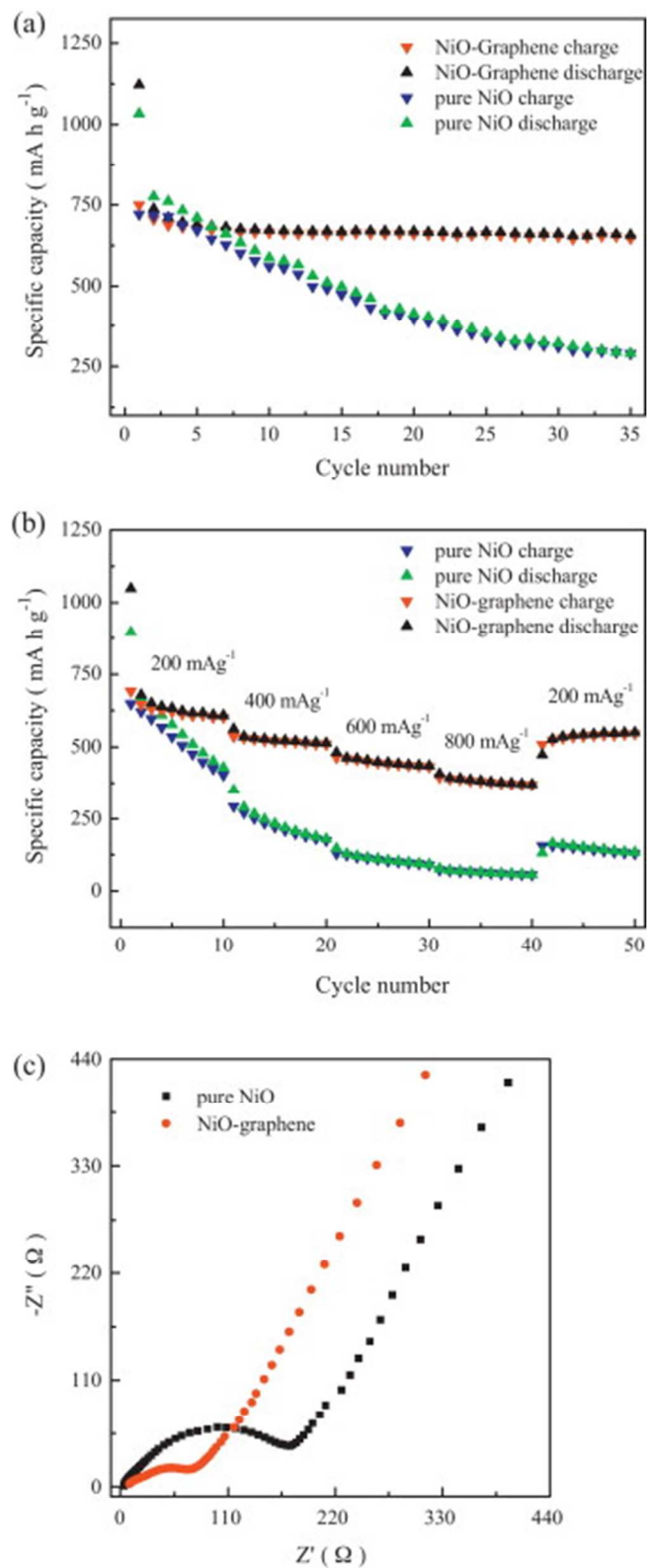


Fig. 18

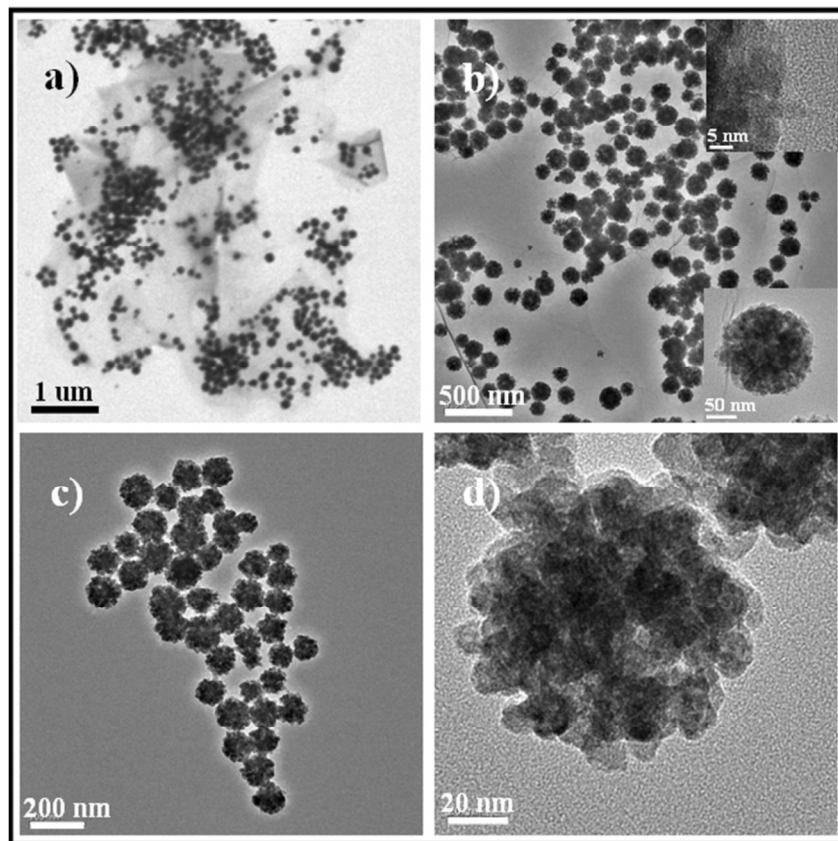


Fig. 19

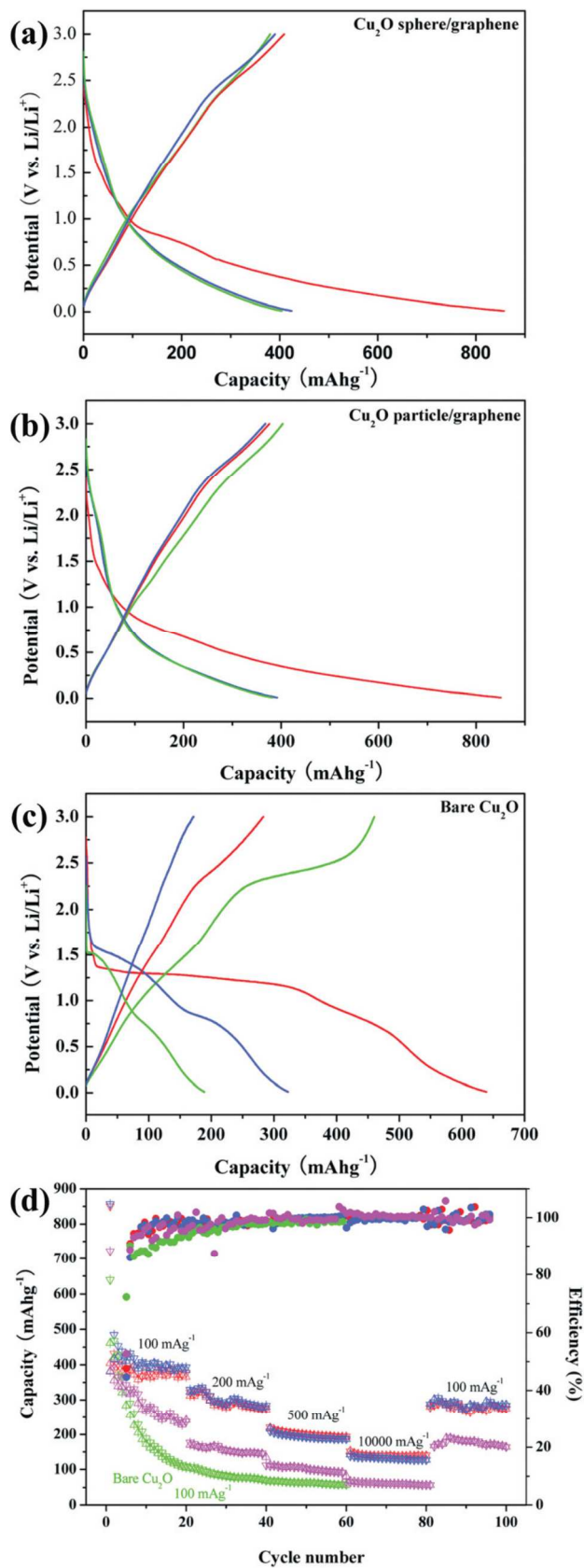


Fig. 20

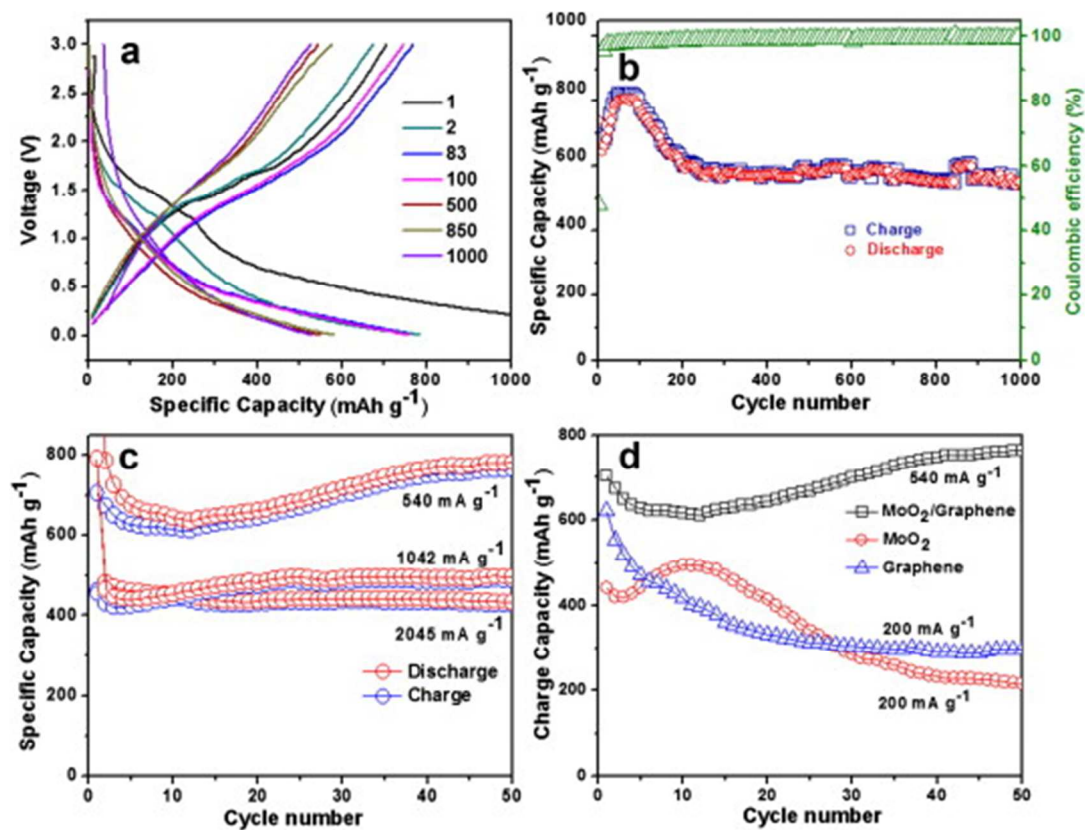


Fig. 21

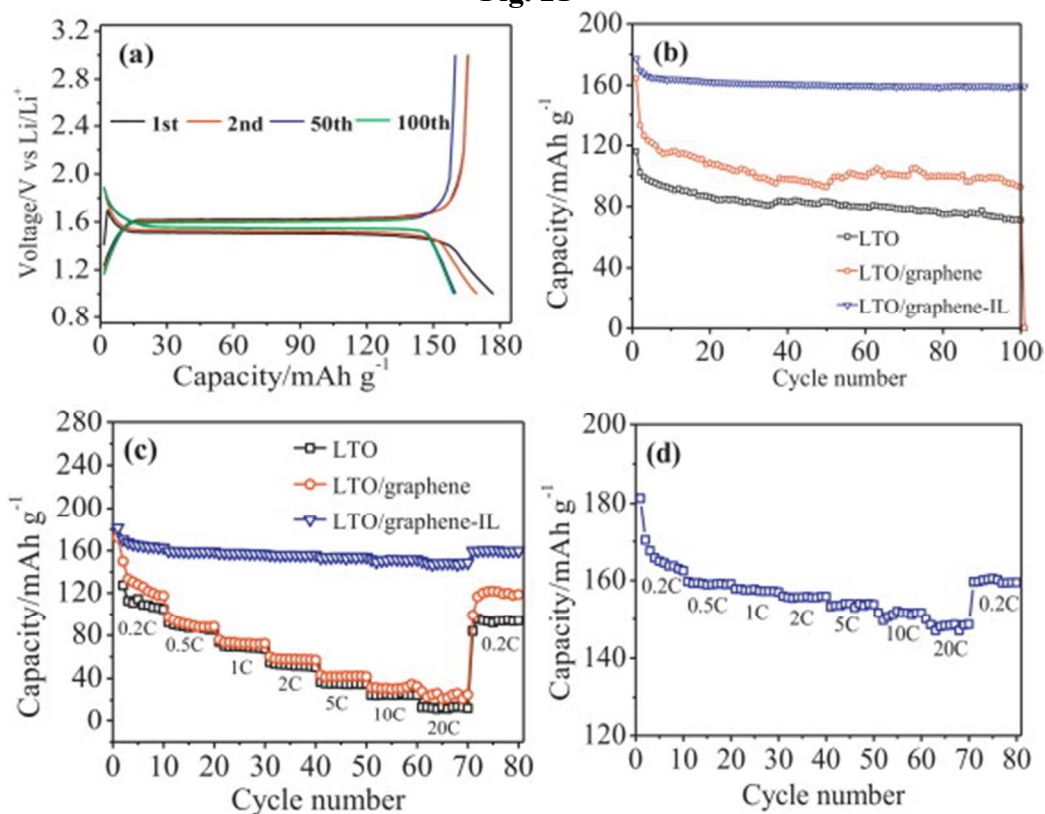


Fig. 22

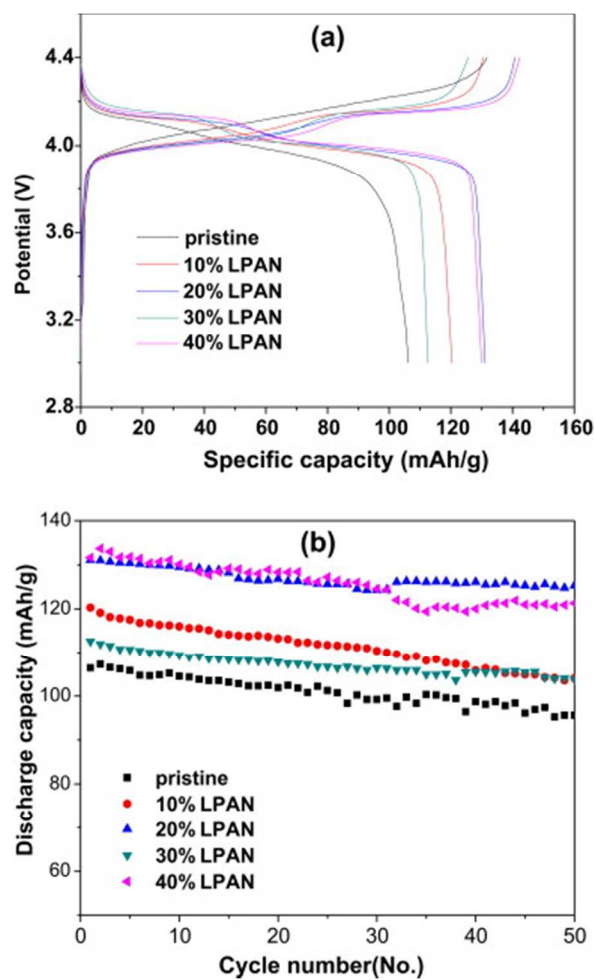


Fig. 23

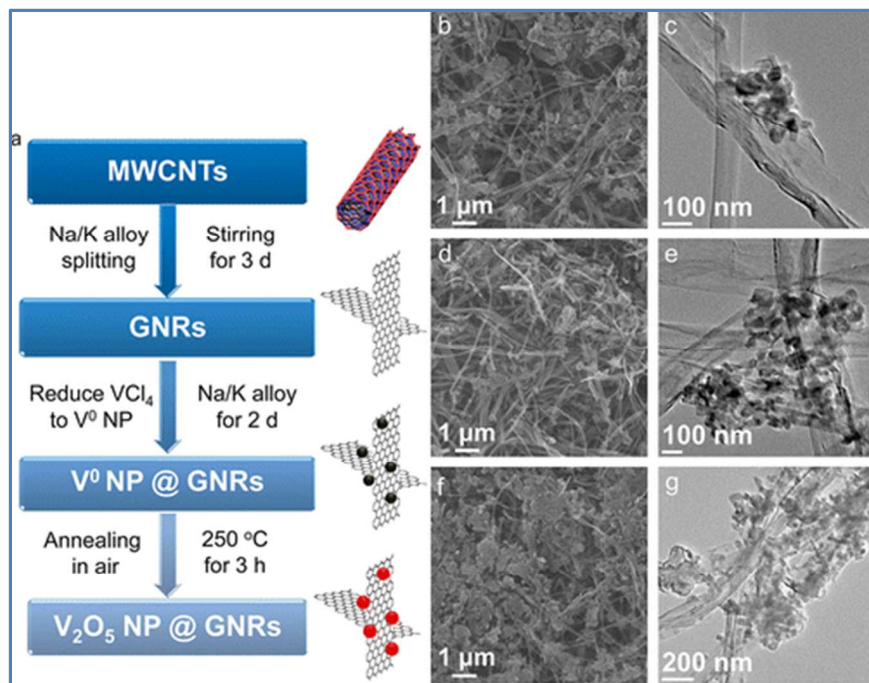


Fig. 24

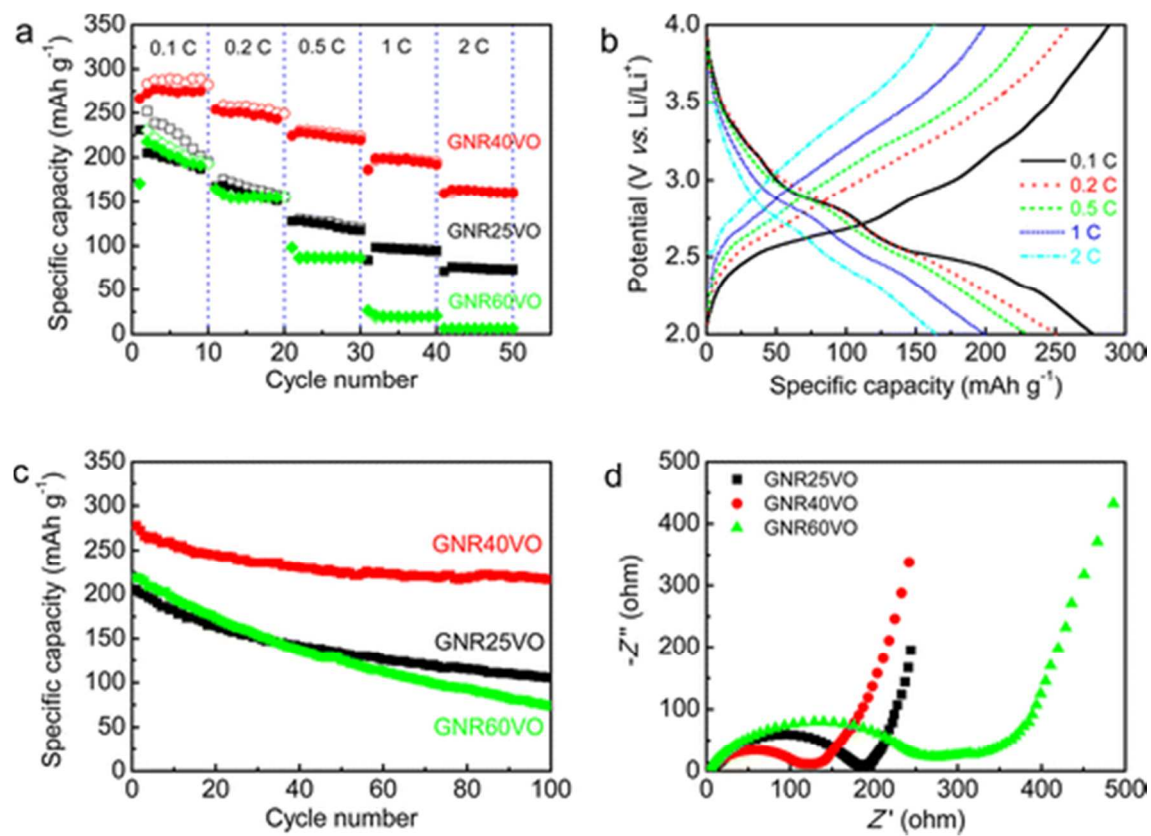


Fig. 25

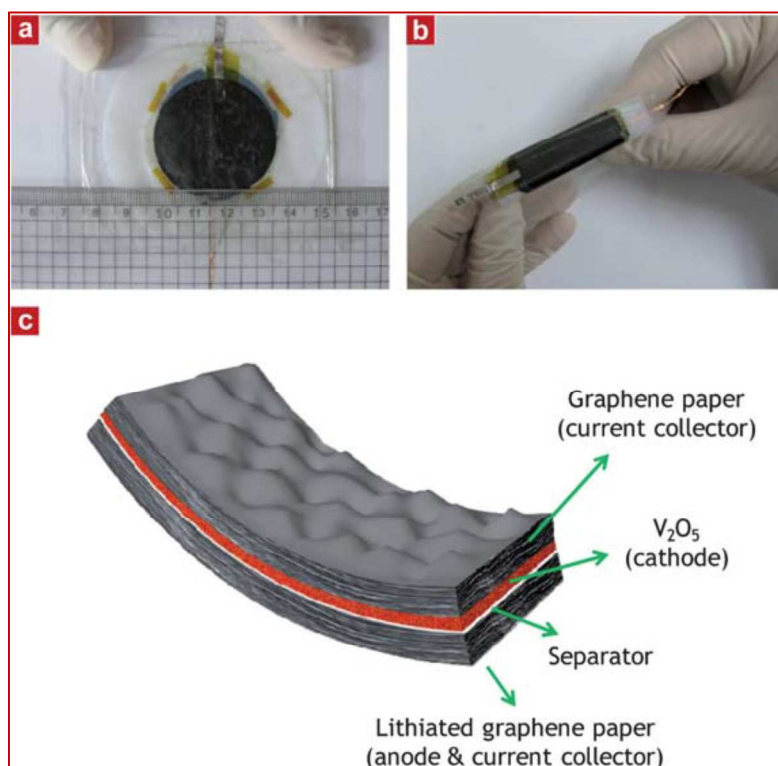


Fig. 26